Chapter 2

Anatomically "Calibrated" Isolated Respiratory Networks from Newborn Rodents

Araya Ruangkittisakul, Bogdan Panaitescu, Lucia Secchia, Nicoleta Bobocea, Chase Kantor, Junya Kuribayashi, Makito Iizuka, and Klaus Ballanyi

Abstract

En bloc and transversal slice preparations from perinatal rodents are established in vitro models for studying control of breathing by neurons and neighboring glial cells in the lower brainstem. These neural "respiratory networks in the dish" show features complementary with those in recent in vivo models that enable, for example, optogenetic manipulation for studying behavioral changes in awake animals or modulation of these circuits by higher brain regions during sleep. Contrary, the in vitro models allow respiratory network analysis at the (sub)cellular level. This is currently studied using powerful analytical tools such as quantitative pharmacology and patch-clamp recording of biophysical membrane properties of respiratory interneurons and/or motoneurons (plus neighboring glia). Increasingly, these approaches are combined with fluorescence imaging of both activity and morphology of individual cells or respiratory groups. Our recent work indicates that properties of the isolated respiratory networks depend critically on both their physical dimensions and the composition of superfusates used for their study. Based on this, we recommend to use anatomically "calibrated" rhythmic *en bloc* and slice preparations that we have developed and to study these models in superfusate that mimics in vivo conditions as closely as possible. We show here how these preparations are generated and present examples for pharmacological and "electrophysiological imaging" analyses that revealed novel properties of neuron–glial networks involved in respiratory control.

Key words: Breathing, Calcium, Fictive eupnea, Fictive sigh, Inspiratory, Multiphoton imaging, Pre-botzinger complex, Respiratory center

1. Introduction

Breathing movements are controlled by neurons that form "respiratory networks" with adjacent glial cells in the lower brainstem, the *medulla oblongata*. Since >200 years, findings from

Klaus Ballanyi (ed.), *Isolated Central Nervous System Circuits*, Neuromethods, vol. 73,
DOI 10.1007/978-1-62703-020-5_2, © Springer Science+Business Media New York 2012

in vivo experiments including brainstem transection indicate a rostrocaudal hierarchic organization of these neural respiratory networks that are located in three distinct areas. These bilaterally organized areas comprise the pontine, the dorsal and the ventral respiratory groups, with parts of the latter structure being referred to as the ventral respiratory column (VRC) (1–3). These three respiratory groups are located deep within the brain and are thus difficult to access. Consequently, there is a long-standing wish to isolate them for analyzing their properties. In 1984, Suzue (4) reported that an isolated newborn rat brainstem–spinal cord preparation (Fig. 1) generates inspiratory-related motor output. Since then, numerous studies aimed at elucidating respiratory network functions in this *en bloc* model (1, 2, 5, 6). In 1991, Smith and colleagues, involving our group (7), showed by serial brainstem section of this preparation that a limited VRC region, the pre-Bötzinger complex (preBötC), remains inspiratory active in a transversal brainstem slice, suggesting that it is responsible for generation of respiratory rhythm in mammals (Figs. 1 and 2). Since then, in vitro and in vivo studies established that the preBötC is crucial for normal breathing which greatly depends on active inspiration, whereas active expiration is less important (1–3, 8).

It is generally assumed that the preBötC comprises the only active respiratory network in the "classical" rhythmic slice which is a powerful model that enables application of various tools for analyses at both network and (sub)cellular levels. These tools include quantitative pharmacology, Ca^{2+} or voltage imaging, and patch-clamp analysis of membrane biophysics of preBötC neurons and preBötC-driven inspiratory active hypoglossal (XII) motoneurons (7, 9–15). Besides, "breathing" preBötC slices are studied increasingly from genetically engineered mice which either serve as models for respiratory diseases and/or contain respiratory neurons or glial cells that express fluorescent markers associated with cell-type-specific proteins such as transcription factors or neurotransmitter receptors (16–19).

The fact that various spinal and cranial ventral nerve roots in the brainstem–spinal cord preparation show inspiratory-related activity enables the analysis of different preBötC-driven inspiratory motor networks (5, 20–22). Such analyses can make use of most "electrophysiological imaging" approaches and genetic tools that are applicable to the slice model (5, 6, 15, 23, 24). Moreover, the *en bloc* model allows investigation of mutual interactions between inspiratory center neurons and another class of respiratory interneurons. This "parafacial respiratory group" (pFRG) was identified by voltage imaging in newborn rat *en bloc* medullas in the milestone study in 2003 by Onimaru and Homma (25). That report and previous work from that group reviewed in 1999 by Ballanyi and colleagues (5) hypothesized that a major rhythmogenic portion of the pFRG is located within the ventrolateral medulla several

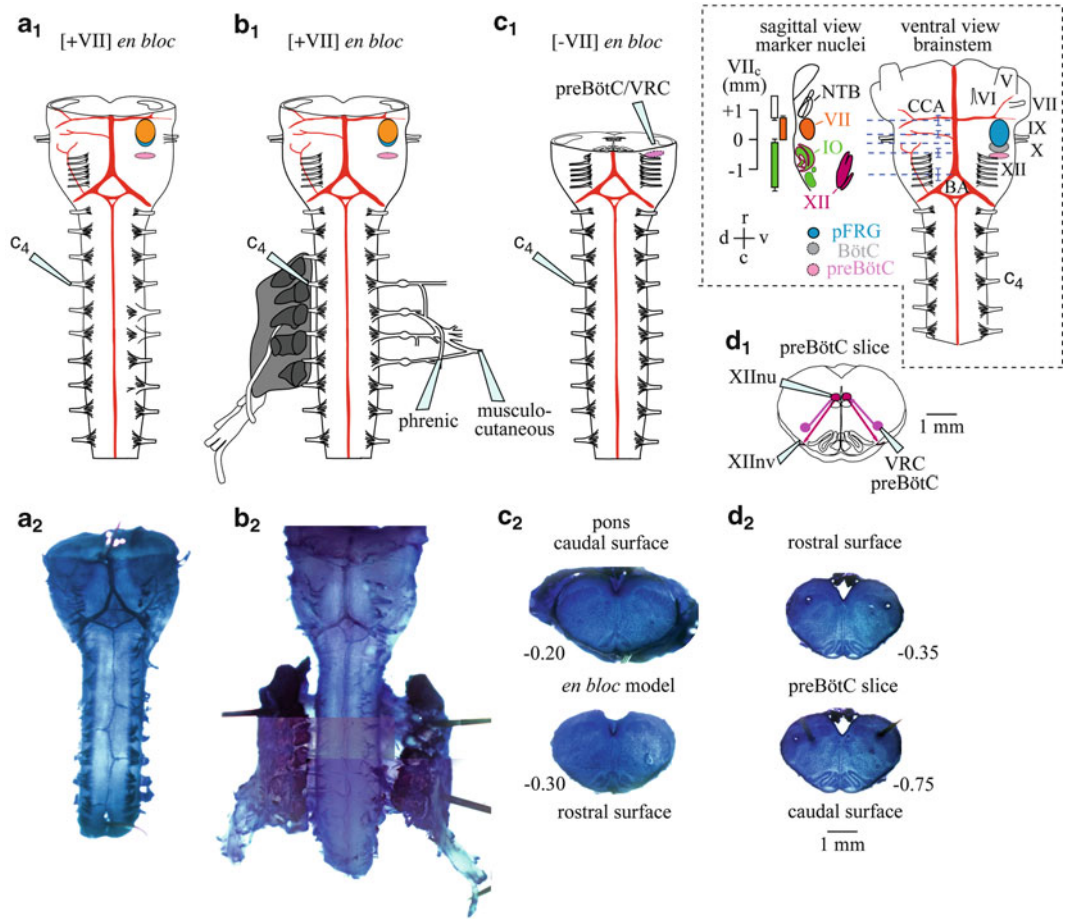


Fig. 1. Calibrated newborn rat “respiratory networks in the dish.” The inset in the *dotted box* indicates in the ventral brainstem view the estimated rostrocaudal extents of inspiratory active pre-Bötzinger complex (preBötC) and expiratory pre-/postinspiratory active parafacial respiratory group (pFRG) neural networks that form a dual respiratory center. The region between these respiratory groups corresponds to the Bötzinger complex (BötC) which is primarily expiratory active in adults but not yet studied in newborns. The sagittal view in the inset indicates mean values plus standard deviations of rostrocaudal extents of some respiratory brainstem marker nuclei included in a newborn rat brainstem atlas for generating anatomically defined (“calibrated”) inspiratory active transversal preBötC slices (see Fig. 2). These nuclei are the inspiratory active hypoglossal (XII) motor nucleus, the nucleus of trapezoid body (NTB), and particularly the “peri-inspiratory” active facial (VII) motor nucleus plus different subregions (“loops”) of the inferior olive (IO). The respiratory groups and marker nuclei have a defined position relative to respiratory active nerve roots on the ventral brainstem surface. Specifically, these roots are from XII, trigeminal (V), abducens (VI), glossopharyngeal (IX), and vagal (X) nerves. Importantly, the most rostral XII root corresponds to the location and rostrocaudal extent of the preBötC. (**a**–**c**) Brainstem–spinal cord preparations. (**a**$_1$) Schema of the “Suzue preparation” (4), which is rostrally transected at the caudal cerebellar artery (*CCA*, see inset), whereas the cord is typically cut at the last cervical (C_8) or first thoracic (T_1) level. This is the “classical” *en bloc* model with complete *VII* nucleus (“[+VII] *en bloc*”) for studying the dual respiratory center. (**b**$_1$) The *en bloc* model in **a**$_1$ can be isolated with intact cervical and brachial plexuses for recording from cervical (e.g., C_4) roots plus phrenic, brachial, and/or musculocutaneous nerves. The drawing on the *left* is based on an actual preparation, while the drawing on the *right* is derived from (67). (**c**$_1$) shows a “calibrated” *en bloc* preparations with the manually cut rostral surface located –0.25 mm caudal to the caudal end of VII nucleus, VII_c (see inset and numbers next to stained preparations). This [–VII] *en bloc* model does not produce pFRG motor output and allows recording from the VRC/preBötC at the rostral surface and spinal (cervical) nerves. (**d**$_1$) Schema of preBötC slice with suction electrode positions for recording inspiratory-related rhythms. (**a**$_2$–**d**$_2$) show preparations according to **a**$_1$–**d**$_1$ that were chemically fixed and thionin-stained after the experiment for better visualization of brainstem (surface) markers for histological analysis of their anatomical margins (For further details, see text or (33, 34, 40)).

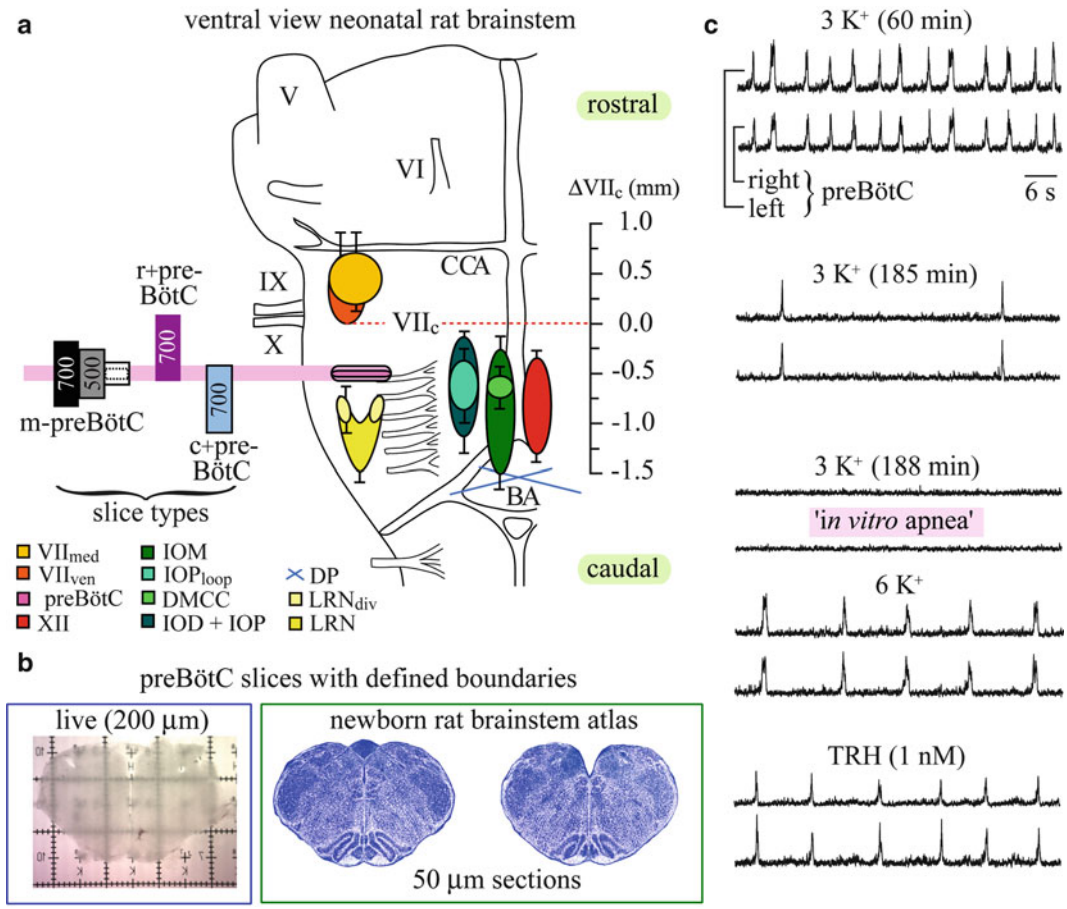


Fig. 2. Rhythm in physiological (3 mM) K^+ of calibrated preBötC inspiratory center slices. (**a**) Rostrocaudal extents of respiratory brainstem marker nuclei such as subnuclei of the IO and the VII motor nucleus, projected onto the ventral brainstem surface, referred to *VII$_c$* (see Fig. 1) are constant (see small standard deviations of bars) in Sprague-Dawley and Wistar rats of postnatal days (P) 0–4. This allows generation with novel "online histology" of various types of preBötC slices with defined anatomical boundaries referred to *VII$_c$*. "m-preBötC" slices have the preBötC in the *middle*. r+preBötC or c+preBötC slices contain the <100-µm small preBötC kernel necessary for generation of rhythm plus additional rostral or caudal tissue, respectively. (**b**) shows in the *left* a 200-µm-thin living rhythmic m-preBötC slice after an experiment next to two sections from a newborn rat reference atlas used to determine the margins of rhythmic slices. (**c**), Rhythm recorded with two suction electrodes in solution with 3 mM K^+ and 1 mM Ca^{2+} ("3K/1Ca") in a 500-µm-thick m-preBötC (m-preBötC[500/−0.70]W-P3) slice was stable for ~3 h before burst rate dropped from >10 to <4 bursts/min. After rhythm stopped spontaneously shortly after 185 min ("in vitro apnea"), it was restored by raising K^+ to 6 mM or bath application of thyrotropin-releasing hormone (TRH) (details in (33, 40)). Abbreviations: *DMCC*, dorsomedial cell column of inferior olive (IO); *IOM*, medial IO; *IOD*, dorsal IO; *IOP*, principal IO; *IOP$_{loop}$*, lateral loop of IOP; *LRN*, lateral reticular nucleus; *LRN$_{div}$*, LRN divided into medial and lateral subnuclei; *VII$_{med}$*, medial subnucleus of VII; *VII$_{ven}$*, ventral subnucleus of VII; *DP*, pyramidal decussation. Other abbreviations in Fig. 1 (Modified after (40), with kind permission).

100 µm rostral to the preBötC in an area surrounding the caudal end of facial (VII) motor nucleus, VII_c (Figs. 1 and 2). This area also contains the retrotrapezoid nucleus that is involved in central respiratory chemosensitivity and may (partly) overlap with the pFRG (26, 27).

Recent findings, by others and us, indicate that important pFRG components are also located close to the rostral end of VII nucleus (28, 29). pFRG neurons drive, for example, lumbar motoneurons innervating expiratory abdominal muscles or facial motoneurons driving upper airway muscles (6, 8, 21, 22). These observations, along with the finding that opioids depress preBötC activity but not rhythmic bursting of pre-/postinspiratory active pFRG neurons, suggest that the inspiratory preBötC and the functionally expiratory pFRG constitute a pivotal dual respiratory center, at least in newborn mammals (2, 5, 23, 24).

Identification of the structure–function relationship for the dual respiratory center in the *en bloc* model is difficult because inspiratory and pre-/postinspiratory neurons are distributed widely along the rostrocaudal VRC axis, indicating that the preBötC and pFRG may partly overlap (5, 24, 30). Even in the more reduced inspiratory slice model, the structure–function relationship of the preBötC is not well elaborated. Between laboratories, preBötC slice thickness ranges from 200 µm to >1,000 µm, and superfusates used for their study differ notably, particularly regarding the contents of Ca^{2+} (0.8–2.5 mM) and K^+ (3–11 mM) (4, 7, 10, 12, 18, 31–35). Because these cations greatly affect neuronal excitability, their extracellular concentrations in the mammalian brain are tightly regulated, specifically to 1.2 mM for Ca^{2+} and 3 mM for K^+, except for short activity-related transients (36–39). These differences in physical dimensions and/or ionic superfusate composition may explain some discrepant findings between groups, for example, regarding the relevance for rhythm of "intrinsic bursting" properties of respiratory neurons (2, 3, 7, 12–14, 25).

Here, we summarize factors that are important for identifying structure–function relationships for inspiratory versus expiratory networks in perinatal rodent *en bloc* and slice preparations. To achieve this, it was firstly necessary to determine anatomical brainstem marker regions in these models for generating "calibrated" respiratory networks in the dish with identified and reproducible rostrocaudal margins. It is one major aim of this chapter to summarize this "online histology" approach for obtaining calibrated *en bloc* and slice preparations from newborn Wistar and Sprague-Dawley rats and preBötC slices from C57BL/6 mice (33, 34, 40, 41). Based on this work and other recent studies from our group (18, 28, 35, 42–44), we also exemplify how physical dimensions and superfusate composition influence rhythmic activities generated by the preBötC and the dual respiratory center in the slice and *en bloc* models, respectively. Also, regarding previous findings on the "noncalibrated" in vitro models, we focus on our own publications reflecting our technical experiences with these preparations. Reference to work by others, for example, regarding interstitial brain levels of ions or glucose, is mostly represented by review articles from other leading groups using these respiratory models and from our own recent reviews.

2. Materials

Various materials used by our group for studying respiratory neurons in vitro are identical with those for analyzing dorsal vagal neurons in brainstem slices. Accordingly, complementary information is given in our chapter on these cells (Chap. 1-Trapp and Ballanyi (45)).

2.1. Animal Models

Respiratory functions are mostly studied in *en bloc* or slice models from perinatal rodents, traditionally mainly Wistar or Sprague-Dawley rats. Increasingly, mice from outbred (e.g., CD1, NMR, OF1) or inbred strains (e.g., C57BL/6) are being used due to ongoing development of transgenic models (16–19). Importantly, use of the *en bloc* and slice models from rats is restricted to newborn animals until about postnatal day (P) 7 (5). Rhythmic slices from some mouse strains such as CD1 or OF1, but likely not *en bloc* preparations, can be used from up to ~P14 animals unless a precocial strain is used (13, 14, 18, 32, 46, 47). This restriction is probably mostly due to inadequate supply of these nonperfused in vitro models with oxygen (O_2) as dealt with below (Sect. 5). In both species, functioning *en bloc* preparations and preBötC slices can be obtained from fetal animals, in which respiratory-related brainstem activities start ~1 week before birth (19, 46, 47). Only one *en bloc* preparation and normally also only one inspiratory active slice are obtained per animal, but see Sect. 4.2.1.

2.2. Solutions

In the following, we refer to compositions of (1) superfusates for optimal functions of the in vitro respiratory networks, (*2*) solutions for patch clamp and (ion-sensitive) microelectrodes, and (3) solutions for histology.

2.2.1. Superfusates

Commonly, the term "artificial cerebrospinal fluid" ('ACSF') is used for superfusate/perfusate in which isolated vertebrate nervous tissues are studied. However, firstly, the composition of cerebrospinal fluid differs substantially from that in the extracellular (interstitial) space of the brain because the latter fluid contains tonically present and/or phasically released neurotransmitters and other neuroactive agents such as endorphins or growth factors (36, 39, 48). Secondly, interstitial concentrations of these agents differ between brain regions and depend on patterns of spontaneous activity and/or developmental state in a given brain area (36, 39, 48). Accordingly, we use the term "superfusate" or "standard/control solution" instead of "ACSF".

Our recent findings pointed out that the ionic composition of the superfusate is pivotal for intrinsic activity of isolated perinatal rodent respiratory networks and their responses to various neuromodulators (Sect. 4.2.2). Based on this, we recommend for use with >600-µm-thick preBötC slices or *en bloc* preparations the

so-called 3K/1Ca superfusate of the following ionic composition (in mM): 120 NaCl, 3 KCl, 1 $CaCl_2$, 2 $MgSO_4$, 1.25 NaH_2PO_4, and 26 $NaHCO_3$. The pH of this solution is adjusted to 7.4 by continuous gassing with "carbogen", which is a mixture of 95% O_2 and 5% carbon dioxide (CO_2). Such "carbogenation" is, for example, achieved with a gas dispersion tube that is also termed "microfilter candle" (Fisher Scientific, Canada; www.fisher.ca or ROBU, Hattert, Germany; www.robuglas.com).

Regarding the content of glucose (more precisely "D-glucose" or "dextrose") of standard superfusate, 20–30 mM is necessary for the *en bloc* model. For calibrated preBötC slices, 20 mM glucose is commonly used in superfusate, although they remain viable and rhythmic at levels as low as 1 mM (for details, see Sect. 4.2.2).

We found that inspiratory-related rhythm in 400-µm-thin preBötC slices in 3K/1Ca solution stops spontaneously within <2 h (in vitro apnea) but can be reactivated for time periods >7 h by raising K^+ to 7 mM (41, 42). In 7K/1Ca, the rate and amplitude of inspiratory rhythms in preBötC slices are appropriate for long-term studies and basically similar to rhythms in preBötC slices studied by others in 8–9 mM K^+ (and 1.5 mM Ca^{2+}) (2, 13, 14). Based on our recent unpublished findings, it may be appropriate for studies on "K^+-sensitive" cellular processes in thin preBötC slices (Sect. 4.2.2) to use 5K/1Ca solution at the start of recording and raise K^+ to 6 mM, and then eventually to 7 mM, when rhythm starts to slow down.

2.2.2. Electrode Solutions

The following "standard" patch electrode solutions are currently used for whole-cell patch-clamp recording (Sect. 3.2.2) in the Ballanyi laboratory: (1) standard ("low Cl^-") pipette solution contains (in mM) 120 K-gluconate, 1 NaCl, 1 $CaCl_2$, 1 $MgCl_2$, 11 K_4-BAPTA, 0.5 Na_2-ATP, and 10 HEPES (pH adjusted to 7.4 with KOH); (2) "high Cl^-" solution has the same composition, except that 120 mM KCl replaces 120 mM K-gluconate; and (3) "perforated patch" solution contains 5–10 µg/ml gramicidin prepared from two stock solutions. Stock I contains 2 mg gramicidin in 1 ml dimethyl sulfoxide and is freshly made every 4 h, whereas stock II contains 140 mM KCl and 10 mM HEPES; pH is adjusted to 7.4 with KOH. Stocks I and II are mixed at a ratio of 1:10, and this mixture is diluted 1:40 or 1:20 with one of the above patch solutions. Pipettes are prefilled with 2 µl of these solutions to avoid contamination of the tissue with gramicidin during cell searching. Rationales for particular compositions of patch electrode solutions are outlined in review articles (49, 50) and below (Sect. 3.2.2). Recording with intracellular sharp microelectrode is feasible for respiratory motoneurons but has not yet been reported for VRC interneurons in the respiratory networks in the dish. These electrodes with tip diameters <0.2 µm, resulting in a DC resistance of 30–200 MΩ, are typically filled with 3 M KCl, 1 mM K^+-acetate,

or 1 M Mg^{2+}-acetate. Standard superfusate is convenient for filling suction electrodes for recording of extracellular population activity or electrical stimulation and also for filling reference barrels of extracellular double- or triple-barreled ion-sensitive microelectrodes (Sect. 3.2). Ion-sensitive barrels of the latter type of microelectrodes contain the following combination of ion-selective resin (in the silanized tip) and "backfilling" solution: (1) K^+ electrodes (Fluka 82500, from World Precision Instruments [WPI Sarasota, FL, USA; www.wpiinc.com]; 150 mM KCl), (2) Ca^{2+} electrodes (Fluka 21048, WPI; 150 mM KCl), and (3) pH electrodes (Fluka 95291, WPI; 40 mM K_2HPO_4 + 23 mM NaOH + 15 mM NaCl, buffered to pH 7 with 1N HCl).

2.2.3. Histological Solutions

For histological analysis using the dye thionin (Sigma-Aldrich; www.sigmaaldrich.com) (Sects. 2.9 and 3.1), brainstem tissue is fixed in 4% paraformaldehyde in phosphate buffer (1:2 mixture of 0.1 M NaH_2PO_4 + 0.1 M Na_2HPO_4 in H_2O, pH 7.2). The staining solution consists of 0.1 M Na^+-acetate trihydrate + 0.1 M acetic acid + 1% Thionin acetate dissolved in distilled water. The solution for embedding brainstems for facilitated sectioning consists of 6% agar-agar (Sigma-Aldrich) dissolved in boiling distilled water that is subsequently cooled down to ~40°C. A fixed brainstem is quickly dried (with filter paper or paper towel) and then placed in a small container (e.g., 10-ml beaker or small Petri dish) that is prefilled with agar solution. More agar solution is then added to cover the entire tissue block. The embedded block is subsequently cooled on an ice pad to eliminate air bubbles.

Whole-cell patch-clamp recorded respiratory neurons are stained with either 0.5% lucifer yellow (Sigma-Aldrich) or 0.2–0.5% biotin or biocytin (Sigma-Aldrich) added to the patch electrode solution. For histological reconstruction of these cells, we fix preparations either according to our studies in collaboration with the group of Dr. H. Onimaru (Showa University, Tokyo, Japan) (24, 51, 52) for >48 h at 4°C in "Lillie" solution (i.e., 10% formalin in phosphate buffer, pH 7.0). According to our previous collaboration with the group of Dr. S.W. Schwarzacher (University of Frankfurt, Germany) (53), tissue was fixed for 4–15 h at 4°C in 4% paraformaldehyde (in phosphate buffer, pH 7.4), followed by 10-h immersion in 30% sucrose solution. Further histological processing for neuron reconstruction is described below (Sect. 2.9).

2.3. Devices for Brainstem–Spinal Cord Dissection and Brainstem Slicing

Under anesthesia using isoflurane (Baxter Corp., Deerfield, IL, USA; www.baxter.com) (Sect. 3.1), the brainstem–spinal cord preparation is dissected with fine forceps (e.g., Dumont #5, straight tip [0.05 × 0.02 mm] or Dumont #5SF [0.025 × 0.005 mm]) and (iris) scissors (e.g., Vannas-style, straight tip angle [length 80 mm, 2.5-mm blade] or Vannas Tübingen [length 85 mm, 5-mm blade]) (supplied, e.g., by Fine Science Tools Inc., Vancouver, BC, Canada;

www.finescience.com). Also for generating rhythmic slices, the brainstem is firstly isolated and then transferred to the vise of a vibratome such as the VT1000S (Leica Biosystems, Nussloch, Germany; www.leica-microsystems.com) or the 5,000mz (Campden Instruments Ltd., Loughborough, UK; www.campdeninstruments.com). Use of a high-quality vibratome is recommended particularly when <250-μm-thin slices are planned to be used and/or recording from superficial visualized cells is intended (18, 35, 43, 48). The less expensive "McIlwain" tissue chopper (Warner Instruments, Hamden, CT, USA; www.warneronline.com) may cause more damage to superficial slice layers but can be used if recording is restricted to extracellular or "blind" patch-clamp techniques in thicker slices (Sect. 3.2).

There is no obvious need for slicing in ice-cold solution of particular composition, such as substitution of Na^+ with choline, or for storing preparations (in such solution) in a heated chamber for recovery from sectioning injury (48) (Chaps. 1-Trapp and Ballanyi (45), 3-Moore et al. (54), 8-Sanchez-Vives (55), 9-Broicher and Speckmann (56), 11-Kantor et al. (57) and 14-Biggs et al. (58)). In fact, respiratory rhythms can be recorded in both *en bloc* preparations and slices within <10 min after their generation, and these models remain active for extended time periods (Sects. 3.1.4 and 4.2).

2.4. Recording Chamber and Superfusion System

For experiments involving visualization of cells using an upright microscope (18, 35, 43, 48) (Sect. 2.8), we use a submerged-type acrylic chamber system with glass bottom, for example, from Warner Instruments (Fig. 3). A custom-made "submerged"-type acrylic recording chamber (Fig. 3) (see also Chap. 1-Trapp and Ballanyi (45)) is used by us for "blind" electrophysiological recording experiments, in which the preparation is mechanically fixed and electrodes are positioned under visual control using a stereomicroscope (Sect. 2.8) (Fig. 3). The latter type of chamber requires a cold-light source with flexible glass fiber guides, for example, from WPI or Zeiss (Oberkochen, Germany; www.zeiss.com). The recording chambers are continuously perfused with carbogenated standard solution (Sect. 2.2) that is prewarmed in a water bath (DC 10, Thermo Haake, Sigma-Aldrich) and administered via a peristaltic roller pump such as the Watson-Marlow Alitea (Sin-Can, Calgary, AB, Canada; www.sincaninc.com). The superfusate passes through a custom-made acrylic bubble trap to protect from perturbation of fluid flow in the recording chamber. The chamber is typically kept at 25–27°C via a temperature control system such as the TC-324B (Harvard Apparatus, Saint-Laurent, QC, Canada; www.sincaninc.com) (Fig. 3). Superfusate is removed from the recording chamber via a hypodermic needle (gauge 18 G1½″) connected to either (a further channel of) a roller pump or a vacuum system, for example, an aquarium pump (Fig. 3). Tubings for the superfusion system should be impermeable to gases, in particular O_2 and

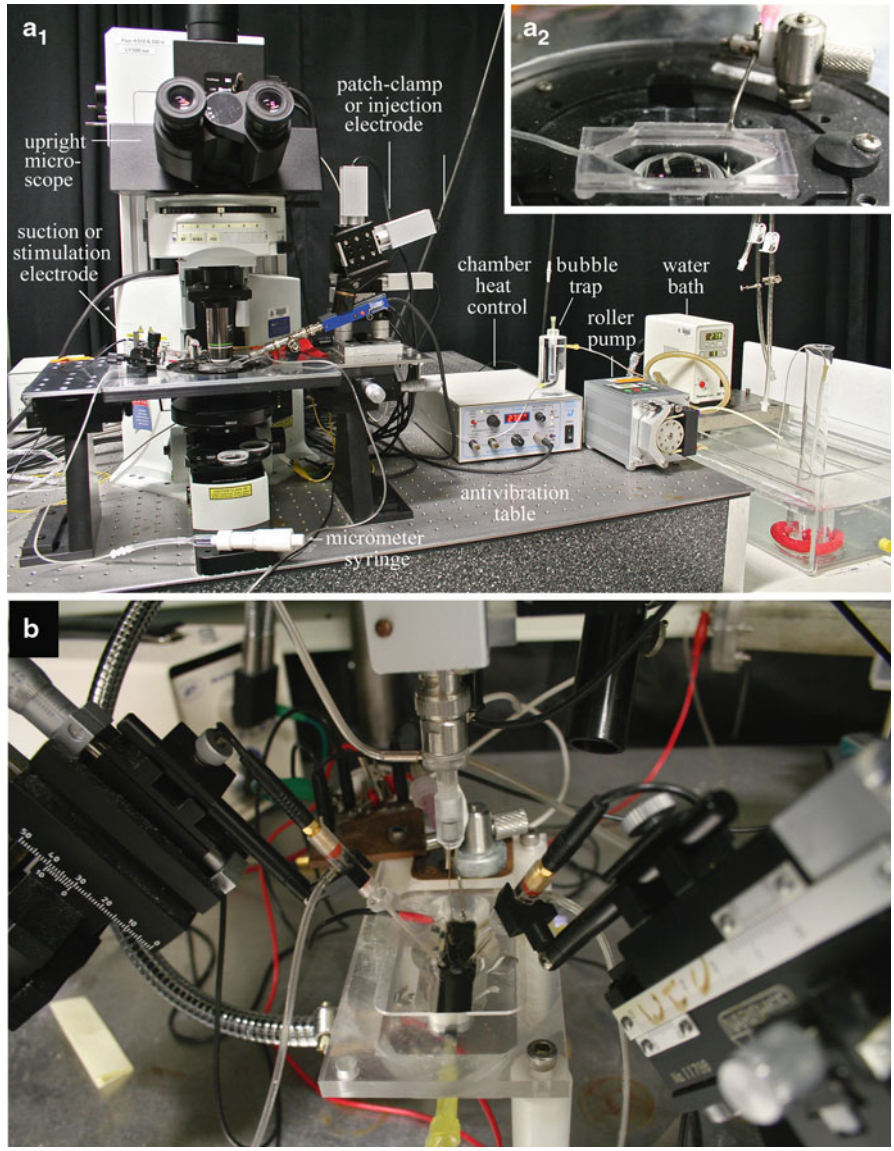


Fig. 3. Equipment for "electrophysiological imaging" in respiratory networks in the dish. (**a**) An upright microscope (**a**$_1$) and a "fixed" custom-made XY microscope stage are used for positioning and mechanical fixation of one calibrated preBötC slice or *en bloc* preparation with a "harp" to the glass bottom of a "Warner" submerged-type recording chamber (**a**$_2$), or with steel insect pins, if a layer of silicone ("Sylgard-184®") has been added to cover the bottom of the chamber. Superfusate enters the chamber via a Tygon® or steel tube and is removed at the opposite end via a hypodermic cannula connected to a vacuum system (e.g., an aquarium pump). Superfusate is prewarmed in a "Haake" water bath while the temperature of superfusate in the recording chamber is kept constant by a "Warner" temperature control system. Superfusate is transported via a "Watson-Marlow" peristaltic ("roller") pump and passes an acrylic "bubble trap" before entering the recording chamber. Cells in slices are visualized using a x20 objective which is part of a FV300 Olympus confocal laser scanning imaging system. Fluorescent dye is injected via a broken patch electrode positioned with a "Siskiyou" step motor also used for patch recording using a HEKA "patch clamp" (HEKA headstage shown here) or npi "single-electrode voltage-clamp" amplifier. Neuronal population activity is extracellularly recorded using suction electrodes positioned via a Narishige micromanipulator and connected to a "WPI" or "AM-Systems" differential amplifier. The entire recording system is positioned on a "Kinetic Systems" antivibration table. (**b**) Recording chamber and mechanical arrangement

CO_2 with which the standard superfusate is carbogenated (Sect. 2.2). This ensures that the partial pressure of O_2 (PO_2) and CO_2/HCO_3^--adjusted pH, respectively, do not change during superfusate transport to the recording chamber. Stainless steel or Tygon® tubing (e.g., Fisher Scientific, Canada; www.fishersci.ca) is a convenient option in that regard.

For long-term viability and (spontaneous) activity of respiratory networks in the dish, flow rates for superfusate administration should be at least 5 ml/min for recording chambers with a volume of ~1 ml. Larger chambers may be necessary if multiple electrodes are to be positioned, for example, for recording of bath and tissue PO_2 as well as ion activities combined with suction electrode and intracellular recording. These larger chambers require a higher flow rate for a similarly effective exchange rate of superfusate compared to smaller models. Importantly, flow rates <5 ml/min in a ~1-ml chamber may cause interstitial accumulation of (inhibitory) neuromodulators such as adenosine (48). A small recording chamber may be necessary, in combination with recirculation of superfusate, for particular experiments such as those involving expensive drugs. In our hands, normal rhythmic activity in both *en bloc* and slice preparations persists for several hours during such recirculation. A sophisticated recording chamber in that regard is referred to in a different chapter (Chap. 1-Trapp and Ballanyi (45)). Though not studied systematically by us, it seems that rhythm, in particular, in calibrated preBötC slices is faster and more robust when the meniscus of the fluid is <1 mm above the slice surface. However, the lower the fluid level, the more sensitive it is to perturbations of superfusate flow. This may result in movement of the slice toward the meniscus because of surface tension and would thus impair supply of superficial slice areas with carbogenated superfusate and disturb recording as well.

For imaging experiments or patch-clamp recording from superficial visualized cells (18, 35, 43, 48), a single brainstem slice or *en bloc* preparation is transferred to the recording chamber (Fig. 3). The rhythmic slice is held in place by a nylon net fixed to a platinum frame (48) (Fig. 4 in Chap. 1-Trapp and Ballanyi (45)).

Fig. 3. (continued) for combining suction electrode (and eventually ion- and/or gas-sensitive microelectrode recording) with "blind" patch-clamp recording from the respiratory networks in the dish. Preparations are positioned and fixed in the silicone-covered submerged-type custom-made recording chamber using a stereomicroscope that can be combined with (or replaced by) a video camera. Superfusate system including inlet and outlet is identical with that in **a**. Intracellular recording is done using a "Siskiyou" (see **a**) or "Sutter" step motor while "Märzhäuser" (*left*) or "Narishige" (*right*) micromanipulators are stable enough for >10-h recording, for example, of neuronal population activity. Suction and patch electrodes are conveniently placed in "ALA Scientific" or "Warner" holders. The latter models, shown here on the *left* and *right* sides, are not bulky, thus enabling positioning of up to eight electrodes in this type of chamber, in particular when using the slim Narishige manipulators. While extracellular electrodes are positioned at an angle, the patch electrode (connected here to the headstage of an npi amplifier) advances perpendicularly through the tissue using digital readouts for the Siskiyou or Sutter motors for identifying the recording depth.

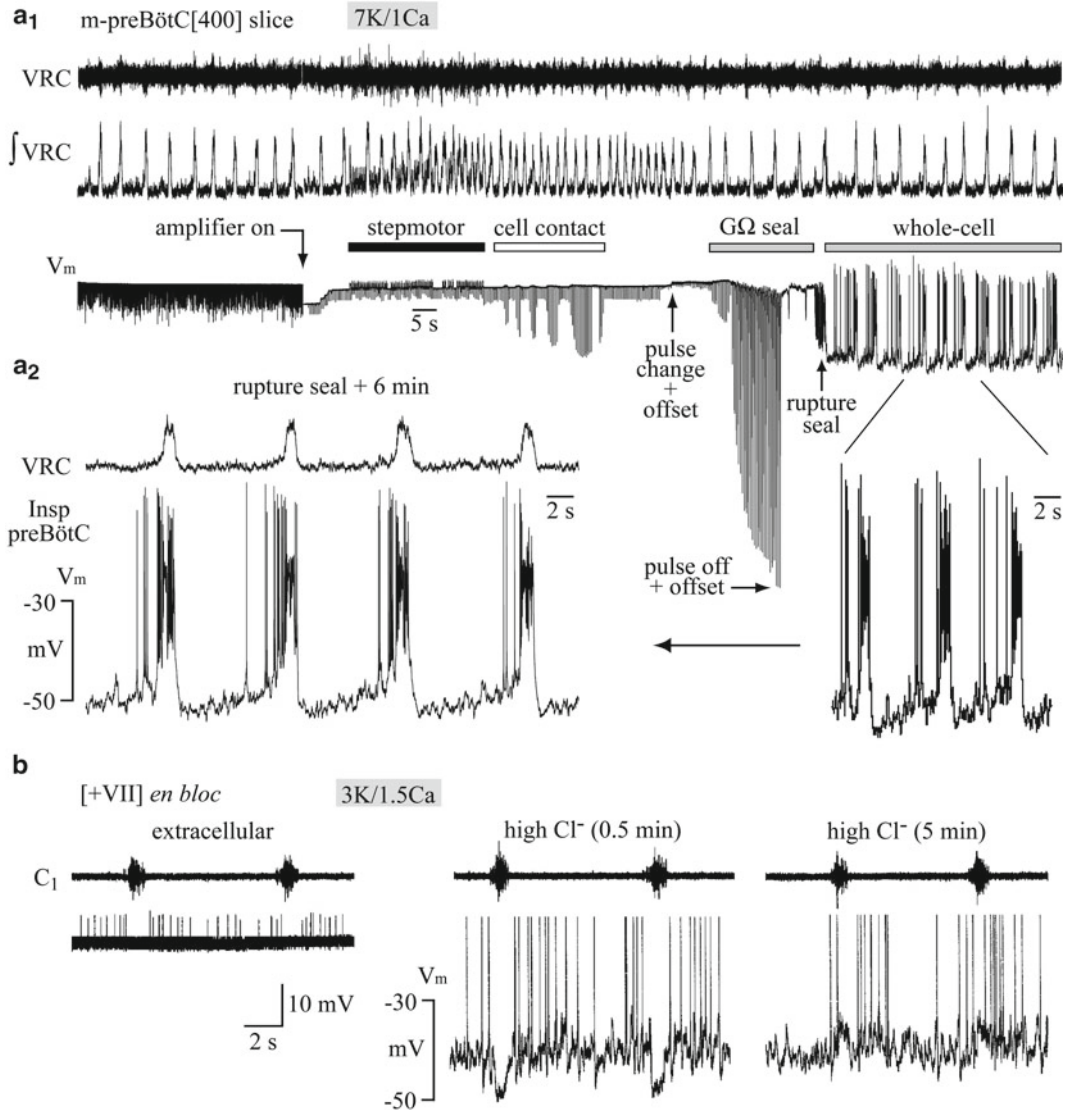


Fig. 4. "Blind" whole-cell recording from respiratory neurons. (**a**) Procedures involved in establishing a membrane potential (V_m) recording in "whole-cell" patch-clamp configuration. (**a**$_1$) In a m-preBötC[400/-0.75]W-P3 slice, inspiratory-related bursting is recorded with a suction electrode from the ventrolateral slice aspect containing the ventral respiratory column (*VRC*) with the preBötC extending rostrocaudally between 100 and 300 μm below the surface (see Figs. 1 and 2). Compared to the *upper VRC trace* showing the amplified (×10k) differentially recorded and band-pass filtered (0.3–3 kHz) raw signal, the integrated (τ: 50 ms) signal reveals the inspiratory bursts much better. After turning the intracellular npi amplifier on (see *arrow*), the patch electrode is positioned in the contralateral *VRC* and forwarded through the tissue using a Siskiyou step motor (see Fig. 3). Close to the cell membrane, the amplitude of the electrode voltage change in response to a repetitively applied rectangular DC current (-100 pA, 20 ms) increases and shows some flickering ("oscillations"). At this stage, the electrode is moved up and down by 1–5 μm until the oscillations during the test pulse are maximal and stable. Then, the amplitude of the test pulse is reduced to 10%, and the positive pressure (20–30 mmHg) applied to the electrode is removed. In most cases, a gigaohm seal establishes spontaneously, while in the other cases slight suction is applied to facilitate this. Once a seal of at least 1 GΩ is established, the pulse is switched off and the patch is ruptured by sudden suction, eventually combined with application of a short current pulse. In this example, the whole-cell configuration is established for an inspiratory ("Insp") preBötC neuron. The trace in **a**$_2$ from the same neuron shows that the recording

Platinum is mostly used because the frame needs to be both heavy and inert, but tantalum is a cheaper alternative, and both are available at Goodfellow (Huntington, United Kingdom; www.goodfellow.com). In recording chambers covered with silicone (Sylgard-184® ["Kwik-Gard"], WPI) (Fig. 3), a rhythmic slice can also be fixed with insect pins ("minutien pins," stainless steel, length 10 mm, 0.02-mm tip/0.2-mm base diameters; Fine Science Tools) inserted in its (dorso)lateral aspects, while suction electrode(s) provides further mechanical stability. Depending on the (angle of the) cold-light source used for illuminating the recording chamber, carbon powder may be added to the Sylgard-184® for better visualization of details of the preparation and electrode positioning. Also, *en bloc* preparations are fixed in Sylgard-184®-covered chambers with the ventral side up by placing a minutien pin at the rostral end of the brainstem and caudal end of the spinal cord. Further stabilization is achieved by suction electrodes used for recording nerve activities (Sect. 2.5).

2.5. Microelectrodes for Recording and Stimulation

Patch electrodes with outer tip diameters of 1.5–3 µm are used for "whole-cell" recording (7, 9, 42, 51–53, 59, 60) of membrane potential (V_m) or membrane currents of respiratory neurons for up to several hours (Sects. 3.2.2, 4.1.2, and 4.2). Fine-tipped microelectrodes with outer tip diameter <0.2 µm can be used for intracellular recording from most respiratory motoneurons, whereas stable recordings from preBötC or pFRG interneurons do not seem to be feasible with such "sharp" microelectrodes. Suction electrodes are a pivotal tool for recording spontaneous extracellular neural population activity from the *en bloc* and slice models (Sects. 3.2.1 and 4.1) (5, 18, 40). These electrodes have an outer tip diameter of 50–250 µm depending on the diameters of respiratory active nerve rootlets to which they are mostly attached besides positioning them in active slice regions (Fig. 3). They are pulled from borosilicate glass capillaries (GC-150TF-10; 1.5-mm outer diameter × 1.17-mm inner diameter, Harvard Apparatus). The electrode tip can be grinded down ("beveled") to a desired size with sandpaper or

Fig. 4. (continued) stabilized within some minutes after the rupture of the seal. It is difficult to determine resting V_m in this cell because of its rhythmic fluctuations. Specifically, V_m is slightly more negative than –50 mV during a hyperpolarization after termination of the inspiratory burst and subsequently shows a progressive depolarization until action potential ("spike") discharge occurs in the preinspiratory phase preceding the onset of the inspiratory *VRC* population burst that is accompanied by a synaptic drive potential and further spike discharge in the neuron. Compared to the absence of respiratory-related neuronal activity in the patch electrode recording in **a** shortly before establishing the GΩ seal, recording in **b** showed inspiratory-related inhibition of tonic spiking, indicating that the electrode was close to a "tonic expiratory" neuron in a newborn rat *en bloc* preparation with complete VII nucleus ("[+VII] *en bloc*", see Fig. 1). Within 30 s after the rupture of the seal, the cell showed a very similar discharge pattern and a notable inspiratory-related hyperpolarization. After 5 min of whole-cell recording, this hyperpolarization transformed into a depolarization due to the fact that the patch electrode solution contained, among other components, 144 mM Cl^- ("high Cl^-") which changed the reversal potential for this anion from a value that was originally lower than V_m to a substantially less negative value (details in (59)).

whetstone ("True hard Arkansas whetstone," Fine Science Tools) and fire polished using a commercial lighter and blowing air through the electrode to avoid closure by melting. To prevent tissue damage particularly for recording under visual control using a short distance high-magnification objective (18, 35, 43, 48), electrodes are beveled at an angle (30–45°) to produce a cut tip surface that is parallel to the slice surface. Alternatively, a straight tip electrode is heated and bent down ~45° at its shank to obtain a parallel tip surface and allow maneuvering under the objective. The electrodes are inserted into a patch electrode holder system (ESP-M15-P + MHH-25, Warner Instrument Corp.) (Fig. 3) with an outlet for connecting a suction tube that is attached to a 5-ml standard medical syringe for pressure control via Tygon tubing. Fine-tuning of suction is achieved with a manually tunable syringe (e.g., Gilmont micrometer syringe; www.vwrsp.com) (Fig. 3).

Electrical stimulation, for example, of afferent spinal fiber tracts in the *en bloc* model (37) or the contralateral preBötC in rhythmic slices (Sect. 4.2.4), is feasible with suction electrodes used for extracellular recording. Alternatively, concentric 50–200 µm outer diameter platinum/iridium electrodes can be used such as the PTM3CC02INS or related models from WPI. Under visual control (18, 35, 43, 48) (Sects. 2.8, 3.3, and 4.2.4), single axons or local neural circuits can also be stimulated using a patch electrode filled with standard superfusate after breaking its tip to an outer diameter of 5–10 µm. A broken patch electrode or a triple-barreled microelectrode (3B120F-4 borosilicate glass with 1.2/0.68 mm outer/inner diameter; WPI) can also be used for injection of fluorescent dyes, for example, for Ca^{2+} imaging (Sects. 3.3.2, 3.3.3, and 4.2.4) or pressure application of drugs, respectively (15, 33, 40, 43, 61). These electrodes and double- or triple-barreled ion-sensitive microelectrodes (Sect. 3.2.4) consist of (thin-walled) borosilicate glass capillaries from, for example, Warner Instruments or WPI. The latter company also offers O_2-sensitive (micro)electrodes and compatible amperometers.

Patch electrodes, sharp microelectrodes, and ion-sensitive microelectrodes are fabricated using microelectrode pullers such as the P-1000 (Sutter Instrument Company, Novato, CA, USA; www.sutter.com) or the DMZ (Dagan Corporation, Minneapolis, MN, USA; www.dagan.com). The PC-10 (Narishige International Inc., East Meadow, NY, USA; www.usa.narishige-group.com) is a less expensive alternative but is not designed for pulling sharp (ion-sensitive) microelectrodes.

2.6. Micromanipulators and Antivibration Tables

Patch or sharp microelectrodes are positioned with either an MP-285 (Sutter Instrument Company) or an MX7600 step motor plus digital display of recording depth (Siskiyou Corporation, Grants Pass, OR, USA; www.siskiyou.com) (Fig. 3). For positioning extracellular or stimulation electrodes, less precise and consequently

less expensive, yet reliable, micromanipulators can be used such as the Märzhäuser MM33 or the Narishige MMN-1 (both distributed by ALA Scientific Instruments, Farmingdale, NY, USA; www.alascience.com) (Fig. 3). For positioning electrodes on the XY stage of an upright microscope (Sect. 2.8), YOU-2 (Narishige) or Kleindiek Nanotechnik (Reutlingen, Germany; www.nanotechnik.com) manipulators are well suited. Various companies offer manual or motorized XY stages such as Siskiyou Design Inc. or Luigs-Neumann (Ratingen, Germany; www.Luigs-neumann.com).

If the laboratory floor is sensitive to vibration, intracellular recording requires use of an antivibration table, for example, from Newport (Irvine, CA, USA; www.newport.com) or Kinetic Systems (Boston, MA, USA; www.kineticsystems.com) (Fig. 3). These companies also provide Faraday cages that are necessary in a laboratory environment with electrical noise. The Faraday cage is mounted on the antivibration table and thus electrically shields the microscope, experimental chamber, and manipulators positioned on this table. A simple and less expensive (but often sufficient) system uses a stone or solid metal plate resting on rubber or silicone dampers inside a metal (tool) cabinet serving as Faraday cage.

2.7. Amplifiers, Stimulators, and Computer-Based Data Acquisition

For intracellular electrophysiological recording from respiratory neurons, either a patch-clamp amplifier from the "EPC family" (HEKA Lambrecht, Germany, www.heka.com) or a "sample-and-hold" SEC amplifier (npi electronic, Tamm, Germany; www.npielectronic.com) can be used. The latter company also provides high-impedance amplifiers for ion-sensitive microelectrode recording (Sect. 3.2.4). Suction electrode recording of neuronal population activity with amplitudes of 10–500 μV (mostly <100 μV) is done using an AC-coupled differential amplifier which has a gain of at least 1–10 k and is equipped with band-pass-filtering option (optimally 0.3–3 kHz). Examples are the Model-1700 from AM-Systems (Sequim, WA, USA; www.am-systems.com) or the DAM50 from WPI. For better resolution of <100 μV small signals, it is recommended to integrate the output of this amplifier, for example, by using the MA-821/RSP "Moving Averager" (CWE; www.cwe-inc.com) at a time constant of 20–50 ms (Fig. 4). Electrical signals are sampled into a computer via an interface and acquisition software at rates of 1–4 kHz for suction electrode recording and 4–20 kHz for V_m or membrane current recording. Convenient hardware/software packages are available from HEKA, npi, or Axon Instruments (Molecular Devices; Sunnyvale, CA, USA; www.moleculardevices.com). Commonly used multichannel systems for acquiring electrophysiological data are "PowerLab" (ADInstruments, Colorado Springs, CO, USA; www.adinstruments.com) and "Spike2" (Cambridge Electronic Design Ltd., Cambridge, UK; www.ced.co.uk). In most of these systems, software options are implemented for single-pulse or repetitive

("tetanic" or "train") electrical stimulation. For such stimulation, the output of the interface is connected with an electrical isolation unit, for example, from WPI, AM-Systems, or A.M.P.I. (Jerusalem, Israel; www.ampi.co.il), while the output of that unit is connected with the stimulation electrode.

2.8. Microscopes, Imaging Devices, and Fluorescent Dyes

For optic control or mechanic fixation of a preparation and subsequent microelectrode positioning, a stereomicroscope is used such as the Stemi 2000 (Zeiss), SZXZ (Olympus, Center Valley, PA, USA; www.olympusamerica.com), or the ELZ (SCIENSCOPE, Chino, CA, USA; www.scienscope.com). Visualization of slice areas and microelectrode positioning is facilitated by attaching to these microscopes a simple video camera, for example, from WPI. Alternatively, the stereomicroscope is substituted by a video system equipped with zoom optics. The video signal is displayed on a separate monitor or, using a frame grabber, as an inset on the computer monitor used for controlling the (intracellular) recording (Chap. 3-Moore et al. (54)). For recording under visual control from superficial neurons in slices (18, 35, 43, 48), an upright microscope is needed such as the Zeiss Axioskop 2 FS (or successor) and the Olympus BX61WI (Fig. 3). Such microscopes require a water immersion lens (usually 40× or 60× magnification) with a working distance >1 mm to facilitate pipette positioning. For approaching individual cells, the microscopes should be equipped with differential interference contrast (DIC) optics which makes them appear 3D-like (62) (Chaps. 1-Trapp and Ballanyi (45), 4-Fish et al. (63), 5-Nakamura et al. (64) and 9-Broicher and Speckmann (56)).

Cells located up to 80 μm below the slice surface can be visualized for targeted patch-clamp recording by attaching to the microscope a charge-coupled device (CCD) camera with sensitivity into the near-infrared (IR) spectrum and displaying the acquired IR-DIC image on a monitor. Examples for suitable CCD cameras are "ImageM" or "Orca-R2" (Hamamatsu, Bridgewater, NJ, USA; www.hamamatsu.com) or "CoolSNAP" (Röper, Ottobrunn, Germany; www.roperscientific.de). For patch-clamping cells that are tagged with a fluorescent label such as green fluorescent protein, an epifluorescence system is required. Details of such systems based on CCD camera or photomultiplier imaging are described elsewhere (62) (Chaps. 1-Trapp and Ballanyi (45), 3-Moore et al. (54), 4-Fish et al. (63), 5-Nakamura et al. (64) and 9-Broicher and Speckmann (56)).

For our studies on isolated respiratory networks, we used so far two optical imaging approaches. Fast voltage imaging with a temporal resolution in the order of tens of milliseconds was done in collaboration with the Onimaru group (24). In this study, changes in neuronal activity, which were proportional to changes in fluorescence intensity of the voltage-sensitive fluorescent dye

Di-2-ANEPEQ (Invitrogen, Carlsbad, CA, USA; www.invitrogen.com), were monitored with a CCD camera-based imaging system (MiCAM01, Brain Vision Inc., Tsukuba, Japan; www.scimedia.com) attached to an upright BX50WIF-2 microscope (Olympus). The optical path contained a 150-W tungsten halogen lamp, a 510–550 nm excitation filter, a dichroic mirror, and a 590 nm emission filter (U-MWIG2 mirror unit from Olympus). The imaged area was 4.20×3.25 mm (resolution 180×120 pixels). Differential images were processed with a 3×3 pixel software-spatial filter (BV Analyze, BrainVision Inc.).

Our laboratory was the first to adapt confocal and multiphoton ("2-photon") microscopy to image both activity and morphology of mammalian respiratory neurons (15, 33, 40). For this, we loaded these neurons (and adjacent glial cells) with the membrane-permeant acetoxymethyl (AM) form of the fluorescent Ca^{2+}-sensitive dyes Fluo-4 (TEFLabs, Austin, TX, USA; www.teflabs.com or Invitrogen) or Fluo-8L (ATT Bioquest, Sunnyvale, CA, USA; www.attbio.com). For this, Fluo-4-AM is firstly dissolved in dimethyl sulfoxide containing 20% pluronic acid to 5 mM and then diluted with standard superfusate (Sect. 2.2) to 0.5 mM for tissue injection or to 10 μM for loading via incubation (recently, we use mostly Fluo-8L AM for this). For the latter procedures, a slice is transferred to a 1.8-ml CryoTube (Nunc A/S, Roskilde, Denmark; www.nuncbrand.com) with a Tygon® tube inserted through the lid used for carbogenation of standard superfusate to which the dye is added. Direct contact of the Tygon® tube inlet with the solution is avoided to prevent excessive perturbation of the fluid which causes bubble formation due to the pluronic acid content and may also mechanically stress the slice. The CryoTube is inserted in a heating unit (Isotemp-125D, Fisher), and the dye is loaded for 30 min at 30°C. After entering the cells, the AM component of the Ca^{2+}-sensitive dye is cleaved by esterases rendering dye molecules membrane impermeant and activated for monitoring cytosolic Ca^{2+} dynamics (15, 23, 43, 62).

Activity-related increases in Fluo-4 (or Fluo-8L) fluorescence intensity (Sects. 3.3.2 and 4.2.4) are monitored using either a confocal laser scan microscope and software (20× XLUM-PlanF1-NA-0.95 objective; Olympus FV300, FluoView software) (Fig. 3) or a FV300 connected with a Ti:Sa laser (10 W Mira/Verdi, Coherent, Santa Clara, California, USA; www.coherent.com) for multiphoton imaging (15, 18, 23, 33, 40, 43, 61, 62, 65). The latter microscopes and software are also used by us for sulforhodamine 101 imaging that we have adapted to further improve the resolution of morphological features of preBötC neurons, XII motoneurons, and (some) adjacent glial cells (Sects. 3.3.3 and 4.2.4).

2.9. Histological Procedures

For generating brainstem atlases and anatomically "calibrated" *en bloc* preparations and preBötC slices (Figs. 1 and 2), thionin-stained respiratory marker nuclei were mapped in 50–100-μm-thin serial

brainstem sections (Sect. 3.1). For this, isolated brainstems were fixed for >1 h, typically overnight until several months, in 4% paraformaldehyde in phosphate buffer. Agar-embedded neonatal brainstems (Sect. 2.2.3) were cut with the Leica vibratome (Sect. 2.3) to produce a series of 50-µm-thin slices which were then mounted on glass slides and thionin stained for analysis of marker structures. Specifically, slices were "washed" in phosphate buffer for 2 min, then immersed for 45–60 s in thionin solution (Sect. 2.2.3), and finally washed in 50% ethanol (4 min) and phosphate buffer (2 min). After experiments, rostrally sectioned *en bloc* preparations, preBötC slices, and also 100-µm-thin pre- and postrhythmic slice sections are fixed for at least 15 min (typically overnight) and stained, using the above-described procedure, but exposed to thionin for 105, 90, and 45 s, respectively. For histological analysis, these sections are transferred on a "hanging drop" glass slide (Fisher Scientific) to an upright microscope (Zeiss Standard 16, magnification ×32) (Sect. 2.8) and photographed (PL-A642-1.3Megapixel, PixeLINK, Ottawa, ON, Canada; www.pixelink.com). Stained preBötC slices or *en bloc* preparations are transferred in phosphate buffer to a Petri dish and photographed (PL-A686-6.6-Megapixel, PixeLINK) under a stereo microscope (Zeiss-SR15, magnification ×32) (Sect. 2.8) (Figs. 1 and 2).

For morphological reconstruction of respiratory neurons that were filled during electrophysiological recording with lucifer yellow, biotin or biocytin via the whole-cell patch electrode (Sect. 2.2.3), two techniques can be used. According to the approach of the Onimaru group (24, 51, 52), transverse 100 µm slices of brainstem–spinal cords fixed in Lillie solution (Sect. 2.2.3) are cut with a (Leica) vibratome (Sect. 2.3) and stained in distilled water with 1% neutral red (Sigma-Aldrich) for visualizing marker regions. Morphology and anatomical location of labeled neurons are reconstructed via a camera lucida attached to a fluorescence microscope (BH-2; Olympus) (Sect. 2.8) and comparing marker structures with our newborn rat brainstem atlas, respectively (24). For histological analysis of whole-cell recorded neurons in (>400 µm thick) preBötC slices (53), slices are immersed in 4% paraformaldehyde (in 0.1-M phosphate buffer, pH 7.4) for 4–15 h at 4°C, followed by immersion in 30% sucrose solution (10 h). Slices are then cut in serial transversal sections (100 µm) using a Frigocut (Leica, Germany) and processed for "ABC" staining with horseradish peroxidase and diaminobenzidine (both Sigma-Aldrich). Sections are mounted on slides, and cells are examined with a light microscope (for biotin/biocytin staining) or a fluorescence microscope (for lucifer yellow staining). For live-cell labeling of XII motoneurons and (primarily) neurons in the preBötC area, slices are incubated with 0.01% (165 µM) sulforhodamine 101 (in the dark) at 20–23°C for 1–1.5 h in carbogenated standard solution and then analyzed using the multiphoton/confocal imaging stations (Sect. 2.8).

2.10. Agents

Most agents for our studies on respiratory networks in the dish are obtained from Sigma-Aldrich except salts for superfusate, Na^+-acetate trihydrate, or acetic acid (Fisher Scientific). Other agents, mostly neurotransmitters and corresponding (ant)agonists, are mostly available at Tocris Bioscience (Ellisville, Missouri, USA; www.tocris.com), MP Biomedicals (www.mpbio.com), TEFLabs Inc. (Austin, Texas, USA; www.teflabs.com), or Alomone Labs Ltd. (Jerusalem, Israel; www.alomone.com). Fluorescence dyes are purchased from Invitrogen, ATT Bioquest and TEFLabs Inc.

3. Methods

In this section, techniques are described for generating anatomically defined *en bloc* and slice preparations in which respiratory activity is preserved for up to >1 day, while some basic procedures for isolating newborn rodent brainstems or their histological analysis have been described above (Sect. 2.2). Reference is also made here to microelectrode-based extracellular recording of neuronal population plus intracellular activities or dynamic changes of extracellular ions, PO_2 or PCO_2. Finally, morphological, voltage, and Ca^{2+} imaging at the (sub)cellular level plus spatiotemporal optical activity patterns in respiratory neuron populations are dealt with.

3.1. Generation of Calibrated Respiratory Networks in the Dish

Methods for generating transversal preBötC slices vary notably between laboratories, for example, regarding brainstem sectioning in rostral-to-caudal versus caudal-to-rostral direction or their rostrocaudal thickness ranging from 200 μm to >1,000 μm (18, 34). Moreover, previous studies did not provide histological proof of slice margins, and minimal margins sufficient and necessary for rhythm in these slices were also not determined until we addressed these issues (40) (Sect. 4.2.1) (Figs. 1 and 2). In the following, we (1) describe procedures for obtaining brainstem atlases for newborn rats and mice (Sect. 3.1.1), (2) outline how these atlases are used for identifying "respiratory marker" structures for "online histology" during live brainstem sectioning for generating preBötC slices with defined and reproducible anatomical boundaries (Sect. 3.1.1), and (3) describe how "calibrated" *en bloc* preparations are generated based on procedures outlined under (1) and (2) in concert with our analysis of ventral brainstem surface landmarks (Sect. 3.1.3). Experiments were performed in accordance with guidelines by the Canadian Council on Animal Care and were approved by the Health Sciences Animal Policy and Welfare Committee of University of Alberta.

3.1.1. Newborn Rat and Mouse Brainstem Atlases

For generating calibrated preBötC slices from commonly used P0-4 Wistar and Sprague-Dawley rats (33) and P0-7 C57BL/6 mice (41), we firstly showed that the rostrocaudal extents of anatomical marker structures associated with the yet solely functionally defined preBötC do not change during P0-4 for rats, whereas growth was evident between P0 and P6 mice. The brainstem marker structures include the VII motor nucleus, the lateral reticular nucleus, and in particular the "loops" (in coronal sections) of different subnuclei of the inferior olive, which are most pronounced in the rostrocaudal axis at the center of the preBötC (Figs. 1 and 2) (see also *Supplemental Web Material* including brainstem atlases in (33, 34, 41)). Less valuable information is obtained from dorsal marker regions such as the XII nucleus or the obex (i.e., the opening of the fourth ventricle) because their association with ventral structures depends on the cutting angle. However, this particularity can be used for quantifying such a "tilt" by comparing ventral and dorsal marker areas. Similarly, discrepancies between ventral marker structures on each brainstem side provide information on the extent of a possible lateral tilt. Motoneurons of the *nucleus ambiguus* do not aggregate to a detectable marker in live thin transversal brainstem sections, at least in our hands, and are therefore not a useful marker structure for our online histology approach (Sect. 3.1.2).

We analyzed the rostrocaudal extents of marker structures in 50-µm-thin thionin-stained transversal serial sections from agar-embedded paraformaldehyde-fixed brainstems (Sect. 2.9). The rostrocaudal position of each section was defined by its distance (in mm) from the caudal end of VII nucleus, introduced (Sect. 1) as "VII_c," with regions caudal to VII_c assigned negative values (Figs. 1 and 2). Also, serially sectioned 100-µm-thin slices from live brainstems kept in standard superfusate were stained with thionin and photographed. This analysis revealed that the rostrocaudal extents of marker nuclei (Fig. 2) and also the distance between the rostral margin of VII nucleus and the caudal end of the medial inferior olivary nucleus were identical. This was regardless of whether comparisons were made between rat strains (Wistar vs. Sprague-Dawley), age groups (P0 vs. P2 and P4), or live versus fixed sections. The constancy of these marker nuclei, both in absolute dimension and position relative to each other, allowed construction from a single representative 2 Wistar rat brainstem of a "reference atlas" comprised of 50-µm-thin serial transections. This atlas is applicable to P0-P4 Wistar and Sprague-Dawley rats (see *Supplemental Web Material* in (33)). Anatomical relations of the marker nuclei with respiratory brainstem regions, specifically the VRC including the pFRG, the preBötC, and the area corresponding to the Bötzinger complex (BötC) in adults, and some atlas sections are shown in Figs. 1 and 2. We reported (41) that, compared to P0-4 rats, the rostrocaudal marker structure extents are smaller (in particular at

P0) in inbred C57BL/6 mice that are often used for genetic engineering (16–19). For C57BL/6 mice at P6, marker structures also apparently differ with those in another developing mouse brain atlas based on 120-µm sections from a single brainstem of an unspecified mouse strain (66). The 50 µm resolution in our mouse atlas (41) provides details on brainstem marker structures that are necessary for generating calibrated slices.

Three conclusions can be drawn from our findings: (1) Neither our rat atlas nor the mouse atlas by Paxinos et al. (66) can be used for generating calibrated preBötC slices from C57BL/6 mice. Consequently, research groups that routinely use a mouse strain other than C57BL/6 (or a rat strain other than Wistar or Sprague-Dawley) should generate a reference atlas for that strain. (2) Our histological findings suggest that rhythmic slices of identical thickness from newborn rats versus mice contain a different portion of the VRC and other brainstem structures that may differentially modulate preBötC activity. Specifically, we found that the distance between the rostral margin of VII nucleus and the caudal margin of the inferior olive is ~1.5-fold larger in P0-4 rats versus P0 mice. This suggests that, at a thickness of 500–800 µm, P0-2 (C57BL/6) mouse slices used by numerous groups (2, 10, 13, 14, 18, 31, 32, 41) contain similar brainstem structures as 750–1,200-µm-thick newborn rat slices. (3) A >1,000-µm-thick newborn rat slice and a >650-µm-thick P0 mouse slice would likely include the entire preBötC plus a major portion of the (caudal aspect of the) pFRG, if the preBötC would be located close to their caudal margin (see Fig. 1 in (18)).

3.1.2. Calibrated preBötC Slices

Calibrated preBötC slices are generated according to procedures described in our original report (33). For this, animals are anesthetized with 100–200 µl isoflurane added to a small beaker with lid (Sect. 2.3) until the paw withdrawal reflex disappears. They are then decapitated at a level close to the shoulder, which ultimately provides a spinal cord length up to the first thoracic segments. Next, the brain plus rostral segments of the cervical spinal cord are isolated at 18–20°C in standard superfusate (Sect. 2.2). After removal of the cerebellum, the brainstem is transected between the fifth and sixth cranial nerves and just rostral to the C_1 spinal cord segment. For obtaining complete 200 µm or thinner slices as described below, it is pivotal to remove ("unzip") at that stage with a fine forceps (Sect. 2.3) the arachnoid layer, which is the component of the meningeal membranes that loosely ensheathe the brainstem. The brainstem block is then fixed with a thin layer of commercial grade cyanoacrylate glue rostral side down to a metal plate that is subsequently transferred to a Leica vibratome (Sect. 2.3). The plate is fixed in the slicing chamber that is afterward filled with standard superfusate (18–20°C) that is continuously carbogenated via a small gas dispersion tube (Sect. 2.2).

The brainstem block is sectioned, initially in 200–400 μm steps, in caudal-to-rostral direction starting at the caudal end of the inferior olive (Fig. 2). Each section is inspected using a microscope (Sect. 2.8) for comparing marker structures in the living tissue with those in the reference brainstem atlas (Sect. 3.1.1). Varying the focus plane and/or the condenser aperture reveals the medullary marker nuclei, particularly diverse subnuclei of the inferior olive (Figs. 1 and 2). Using such online histology, section thickness is reduced to 100 μm when approaching the desired level for generating a rhythmic slice. At that stage, it is particularly important to adjust the Leica vibratome (Sect. 2.3) to cut close to both the slowest speed of forward blade movement (0.05 mm/s, which takes >1 min per single slice section) and the highest frequency of lateral blade movement (~100 Hz). This is to avoid partial disintegration of the slice and to minimize damage of cells in superficial layers of the rhythmic slice. After cutting the preBötC-containing slice, 100–200-μm-thin "postrhythmic" sections are cut and photographed for determining the rostral border of the rhythmic slice (Figs. 1 and 2). For more detailed "off-line" analysis of slice margins, pre- and postrhythmic sections are fixed and stained with thionin (Sects. 2.9 and 3.1.1) (Figs. 1 and 2). For estimating the boundaries of the prospective rhythmic slice, it needs to be considered that the slicing procedure disintegrates a tissue layer of several tens of micrometer thickness. The predicted margins of calibrated preBötC slices vary by about ±50 μm due to the above-mentioned reasons and related to the fact that the extent and position of marker structures vary slightly between individual brainstems.

In our initial study (33), we generated calibrated slices that would likely contain in their middle the preBötC whose rostrocaudal thickness has originally been estimated to be ~200 μm, with its center located ~0.5 mm caudal to VII_c (7). According to terminology introduced in our study (33), a 400-μm-thick slice from a P4 Wistar rat with the preBötC in the middle and the caudal boundary located 0.8 mm caudal to VII_c is labeled "m-preBötC[400/–0.80]W-P4 slice" (Fig. 2). Corresponding m-preBötC slices from C57BL/6 mice were generated in a further study from our group (41). We also used (175–700 μm thick) newborn rat m-preBötC slices in one section of our study on identification of necessary and sufficient margins of preBötC slices for inspiratory rhythm (40) (Sect. 4.2.1) (Fig. 2). For the latter analysis, we developed two additional types of 700-μm-thick slices, in which the preBötC was located close to one slice boundary or was even partially exposed to the superfusate. In addition to the preBötC, these slices thus contained a notable amount of either rostral or caudal brainstem tissue. They were consequently labeled "r+preBötC[700]" and "c+preBötC[700]" slices, respectively, with the additional attributes of distance from VII_c of caudal or rostral slice surface, respectively, plus rat strain and age (see above) (Fig. 2) (Sect. 4.2.1).

3.1.3. Calibrated Brainstem–Spinal Cords

Different types of perinatal rodent brainstem–spinal cord preparations are available for studying the preBötC, the pFRG, their mutual interactions and/or properties of cranial versus spinal motor networks that are driven by either constituent of the dual respiratory center (Sects. 1 and 4.2.1) (Fig. 1). Our group uses primarily newborn Wistar or Sprague-Dawley rats for this research. For generating the *en bloc* models, animals are anesthetized with isoflurane until disappearance of the paw withdrawal reflex (Sects. 2.3 and 3.1.2). Following decerebration, the neuraxis is isolated at 18–20°C in standard superfusate, which contains 30 mM glucose instead of 20 mM typically used by us for calibrated slices (Sects. 2.2, 3.1.2, and 4.2.2). As described for generating rhythmic slices (Sect. 3.1.2), it is important to remove with fine forceps the arachnoid layer from the brainstem and spinal cord. If not removed, the arachnoid layer may act as a diffusion barrier and would also hamper microelectrode insertion into the ventral brainstem or spinal cord aspects.

We use three types of *en bloc* models. The first type, in which the preBötC interacts with the pFRG, is anatomically closely related to the preparation originally described by Suzue (4) (see also (5, 6)) (Fig. 1). For its generation, the isolated brainstem is transected rostrally, just rostral to the caudal cerebellar artery, and thus contains the complete VII motor nucleus ("*en bloc* [+VII] model"). In most studies, the spinal cord is partially exposed via laminectomy and then cut at the last cervical (C_8) or first thoracic (T_1) level. If the lumbar motor output of the pFRG is to be studied, the complete spinal cord is isolated (21, 22, 28). For investigating, for example, whether stimulatory neuroactive agents, such as caffeine, serotonin, or the ionotropic glutamate receptor agonist N-methyl-D-aspartate, induce hyperexcitability primarily in respiratory or rather nonrespiratory motoneurons, "classical" Suzue-type *en bloc* [+VII] preparations are isolated with the cervical and brachial plexuses attached for recording from the fourth cervical root (C_4), the contralateral phrenic, and the musculocutaneous (or brachial) nerves (Figs. 1 and 5). Inspiratory active cervical roots (C_1–C_8) contain axons from both inspiratory and nonrespiratory motoneurons, whereas the phrenic nerve contains solely axons from inspiratory (phrenic) motoneurons located in spinal segments C_3 to C_6, while the musculocutaneous nerve contains only nonrespiratory axons (5, 67, 68). In this model, it is possible to evoke fictive locomotion by combined bath application of serotonin and N-methyl-D-aspartate (for references, see (28)) (see also Chap. 15-Mandadi et al. (69)). Figure 5 shows that these agents induce, following an initial period of tonic discharge, (bilaterally alternating) fictive locomotor activity in several ventral nerve roots, whereas phrenic nerve activity is not much perturbed.

Finally, we use calibrated *en bloc* preparations (Fig. 1) in which manual brainstem transection with a razor blade aims to expose the

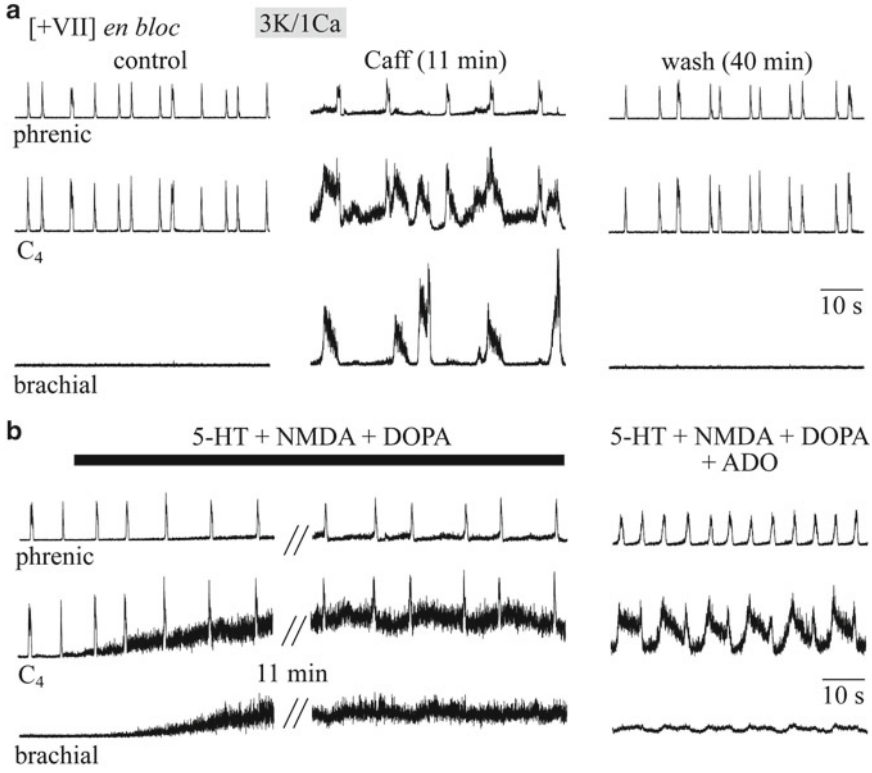


Fig. 5. Differences in fictive inspiratory and locomotor bursting between cervical nerve roots and phrenic plus brachial nerves in the *en bloc* model. (**a**) Suction electrode recording from phrenic nerve in the Suzue-type brainstem–spinal cord preparation with complete VII nucleus ("[+VII] *en bloc*") revealed inspiratory-related bursting very similar to that in the most commonly recorded C_4 root, whereas no activity occurred in brachial nerve not containing axons from respiratory motoneurons. Both, brachial nerve and C_4 root showed reversible (synchronous) massive bursting 11 min after start of application of caffeine (10 mM), whereas inspiratory phrenic activity was only slightly perturbed. (**b**) After recovery from caffeine, the same preparation was exposed to a "neuromodulator cocktail" comprised of serotonin (*5-HT*, 10 μM), N-methyl-D-aspartate (*NMDA*, 5 μM), and dopamine (*DOPA*, 100 μM). This induced massive tonic activity in C_4 root and brachial nerve, whereas phrenic inspiratory rhythm was barely affected even when slow rhythmic bursting occurred in particular in brachial nerve as indication of chemically evoked fictive locomotion. After several applications of different concentrations of neuromodulators (not shown), a very regular fictive locomotor pattern was revealed in the presence of 10 μM *5-HT*, 5 μM *NMDA*, 500 μM *DOPA*, and 1 mM adenosine (*ADO*). These findings show firstly that C_4 recording of inspiratory activity can be contaminated by nonrespiratory bursting that is much less pronounced in phrenic nerve. Secondly, this demonstrated that this preparation is principally suitable of analyzing cervical respiratory and locomotor networks simultaneously.

preBötC more or less to the cut surface. For newborn rats, we found that the extension of the preBötC between –0.4 and –0.6 mm caudal to VII_c is identical with that area on the ventral brainstem surface, from which the most rostral XII nerve root originates (34) (Fig. 1). In this transected *en bloc* model, the pFRG does not seem to be active as indicated by absence of pre-/postinspiratory activity in the two most rostral lumbar nerve roots containing axons from motoneurons that drive abdominal expiratory muscles (8, 22, 28, 34). For these reasons, transection should be

done slightly rostral to the most rostral XII root, if an *en bloc* [–VII] preparation is to be studied in which the preBötC is not subject to a major influence from the pFRG (Sect. 4.2.1). The spinal cord is either transected at the midcervical level or completely dissected (which takes ~15 min longer). As with the other models, suction electrodes can be used for simultaneous recording of inspiratory-related rhythms from ventral spinal nerve roots. Normally, the lumbar roots in these transected *en bloc* [–VII] preparations are not active or show small-amplitude inspiratory activity (28, 34). Moreover, suction electrodes can be positioned in the ventrolateral aspect of the cut medullary surface containing the VRC with the more- or less-exposed preBötC, and also in the XII motor nucleus, which is though rather small at this rostral level (Fig. 1). Figure 1 also shows that thionin staining of the (chemically fixed) transected *en bloc* model after the experiments enables determination of its rostral boundary by comparison with the reference brainstem atlas. For some studies, it may be intended to use *en bloc* preparations in which a defined amount of tissue is preserved rostral to the preBötC, for example, the area corresponding to the BötC in adults (1–3) (Sect. 1). We determined for newborn rats that the vagal nerve is located on average 0.06 mm caudal to VII_c (34). This is the area in which the caudal aspect of the pFRG may overlap with the BötC (Fig. 1).

The location of the caudal cerebellar artery matches well with that of the rostral border of VII nucleus, that is, 0.74 mm versus 0.76 mm rostral to VII_c, respectively. The latter surface landmark may delineate an important part of the rostral aspect of the pFRG that may also be relevant for respiratory control, at least in newborns (28, 29, 34) (Sect. 1). For preparations transected between VII_c and the rostral end of the inferior olive, there are no marker nuclei to help determine the rostral boundary. In these cases, thionin-stained sagittal sections are generated from the transected and fixed rostral brainstem aspect for identifying the distance of VII_c from the caudal boundary of the rostral brainstem block. Based on this, the rostral boundary of the transected *en bloc* model can be calculated. For further information on anatomical properties of the calibrated *en bloc* model, see the original report (34).

3.1.4. Influence of Temperature and Preparation Time on Respiratory Rhythms

For slices studied in 3K/1Ca, and *en bloc* preparations in general, the closest possible range compared to in vivo of the temperature in the recording chamber is 25–27°C (Sect. 2.4). At >30°C, inspiratory-related bursting ceases irreversibly within <1 h in the *en bloc* [+VII] preparation as indicated by our unpublished results, while rhythm may also not be stable at temperatures <22°C. Similarly, we found that rhythm of calibrated preBötC slices in 3K/1Ca is "washed out" spontaneously within <0.5 h upon increasing the temperature in the recording chamber from 27°C to 37°C. However, as tested by us in m-preBötC slices of <700 μm

thickness, bursting is reactivated by increasing K^+ to 7 mM and remains stable for >5 h. Similarly, mouse preBötC slices can be studied in 8K/1.5Ca at physiological temperature and even during "in vitro fever" (32). We use standard superfusate at 18–20°C for brainstem-spinal cord dissection and slice generation. We did not find any obvious advantage of using ice-cold standard solution or modified solution that may improve the viability of slices or *en bloc* models from other brain regions (see also other chapters of this book and Sects. 2.2 and 5).

When a temperature of 25–27°C is maintained in the recording chamber, cervical inspiratory-related rhythms in the *en bloc* model in 3K/1Ca solution last often >10 h, regardless of whether preparation time was 15 min or up to 2 h. Contrary, pFRG bursting, pFRG-driven cranial plus spinal (motor) activity, and cranial preBötC-driven motor activities may depend substantially on preparation time (Sect. 5.2). The average time for generating a calibrated slice by an experienced experimenter ranges between 35 and 45 min, while noncalibrated slices can be obtained within 15–25 min, mainly depending on how fast slicing is done (Sect. 2.3). Preparation time is not critical for the capability of the slices to generate inspiratory rhythm in high K^+, while the "longevity" of rhythms in 3K/1Ca decreases notably when it takes >1 h to obtain a slice. Importantly, no recovery time from the isolation/cutting procedures is necessary for either the *en bloc* or slice models.

Within <10 min after transferring a preparation to the recording chamber and start of the superfusion pump, respiratory activities are present in either 3K/1Ca or high-K^+ solution while their amplitudes may still develop during the first 30 min of recording. Only when <300-μm-thin slices are used or slices are generated in solution with <10 mM glucose, it may take up to 30 min until robust rhythm develops (in 3K/1Ca).

3.2. Electrophysiological Recording and Stimulation

Suction electrode recording is the most widely used electrophysiological approach for studying respiratory networks in the dish (Sect. 2.5) (Figs. 2, 4, 5, 6, 7, 8, 9, 10, and 11). Importantly, suction electrodes can be applied not only to proximal cut ends of ventral nerve roots but also to other inspiratory active structures such as the VRC region and XII motor nucleus in preBötC slices. Besides, they can be used for electrical stimulation (Sects. 2.5 and 4.2.4). Our group pioneered two decades ago the use of ion- and gas-sensitive microelectrodes for in vitro analyses of the ionic microenvironment of respiratory structures (37). Moreover, we were the first to adapt 10 years ago "blind" patch-clamp techniques for analyzing biophysical membrane properties of respiratory neurons (7, 9). Currently, whole-cell recording from respiratory neurons using either the blind approach for cells located deeper within brainstem tissues or visually targeted recording from (fluorescent protein-expressing) cells in superficial tissue layers is to an increasing

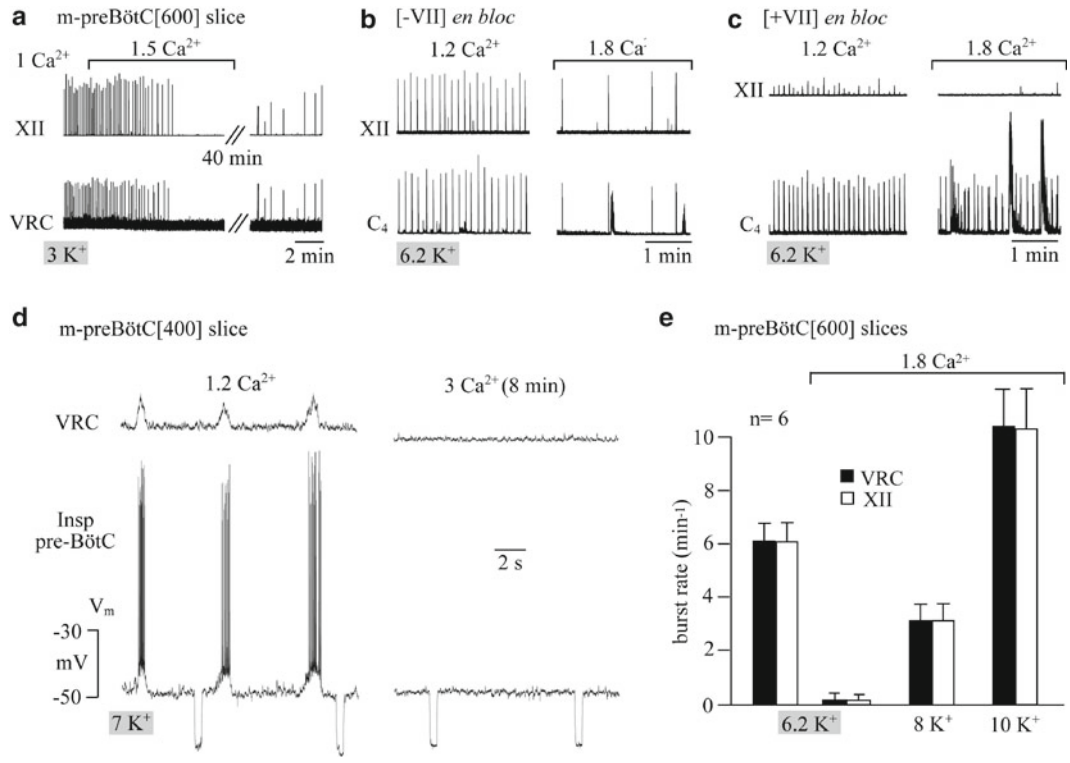


Fig. 6. Ca^{2+}/K^+ antagonism of isolated preBötC bursting. (**a**) In an m-preBötC[600/−0.85]W-P1 slice, raising superfusate Ca^{2+} in 3 mM K^+ from 1 to 1.5 mM abolished inspiratory bursting in both the VRC/preBötC area and *XII* nerve, and this effect reversed only partially even after >40 min following return to 1 mM Ca^{2+}. (**b**) In a brainstem–spinal cord preparation without VII nucleus transected close to the rostral preBötC boundary ("[–VII] *en bloc*"), raising Ca^{2+} from 1.2 to 1.8 mM in 6.2 mM K^+ greatly depressed inspiratory-related C_4 and *XII* nerve bursting. (**c**) In a brainstem–spinal cord preparation with complete VII nucleus ("[+VII] *en bloc*"), raising Ca^{2+} from 1.2 to 1.8 mM in 6.2 mM K^+ did not block C_4 rhythm but evoked nonrespiratory cervical discharge (compare Fig. 5). It may appear that high Ca^{2+} blocked *XII* bursting, but depression of this rhythm, which is typical for that model, started already before changing to high-Ca^{2+} solution. (**d**) In an m-preBötC[400/−0.70]W-P2 slice, raising Ca^{2+} from 1.2 to 3 mM in 7 mM K^+ abolished both inspiratory-related VRC bursting and concomitant bursting in a preBötC inspiratory neuron. This blockade occurred without postsynaptic effect on V_m or membrane resistance measured by repetitive injection of negative DC current pulses causing a hyperpolarization of V_m. This indicates that the inhibitory Ca^{2+} effect on the isolated preBötC is primarily of presynaptic origin. (**e**) In 6 m-preBötC[600/−0.86] slices, strong depression of inspiratory-related *VRC* and *XII* bursting due to raising Ca^{2+} from 1.2 to 1.8 mM was countered by raising K^+ from 6.2 to 8 and 10 mM (For details, see (18, 34, 42)) (**a**–**c**, **e** with kind permission from (34), **d** with kind permission from (42)).

extent combined with genetic or acute fluorescence labeling of respiratory neuron populations for identifying their genetic origin and for Ca^{2+} or voltage imaging (Sects. 3.3 and 4.2.4).

3.2.1. Suction Electrode Recording

Extracellular AC-coupled signals obtained with a suction electrode connected to a differential amplifier are typically in the low millivolt range, often as small as 10–100 μV (Sect. 2.7) (Fig. 4). These signals are thus very sensitive to electrical noise, which may require the use of a Faraday cage (Sect. 2.6), while it is recommended to record and display them as a moving average "integrated" trace for

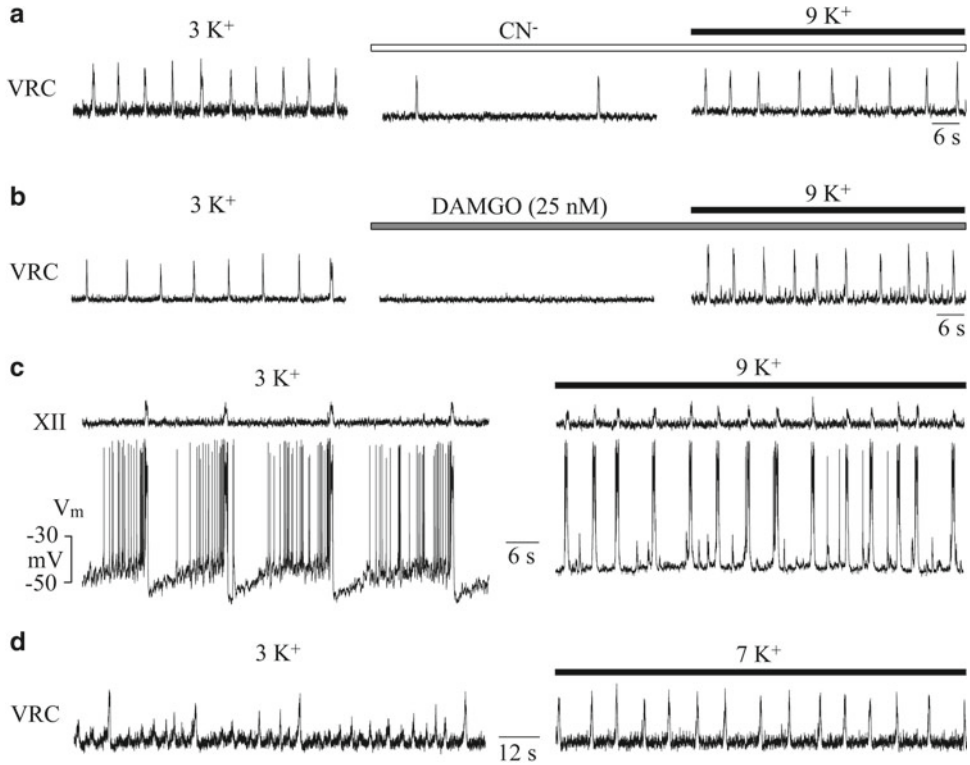


Fig. 7. Modulatory effects of superfusate K^+ on in vitro inspiratory activities. (**a**) In an m-preBötC[600/−0.85]W-P3 slice, substantial slowing of *VRC* bursting due to chemical anoxia evoked by bath application of cyanide (CN^-, 1 mM) was countered by raising superfusate K^+ from 3 to 9 mM. (**b**) In a different m-preBötC[600/−0.83]W-P3 slice, blockade of *VRC* rhythm by the μ-opioid receptor agonist [D-Ala2, N-MePhe4, Gly-ol]-enkephalin (*DAMGO*) was countered by increasing K^+ from 3 to 9 mM. (**c**) Raising K^+ from 3 to 9 mM in an m-preBötC[500/−0.80]W-P2 slice not only greatly accelerated the rate of rhythm but also changed the V_m trajectory in an inspiratory preBötC neuron notably. (**d**) Increasing K^+ from 3 to 7 mM reconfigured *VRC* bursting in a preBötC[500/−0.75]SD-P2 slice from a mixed pattern of fictive eupnea and fictive sigh bursts to a regular burst pattern.

a better signal-to-noise ratio (Sect. 2.7) (Fig. 4). Suction electrodes of apparently identical shape can differ notably in the capability of recording particularly small signals. Prior to starting a series of experiments, it is thus recommended to prepare a set of about ten such electrodes and record rhythmic bursting in a test *en bloc* preparation or preBötC slice for choosing the most responsive electrodes. These electrodes can be used for up to several months provided they are cleaned with distilled water after the experiment. For suction electrode recording from a nerve root, the initial (modest) suction may be relieved by disconnecting the syringe from the suction tube (Sect. 2.5) while the electrode is slightly pushed against the brainstem or spinal base of the nerve root. For recording from the cut brainstem surface, the electrode should only make contact with the superficial tissue layer, particularly for recording from the VRC/preBötC in <300-μm-thin slices when the inspiratory center is partly exposed to the recorded surface. Though,

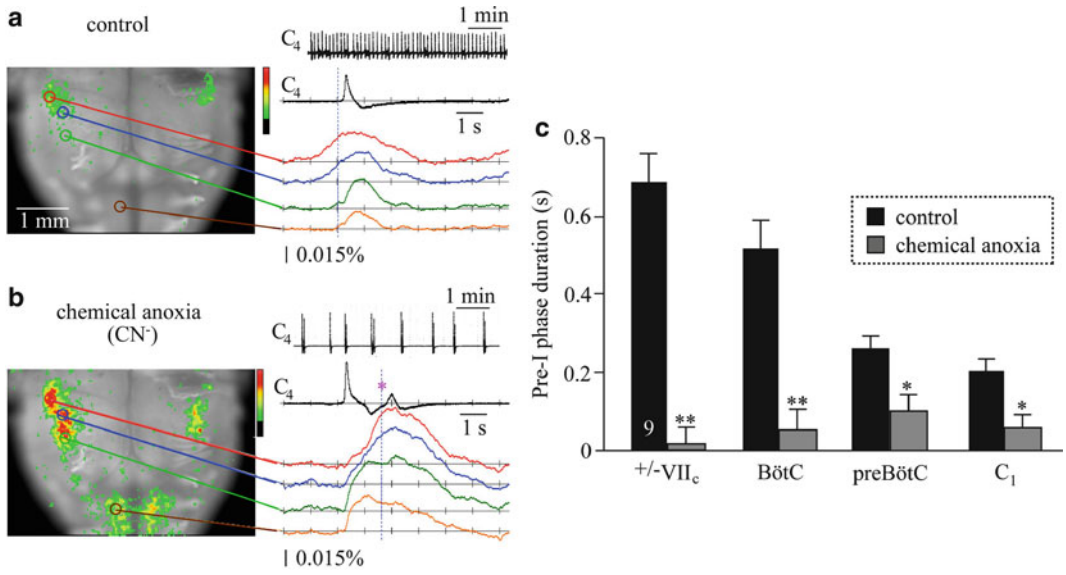


Fig. 8. Shortening by anoxia and prolongation by opioids of delay between onset of preinspiratory (pFRG) and inspiratory (preBötC) network bursting in newborn rat *en bloc* [+VII] medullas. (**a, b**) Simultaneous voltage imaging and electrophysiological cervical inspiratory burst recording during control (**a**) and anoxia (**b**). Averaged (n = 40) imaging pixels in the *left* image summarize respiratory activity immediately at the onset (indicated by *dotted line* in *right panel*) of averaged inspiratory-related integrated cervical root (C_4) burst that was plotted synchronous with kinetics of fluorescence changes in four regions of interest (ROIs). These ROIs were located within [in rostral to caudal direction] the area around VII_c, the *BötC*, the *preBötC*, and the C_1 spinal motoneuron area (for exact location of these areas, see Figs. 1 and 2). Note that preinspiratory activity is particularly evident in the VII_c and *BötC* areas. (**b**) Chemical anoxia due to bath application of CN^- (1 mM) slowed rhythm and evoked double bursts (compare integrated original C_4 recordings in **a**, **b**). Anoxia abolished the preinspiratory phase of optical pFRG activity as shown in the bar graphs of **c** based on measurements in nine preparations. Moreover, anoxia elicited in all regions a prominent second peak of activity during the postinspiratory phase after the augmented initial C_4 peak. Signals were sampled and averaged (n = 20) only upon occurrence of C_4 double bursts during the late phase of chemical anoxia. The peak was attenuated here by averaging due to a variation in the time of its onset ("jitter") (With kind permission from (24)).

recording from the cut surface of the VRC/preBötC area or XII motor nucleus can benefit from gentle suction using a micrometer syringe (Sect. 2.5), which often improves the signal-to-noise ratio greatly. In case of a "leaky" recording with steadily decreasing signal amplitude, it may be necessary to reestablish modest suction every 10–20 min. When recording from calibrated preBötC slices in 3K/1Ca, the amplitude of inspiratory-related XII nerve or nucleus signals may be small and disturbed by random nonrespiratory discharge contrary to pronounced inspiratory activities in elevated K^+. When recording from cranial nerves, such as the XII, VII, or trigeminal nerves in the *en bloc* [+VII] model (Sect. 3.1.3), signal amplitude may progressively and irreversibly decrease for unknown reasons as indicated by our unpublished results on VII and trigeminal bursting and our published findings on unstable XII rhythm (34) (Sects. 4.2.1 and 5). In particular, in the ventrolateral slice aspect, suction electrodes record tonic neuronal population

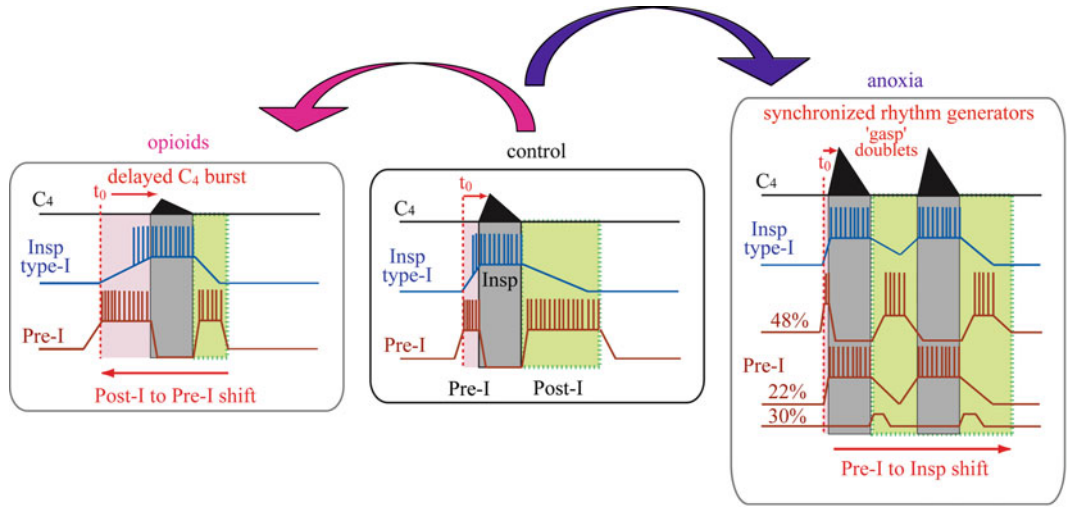


Fig. 9. Opioid versus anoxia effects on onset of pFRG and preBötC bursting. As shown in the box in the *center*, inspiratory motor output is recorded, for example, from C_4 roots. pFRG ("Pre-I") neurons provide preinspiratory drive to type I Insp neurons that may play an important role in triggering the onset of preBötC bursting. *Left box* shows that opioids prolong preinspiratory bursting in Pre-I neurons and concomitantly shorten their postinspiratory bursting compared to control (compare with *center box*). Assuming that pFRG activity starts the respiratory cycle, this effect may be due to delayed generation of inspiratory motor output. As shown in the *right box*, anoxia almost synchronizes the dual respiratory rhythm generator. Accordingly, the preinspiratory drive potential is shortened in type I Insp neurons, whereas Pre-I neurons show three different responses to sustained (10–20 min) anoxia. In 48% of cells, the bursting pattern shifts toward the postinspiratory phase with concomitant depression of the duration of preinspiratory activity and the strength of postinspiratory bursting. In 22% of Pre-I neurons, the activity pattern changes to inspiratory bursting, whereas the remaining 30% are "functionally inactivated" because of greatly depressed drive potentials (and concomitant hyperpolarizations). Not shown in this schema are hypothetic medullary neurons, which develop pronounced postinspiratory activity during anoxia as indicated by the voltage imaging data. The overall enhanced inspiratory/postinspiratory medullary activity during anoxia may be responsible for triggering inspiratory motor bursts, doublets or triplets. More details in (24) (With kind permission from (24)).

discharge in addition to phasic inspiratory-related bursting in the ventrolateral aspect. This becomes most evident in the integrated VRC/preBötC trace (Sect. 2.7) when inhibition of such activity, for example, with opioids, high superfusate Ca^{2+}, or blockers of voltage-activated Na^+ or Ca^{2+} channels, occasionally decreases the baseline of this signal profoundly (18, 42) (Figs. 6 and 7).

3.2.2. Patch-Clamp Recording

Single-channel recording is the original domain of patch-clamp technology (49, 50) that is briefly dealt with elsewhere in this book (Chap. 1-Trapp and Ballanyi (45)). This approach is feasible in the perinatal rodent respiratory networks in the dish as documented by various papers, in particular from the groups of Mironov and Richter (31). Our group has so far only used whole-cell or "perforated" patch-clamp techniques for analyzing electrical properties of respiratory interneurons and motoneurons (7, 9, 42, 46, 51–53, 59, 60, 70–72) (Figs. 4, 6, and 7). Both types of recording modes can be stable for up to several hours (mostly 30–60 min), independent on whether cells are studied in deep tissue layers with blind patch-clamp or have been approached under visual control

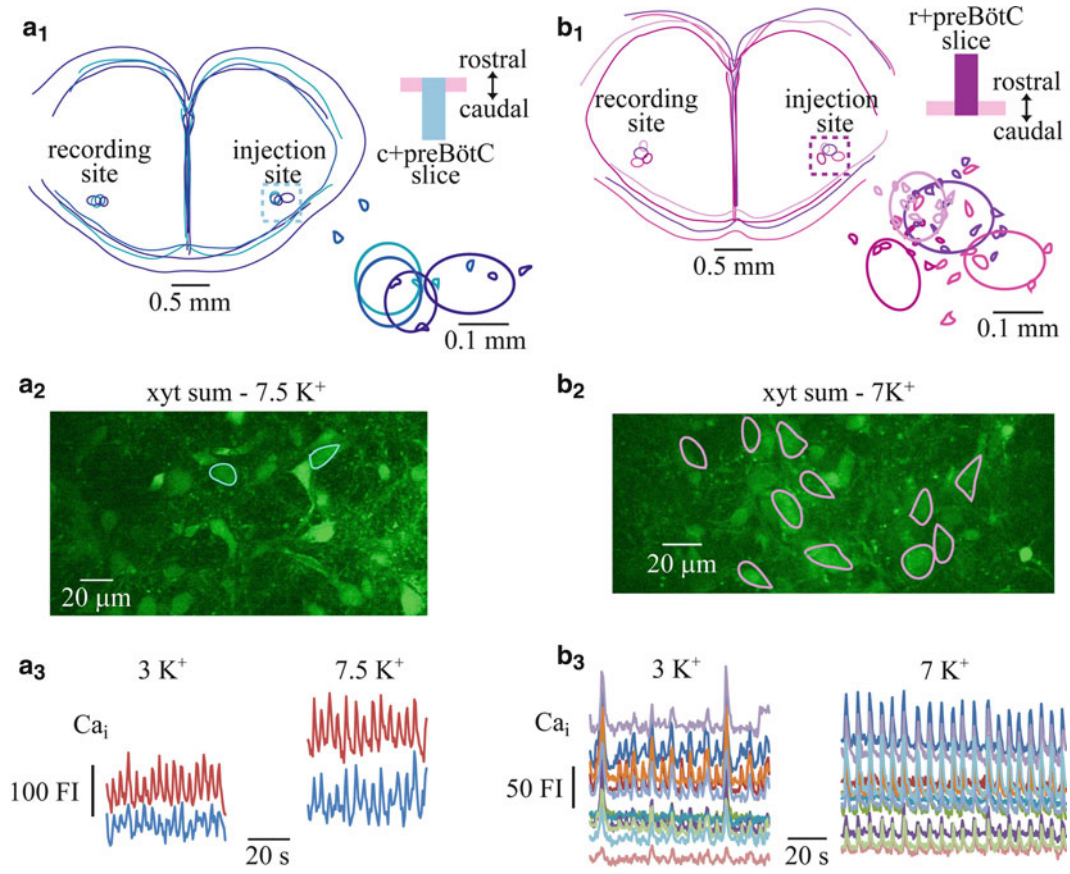


Fig. 10. Multiphoton/confocal Ca^{2+} imaging in the isolated newborn rat pre-Bötzinger complex (preBötC). (**a**) Location, morphology, and activity of active inspiratory neurons in superficial layers (30–80 µm) of slices with the preBötC exposed to the rostral border ("c + preBötC slices"). (**a**$_1$) Locations in four superimposed slices of inspiratory neurons loaded with membrane-permeant Ca^{2+}-sensitive dye (Fluo-4-AM) via pressure injection (25–50 mmHg, 10 min) into the preBötC correspond with positions in contralateral preBötC of suction electrodes for recording inspiratory rhythm with maximal amplitude. Overlapping dye injection sites outlined by *dotted square* are shown in the *lower right inset* at higher magnification. Presumptive inspiratory active neurons are marked by ROIs with equal shading indicating the same injection site (one per slice). (**a**$_2$) Examples for cellular morphology in one injection spot of **a**$_1$ with inspiratory neurons indicated by ROIs. Cells were located 0.43 mm caudal to VII_c, that is, 70 µm rostral to the preBötC center located 0.50 mm caudal to VII_c. (**a**$_3$) Inspiratory-related rises of cytosolic Ca^{2+} (Ca_i) shown by plotting Fluo-4-AM fluorescence intensity (FI) traces over time in the two neurons indicated by ROIs of **a**$_2$ were synchronous with electrophysiologically recorded population bursting in contralateral preBötC (not shown). Raising superfusate K^+ from 3 to 7.5 mM produced more robust oscillations with a concomitant increase in Ca_i baseline (see Movies 1 and 2). (**b**) Location (**b**$_1$), morphology (**b**$_2$), and activity (**b**$_3$) of inspiratory neurons in superficial layers (30–80 µm) of slices with the preBötC exposed to the caudal border ("r+preBötC slices"). (**b**$_1$) Overlapping dye injection sites outlined by *dotted square* are shown in *lower right inset* at higher magnification. (**b**$_2$) Examples for cellular morphology in one injection spot of **b**$_1$ with 11 inspiratory neurons indicated by ROIs. Cells were within the preBötC center at 58 µm caudal to VII_c. (**b**$_3$) Raising K^+ from 3 to 7 mM transformed inspiratory Ca_i rises from a eupnea sigh to regular eupnea pattern in the 11 neurons outlined in **b**$_2$ (see Movies 3 and 4) (With kind permission from (94)).

(18, 35, 43, 48), often using IR-DIC or fluorescence optical approaches (Sects. 2.8 and 3.3).

Whole-Cell Recording: This widely used recording mode has several advantages over sharp microelectrode recording (49, 50) (see also Chaps. 1-Trapp and Ballanyi (45), 3-Moore et al. (54),

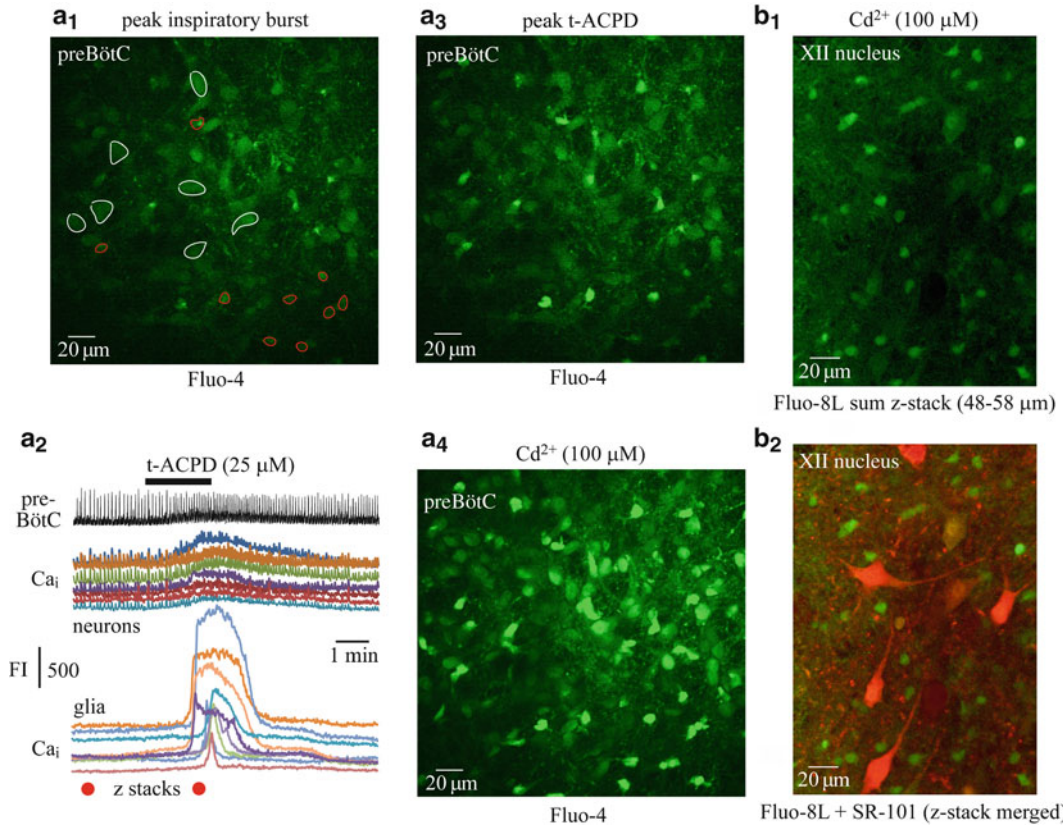


Fig. 11. Morphological and pharmacological discrimination of respiratory neurons and neighboring glia in calibrated preBötC slices. (**a**) In a r+preBötC[400/–0.65]W-P2 slice kept in 7 mM K^+, the presumptive inspiratory neurons, loaded via injection with *Fluo-4*, indicated by white ROIs (**a**$_1$) showed rhythmic Ca_i increases (image taken at the peak of a single inspiratory burst at the time indicated by the *left red dot* in **a**$_2$) that were synchronous with inspiratory population activity in contralateral preBötC (**a**$_2$). Notably smaller cells, presumably representing astrocytes, were sometimes not visible in standard solution, likely indicating a lower Ca_i baseline, and did not show inspiratory-related Ca_i rises. However, such cells (as exemplified by red ROIs in **a**$_1$) responded with a notable Ca_i increase to bath application of the metabotropic glutamate receptor agonist trans-1-aminocyclopentane-1,3-dicarboxylic acid (*t-ACPD*) which accelerated rhythm without a major accompanying Ca_i rise in inspiratory preBötC neurons (**a**$_2$). (**a**$_3$) shows an image at the peak of the response to *t-ACPD* (*right red dot* in **a**$_2$) which reveals that more small (astrocytic) cells are active at this time compared to during the inspiratory peak in control solution in **a**$_1$. (**a**$_4$) Even more presumptive astrocytes could be visualized during the initial 7–10 min of bath application of Cd^{2+} (100 µM) after recovery from *t-ACPD*. Several minutes later also neurons would show an increase in Fluo-4 fluorescence intensity that is due to interaction of the cation with the dye. (**b**) In an m-preBötC[400/–0.80]W-P1 slice kept in 3 K^+ and loaded with *Fluo-8L-AM* via incubation, presumptive astrocytes in XII nucleus became apparent after adding Cd^{2+}. (**b**$_1$) shows summated image from a z-stack (single steps 0.5 µm) between 48 and 58 µm below the slice surface. Contrary, XII motoneurons were only faintly labeled both in control solution and after adding Cd^{2+}. Bath application for 1.5 h at room temperature with 165 µM of the membrane-permeant fluorescent dye sulforhodamine-101 (*SR-101*) stained XII motoneurons (image not shown), whereas glial cells did not accumulate the dye as indicated by lack of appearance of small yellow cells upon merging the green Fluo-4 image in **b**$_1$ with the *SR-101* image (**b**$_2$) (see Movies 5 and 6).

4-Fish et al. (63), 5-Nakamura et al. (64), 6-Stachniak et al. (73), 8-Sanchez-Vives (55), 9-Broicher and Speckmann (56) and 14-Biggs et al. (58)). For example, the recorded cell can more easily be filled with fluorescent dyes for histological analysis and/or imaging (Sects. 2.2.3, 2.9, and 4.2.4). Also, the composition of

the pipette solution can be modified to unmask specific membrane currents. In our study on the distribution of subtypes of voltage-activated Ca^{2+} channels in VRC neurons in the newborn rat *en bloc* model, K^+ in the pipette solution was substituted with Cs^+ and tetraethylammonium$^+$ (TEA^+) for depressing K^+ currents (51) (Sect. 4.1.2). In a more recent study (52), we showed in the same model, for example, that Ca^{2+}-activated K^+ channels are functional in respiratory neurons (Sect. 4.1.2). The extent of activation of these channels and various other cellular processes depend greatly on cytosolic Ca^{2+}, which shows notable fluctuations during activity in these cells (11, 15, 18, 33, 40, 43) (Sect. 4.2.4). Accordingly, it is important to add to the patch electrode solution a Ca^{2+} buffer that mimics endogenous buffering as closely as possible. While some groups prefer ethylene glycol tetraacetic acid (EGTA) in that regard (25, 32, 52), others including us (mostly) use 1,2-bis(o-aminophenoxy)ethane-N,N,N ,N -tetraacetic acid (BAPTA) (7, 9, 11, 31, 42, 53, 59, 60, 70, 71). Both agents are usually applied at a concentration range of 1–11 mM, optimally close to 1 mM to avoid excessive Ca^{2+} buffering in the cytosol. For this reason, some studies preferred not to use either buffer in the patch electrode solution (10–12). Besides, our patch pipette solutions contain Ca^{2+} and also Mg^{2+} as the second physiologically important divalent cation, while 4-(2-hydroxyethyl)-1-piperazine-ethanesulfonic acid (HEPES, mostly 10 mM) is used to buffer pH_i (74). Importantly though, the major relevant physiological intracellular pH buffer is comprised of (dissociated) intracellular CO_2 and HCO_3^- (24–28 mM) provided by the carbogenated standard solution (74). Finally, varying concentrations of Na_2ATP or K_2ATP (usually 1–2 mM) and eventually Na_2GTP (0.2–1 mM) are added to compensate for washout from the cytosol of these important metabolites and/or "second messengers" (49, 50).

According to our experience, the choice between EGTA or BAPTA and 1–11 mM of either agent does not have a major effect on resting V_m, input resistance (R_i), or bursting pattern of newborn rat respiratory neurons in vitro. For these reasons, 1 mM BAPTA is recommended because this presumably approximates the endogenous Ca^{2+}-buffering power (49, 50). Similar to the superfusate, these solutions have an osmolarity of 270–290 mOsmol, which is similar to the value of cellular and interstitial fluids (39). Important to note, long-term whole-cell recording from some types of neurons may require use of slightly hypotonic (85–90%) electrode solution to avoid damage that is presumably due to the pressure of the fluid column in the pipette (Chap. 6-Stachniak et al. (73)).

Perforated Patch Recording: As one disadvantage of whole-cell recording, the low electrical impedance contact between patch electrode and cell interior results in bidirectional diffusional exchange of solute. Therefore, perforated patch-clamp techniques should be applied if the (ionic) composition of the cytosol needs to be maintained. For this, the pipette solution contains ionophores

such as nigericin or gramicidin, which incorporate into the plasma membrane (49, 50). These antibiotics form pores that are primarily permeable to K^+ and H^+ but (mostly) not to Na^+, Ca^{2+}, and most anions or larger uncharged molecules like proteins. After formation of a gigaohm (GΩ) seal (see below) as a pivotal precondition for a stable (perforated) patch recording, the electric "series resistance" (comprised of the electrode resistance plus the resistance between electrode and cytosol) decreases progressively from several hundred MΩ to 40–100 MΩ to reveal a V_m of at least –40 mV and overshooting (rhythmic) action potential discharge. Even at steady state, values for series resistance and R_i are though notably higher for perforated patch than whole-cell recording. This can be problematic for space clamp in (fast) voltage-clamp recordings (Chap. 3-Moore et al. (54)). Perforated patch recordings are also more time consuming because it may take 10–30 min from GΩ seal formation until a sufficient number of channels are integrated into the membrane to allow V_m or I_m recording (49, 50, 59).

A critical step is to figure out empirically the optimal concentration of the ionophore in the pipette solution (Sect. 2.2.2), considering that this concentration may change slightly even from day to day by unknown reasons. In studies referred to in Chap. 1-Trapp and Ballanyi (45), the group of Dr. S. Trapp (Imperial College, London, UK) used solubilized amphotericin B (Sigma-Aldrich) and added it to the pipette solution at a final concentration of ~137 μg/ml freshly every day. Contrary, we used a gramicidin-based solution (Sect. 2.2.2) for a perforated patch recording study on synaptic inhibition in the dual respiratory network in the newborn rat *en bloc* model (59) (Fig. 4) (Sect. 4.1.2).

In the latter study (59), the Cl^- content of the electrode solution was crucial for elucidating whether Cl^--dependent inhibitory postsynaptic potentials in newborn respiratory neurons are depolarizing as in immature cortical neurons (46, 48, 75) (Chap. 11-Kantor et al. (57)). Spontaneous or intended rupture of the perforated patch was evident from a positive change by ~10 mV in the apparent resting V_m likely due to a liquid junction and/or "Donnan" potential (51, 59) plus reversal of spontaneous inhibitory postsynaptic potentials within few minutes (Fig. 4). This indicated that intracellular Cl^- in newborn rat respiratory neurons is similarly low as in adult respiratory neurons (46). Consequently, most groups studying postnatal respiratory networks use now <10 mM Cl^- in whole-cell patch electrode solutions. This is only one example showing that diffusional exchange between patch electrode and the cytosol modifies basic biophysical properties of neurons in isolated brain tissues (for other examples, see Chaps. 1-Trapp and Ballanyi (45), 3-Moore et al. (54) and 7-McKay et al. (76)).

Approaching Respiratory Neurons for Patch-Clamp Recording: For blind patch recording from respiratory neurons in slices, the electrode is advanced perpendicularly using an MX7600 motor-driven

micromanipulator with added display of recording depth, both from Siskiyou (Sect. 2.6), into the preBötC region that is not used for VRC suction electrode recording (Sect. 3.2.1). Inspiratory neurons (the main type of respiratory cells particularly in thin preBötC slices) are identified by their rhythmic extracellular discharge that is in phase with contralateral suction electrode-recorded VRC population bursting (Fig. 4). For blind patch recording in the *en bloc* model from >P1 old animals, it is important to remove the arachnoid and some portion of the pia that cover the brainstem surface to avoid electrode clogging (Sects. 3.1.2 and 3.1.3). Removal of pia is achieved, for example, via scratching using an unfilled patch pipette controlled by a joystick such as used for several types of hydraulic micromanipulators from Narishige. For patch recording under visual control, we use either the MX7600 or the similar motor-driven MP-2 (Sutter) (Sect. 2.6).

While advancing the electrode through the tissue, positive pressure (~30 mmHg) is applied to avoid clogging which is evident from an increase in its electric resistance (7, 9, 35, 48, 50). Independent on the type of patch recording (blind vs. visually targeted), augmentation by up to 300% of a voltage signal in response to repetitive injection at a rate of 25 Hz of negative DC current pulses (−1 nA, 10 ms) indicates that the electrode is close to a neuronal cell membrane (Fig. 4). The probability for a good GΩ seal seems to correlate in this situation with the occurrence during the current injection of electrode potential oscillations that resemble sine waves. At this instance, the patch electrode is moved upward and downward by 1–5 μm several times until the amplitude of electrode potential oscillations becomes maximal. At this point, the pulse is attenuated to −0.1 nA and positive pressure is then removed from the patch pipette (Fig. 4). In ~30% of cases, a GΩ seal develops spontaneously within <5 s as evident from an increase in the amplitude of the current-induced electrode potential change (Fig. 4). If the potential does not start to continuously increase upon removal of positive electrode pressure within this time period, negative pressure of up to −50 mmHg is applied to facilitate GΩ seal formation.

After formation of a seal >1 GΩ, the whole-cell configuration is established by abrupt and brief suction (~100 mmHg) (Fig. 4). If patch electrodes are not "perfect," for example, by corrosion of the filament of the electrode puller (Sect. 2.5), suction may have to be substituted or combined with a short pulse (500–1,000 nA, 1 ms) using the "ZAP" function of the intracellular amplifier/software, if implemented. Depending on the respiratory neuron class (5), resting V_m and R_i in our studies on the neonatal rat in vitro models range from −35 to −60 mV and from 150 to 700 MΩ, respectively (7, 9, 24, 42, 46, 51–53, 59, 60, 70–72) (Fig. 4, 6, and 7). V_m values in our published studies tend to be lower than those in reports from other groups (10, 12, 25). This is partly

because we do not correct V_m for liquid-junction potentials with an estimated amplitude of 10–20 mV (49–51). We do not correct for these potentials because we did not find a significant change between resting V_m for different classes of (respiratory) neurons, regardless of whether the cells were recorded with high or low Cl^- solution (see above), which should theoretically change liquid-junction potential by at least 10 mV. Once V_m stabilizes within several minutes after establishing the whole-cell configuration, R_i is monitored via repetitive injection of hyperpolarizing DC current pulses (40–250 pA, 0.5–0.7 s) at intervals of 5–15 s (Fig. 6).

3.2.3. Electrical Stimulation

Electrical stimulation of neighboring neuronal areas or fiber tracts at regular intervals with either a single pulse or repetitive ("tetanic") pulse trains is a powerful tool for analyzing synaptic neuronal connectivity and roles of glial cells in neural network function. We have used this approach in a variety of respiratory and nonrespiratory slice and *en bloc* preparations (77–82). Findings using stimulation in the respiratory networks in the dish are referred to in the "Results" section (Sects. 4.1.1 and 4.2.4). Typical stimulation parameters using, for example, concentric bipolar stimulation electrodes (Sect. 2.5) are 5–90 V and 20–200 Hz for 0.02–10 s at single-pulse duration of 0.1–0.5 ms.

3.2.4. Gas- and Ion-Sensitive Microelectrodes

In several studies using the newborn rat *en bloc* model (37, 38, 83–85), we have applied microelectrodes that are sensitive to O_2, CO_2, H^+, K^+, or Ca^{2+} (86, 87). Contrary to our positive experience with other isolated mammalian tissues, such as astrocytes in guinea pig olfactory cortex slices (77), neurons in rat sympathetic ganglia (88), and expiratory neurons and neighboring glia in cats in vivo (89), intracellular recording does not seem to be feasible with ion-sensitive microelectrodes in isolated respiratory networks from perinatal rodents. Details regarding extracellular use of such electrodes by us are given in the above reports that focused on analyzing the extracellular microenvironment of newborn rat VRC neurons during spontaneous and evoked activity and on effects of oxygen and glucose depletion, that is "anoxia" and "aglycemia," respectively, and complete blockade of metabolism ("in vitro ischemia") (Sect. 4.1.1). Corresponding experiments were conducted in two of our studies on similarly anoxia-resistant dorsal vagal neurons in juvenile rat brainstem slices (Chap. 1-Trapp and Ballanyi (45); see also Chap. 12-De Curtis et al. (90)).

For recording dynamic changes of the above-mentioned gases or ions, the microelectrodes were positioned within the VRC in a tissue depth of 300–600 μm below the ventrolateral brainstem surface, corresponding to the main distribution within the transversal plane of newborn rat VRC neurons (5, 30, 37) (Figs. 1 and 2).

PO_2 in the recording chamber was continuously monitored with a "Clark-style" macroelectrode (Diamond Electro-Tech Inc.,

Ann Arbor, MI, USA), whereas tissue PO_2 was determined with O_2 microelectrodes obtained either from Diamond Electro-Tech (outer tip diameter, 20–30 μm) or as a gift from H. Baumgärtl (Max Planck Institut fur Systemphysiologie, Dortmund, Germany; outer tip diameter 5–15 μm). Procedures for constructing these electrodes and their properties are described elsewhere (87). The O_2-sensitive macroelectrode was calibrated in the recording chamber during superfusion with HEPES pH-buffered solution gassed with either 100% O_2 or air (21% O_2) and during superfusion with 159 mM of the O_2 chelator Na_2SO_3 for obtaining the 0 mmHg O_2 level ("anoxia"). Subsequent superfusion with standard superfusate resulted in a bath PO_2 value of ~700 mmHg in CO_2/HCO_3^- pH-buffered, carbogenated standard solution and a very similar value in HEPES pH-buffered saline gassed with 100% O_2. In hypoxic saline (95% N_2 plus 5% CO_2 or 100% N_2), PO_2 in the recording chamber ranged from 3 to 10 mmHg. Arrest of superfusate flow reduced the signals of the O_2-sensitive macro- and microelectrodes by 7–15%. This "stirring effect" may lead to underestimation of surface and tissue PO_2 because the electrode approaches the tissue surface and crosses a proposed "unstirred layer" (37, 85, 87).

Procedures for the production of ion-sensitive microelectrodes and their properties have been described elsewhere (37, 38, 80, 83–86). In brief, theta-style double-barreled borosilicate micropipettes are fabricated with a microelectrode puller (Sect. 2.5). A good tip size for extracellular recording is 1–5 μm because smaller tip diameters result in a reduced signal-to-noise ratio due to the high resistance (Sect. 2.2.2), while larger tip sizes may cause leakage of ion resin. K^+-sensitive microelectrodes are calibrated before and after experiments with solutions containing 1.5, 6, and 15 mM KCl and a constant background of 145 mM NaCl. The value for the slope for a tenfold change in the free K^+ concentration for these "valinomycin"-type K^+ electrodes is typically 56 mV. Ca^{2+}-sensitive microelectrodes are calibrated in standard solution with different (buffered) Ca^{2+} content and have a mean slope of 29 mV/tenfold change in Ca^{2+}. pH-sensitive microelectrodes are calibrated in solutions of different pH (Sect. 2.2.2) and have a mean slope of 58 mV/pH unit. Triple-barreled pH-sensitive microelectrodes have been used by us for simultaneous measurement of extracellular pH and partial pressure of tissue CO_2 in the VRC of the newborn rat *en bloc* model (85).

For gas- and ion-sensitive microelectrode measurements, it is important to determine the surface of the in vitro respiratory preparations. For ion-sensitive microelectrodes, touching the surface is reflected by a sudden perturbation of the voltage of the reference barrel. Lateral disposition during downward movement of O_2-sensitive electrodes is used to determine the point of entry into the tissue. Importantly, the reference barrel of ion-sensitive electrodes, which is filled with standard solution (Sect. 2.2.1), can be used to record extracellular respiratory neuronal activity (37).

3.3. Optical Recording

Both voltage- and Ca^{2+}-sensitive fluorescent dyes have been applied since ~10 years for monitoring the activity of populations of respiratory neurons in both *en bloc* and slice models. These studies by various groups including us are summarized in our recent review articles (15, 18, 23, 43). These articles also point out how we have adapted multiphoton microscopy for monitoring cellular morphology and activity based on rhythmic cytosolic Ca^{2+} rises (Sect. 3.3.2) (62) in preBötC neurons and neighboring glia with greatly improved spatial resolution compared to previous CCD camera imaging (e.g., in (11)) (Sect. 4.2.4). In the following, principles of such Ca^{2+} imaging are described after briefly referring to the methodology of voltage imaging using the newborn rat *en bloc* model based on our collaboration with the Onimaru group (24).

3.3.1. Voltage Imaging

In our voltage imaging study (23, 24), *en bloc* [+VII] preparations (Sect. 3.1.3) were immersed for 40–50 min in "Suzue-type" (4) solution with 50 μg/ml of the fluorescent voltage-sensitive dye Di-2-ANEPEQ. They were then placed ventral side up in an acrylic chamber that was mounted on an Olympus BX50WIF-2 fluorescence microscope (Sect. 2.8). After focusing the objective on the ventral brainstem surface, spontaneous activity in the VRC including both the preBötC and the pFRG was optically monitored as a change in Di-2-ANEPEQ fluorescence intensity with a MiCAM01 CCD camera (Sect. 2.8). Optical recording, triggered by electrophysiological cervical inspiratory-related burst activity, was done with an acquisition time of 20 ms per image resulting in a sampling rate of 50 Hz. The sampling period (6.8 s) included a time period of 1.7 s that preceded the steepest point of the cervical burst, which constituted the trigger threshold. Because of the extremely low signal-to-noise ratio associated with voltage imaging (15), 40–50 images and corresponding cervical bursts needed to be averaged and were digitally stored. Fluorescence changes were expressed as ratios of fluorescence intensity that were compared with a reference image.

Differential images were processed with a 3×3 pixel software-spatial filter (Sect. 2.8) and displayed in pseudocolor with red corresponding to a fluorescence decrease indicating depolarization. For representation of the time course of fluorescence changes, averaged fluorescence intensity was assessed and inverted in a 50-pixel region of interest covering an area of 92×108 μm. It should be noted that optical signals presumably reflect primarily depolarizations that are associated with respiratory drive potentials but may also include a glial component (15).

3.3.2. Multiphoton/ Confocal Ca^{2+} Imaging

Bursting in newborn rat VRC neurons is accompanied by Ca^{2+} influx through specific sets of voltage-activated Ca^{2+} channels (51, 52). Consequently, their activity can be visualized with optical imaging of changes in the free cytosolic $[Ca^{2+}]$ as established

since several decades for neurons in various brain regions, both in vitro and in vivo (43, 62, 65). For our multiphoton/confocal Ca^{2+} imaging approach in preBötC interneurons and XII motoneurons plus neighboring glia of calibrated brainstem slices, 0.5 mM Fluo-4-AM is backfilled into a broken patch pipette with an outer diameter of 5–10 µm (Sect. 2.8). The dye is then pressure-injected (25–50 mmHg) for 10 min (65) into the VRC/preBötC area or XII nucleus at 50 µm depth. This leads to staining of cells that are located between the surface and a depth of at least 100 µm, which is the resolution limit for our multiphoton system. While imaging, inspiratory-related neuronal population activity is monitored with a suction electrode from the contralateral VRC/preBötC (Sect. 2.5). Fluorescence signals are measured using either an Olympus FluoView-300 confocal laser scanning microscope (Fig. 3) or a custom-made multiphoton system using a further FluoView-300 system connected to a Ti:Sa IR laser (Sect. 2.8) Details of the extents of stained areas and the quality of cellular imaging are given below (Sect. 4.2.4). The Ca^{2+} dye-loaded areas are mostly monitored using a 20× objective with 2–3× digital zoom at reduced settings for y-axis scanning. Compared to full frame acquisition (512 × 512 pixels), such "clipped mode" imaging samples an area of 512 × 100–220 pixels and provides scanning rates of 1.25–1.43 Hz which are sufficient to detect 70–100% of the peak of inspiratory-related Ca^{2+} rises. The morphology of cell bodies and primary dendrites is best revealed by combining "z-stack" image series (single z-steps 0.1–0.5 µm) with 3D animation using FluoView software (Sect. 2.8). Fluo-4 or Fluo-8L fluorescence emission is weak at low cytosolic Ca^{2+} levels (62, 65). Therefore, to improve morphological characterization of cells, slices are exposed at the end of experiments to glutamate (0.25–1 mM, 5–10 min) for generation of z-stacks. Glutamate-induced fluorescence signals are 3–10 times larger than those associated with spontaneous Ca^{2+} rises or Ca^{2+} increases evoked by other neuromodulators such as substance-P.

Another method of loading cells in preBötC slices with Ca^{2+} dye is via injection into the midline (11). We do not use that approach because retrograde transport of the dye from the injection spot to the preBötC takes several hours compared to 10 min for direct injection into the preBötC or 30 min for incubation of slices with Ca^{2+} dye. For the latter procedure, a preBötC slice is kept for 30 min at 30°C in carbogenated standard superfusate containing 10 µM Fluo-8L-AM (Sect. 2.8). In our hands, bath application of Fluo-8L-AM (or Fluo-4-AM) primarily loads small cells, likely astrocytic glia, whereas others find that a sufficient number of (respiratory active) neurons are loaded as well (for references, see (15, 23)) (Sect. 4.2.4).

3.3.3. Morphological Characterization of preBötC Cells in Calibrated Slices

We outlined above (Sect. 2.9) how whole-cell recorded neonatal rodent respiratory neurons can be histologically identified using lucifer yellow or neurobiotin/biocytin in the patch electrode. While this approach is performed on chemically fixed and subsequently sectioned *en bloc* or slice preparations, we recently developed a method for acutely labeling XII motoneurons and (primarily) neurons in the preBötC area of living slices that were incubated with sulforhodamine-101 (Sect. 2.9). Note that this technique likely cannot be used to differentially label neurons versus glial cells in the brainstem slices contrary to the feasibility of this approach in newborn rat hippocampal or neocortical slices (Chap. 11-Kantor et al. (57)).

3.4. Data Analysis

Inspiratory-related neuronal population activity in preBötC slices in 3K/1Ca solution is continuously recorded at a sampling rate of 1–4 kHz. Burst rate is averaged every 20 min over 2-min time windows. The "longevity" of rhythm in 3 mM K^+ solution is defined as the time from start of recording until the time when a burst is not followed by a further burst within a time period of 10 min. Single-burst duration is defined using ClampFit software (Molecular Devices Corporation, Chicago, Il, USA) as the time interval from when the signal increases above and decreases below a threshold set at 10% of the peak amplitude for that burst. Pharmacologically reactivated rhythms are described by averaging burst rates over a 2-min time period at steady state. Values are means ± SEM except for histological analyses (means ± SD). Significance ($P < 0.05$) is assessed by Student's t-test or one-way ANOVA using SigmaPlot (Systat Software Inc., Point Richmond, Ca, USA) or Prism (GraphPad Software Inc., La Jolla, CA, USA; www.graphpad.com).

For analysis of Ca^{2+}-imaging experiments, firstly, FluoView software is used for drawing regions of interests (ROIs) around cell somata to obtain plots of fluorescence intensity over time (Sect. 2.8). Fluorescence intensity analysis data are then transferred to Excel of the Microsoft Office suite for further computation and plotting of graphs. 3D reconstruction is obtained from z-stack series (Sect. 2.8). As typical 3D settings, we use an x-y plane with rotation in x and y axes to give a 3D impression of cell morphology and x-z plane with y axis rotation to reveal the depth of fluorescence signal. For generating figures for publication, fluorescence intensities are plotted in graphs using both Excel and Illustrator (Adobe; www.adobe.com).

4. Results

Here, we summarize our findings using the (calibrated) in vitro respiratory models. Reference to work by other groups can be found in the reference lists of our original papers and review articles that are primarily referred to in the following.

4.1. Findings on Noncalibrated En Bloc Preparations and preBötC Slices

Our previous studies using the "classical" Suzue-type (*en bloc* [+VII]) brainstem–spinal cord preparation (Sect. 3.1.3) and preBötC slices from newborn rats aimed primarily at analyzing the extracellular microenvironment of VRC neurons (only in the *en bloc* model) and elucidating intrinsic biophysical membrane properties of VRC neurons and their response to (endogenous) neuromodulators. This work, which has been reviewed in detail in several articles (5, 46, 72), is summarized in the following.

4.1.1. Microenvironment of VRC Neurons in the En Bloc Model

One major aspect of our research is devoted to the analysis of cellular mechanisms of the extreme tolerance to anoxia of neural respiratory networks in newborn mammals as established by previous in vivo work (for citations, see (5, 46, 72)). For this, we blocked aerobic metabolism either by exposing the preparations to hypoxic superfusate or chemically via bath application of cyanide (1 mM). Our measurements with O_2-sensitive microelectrodes revealed that hypoxic superfusate causes anoxia within the VRC, whereas tissue PO_2 increases to almost superfusate levels in response to cyanide (37, 38, 83). Contrary, our ion-sensitive microelectrode and whole-cell V_m recordings revealed very similar responses to both approaches for blocking aerobic metabolism. Specifically, extracellular pH shows (often after a <2-min period of alkalinization) a progressive acidosis that can exceed >0.3 pH units at the end of a >10 min anoxia period (37, 38, 84, 85). Within <3 min into anoxia, extracellular K^+ rises by <2 mM and remains stable at this level for at least 30 min, whereas extracellular Ca^{2+} does not change during this time period (37, 38, 83, 84). In ~30% of cases, inspiratory-related cervical bursting accelerates by up to 100% during the initial 1–2 min of anoxia. Rhythm transiently stops during this period in other ~30% of preparations, while bursting is not affected in the remaining cases. After >3 min into anoxia, inspiratory rhythm slows down progressively. At the end of a 30 min anoxia period, in vitro inspiratory burst rate typically falls about tenfold, from 5–10 bursts/min in control to <0.5 bursts/min. This is very similar to slowed, but persisting breathing in newborn mammals in vivo at reduced temperature (for references, see (5, 46, 72)).

Slowing of in vitro inspiratory rhythm in response to hypoxic or chemical anoxia is accompanied by a persistent hyperpolarization in >50% of inspiratory VRC neurons, a major portion of which becomes "functionally inactivated" (70). There is pharmacological evidence that ATP-sensitive K^+ channels are involved in this anoxic hyperpolarization and thus possibly contribute to slowing of rhythm, which may be an adaptive mechanism for reduction of energy consumption (5, 46, 70, 72, 84). Arrest of metabolism, by combined exposure to cyanide and the glycolytic inhibitor iodoacetate, blocks inspiratory rhythm irreversibly within <5 min after start of application. Such in vitro apnea is followed within several minutes by a rise of extracellular K^+ of >10 mM that is mirrored

by a fall of extracellular Ca^{2+} by >0.5 mM (84). Perturbation of extracellular ions and pH within the VRC in response to in vitro ischemia is accompanied by irreversible depolarization of VRC neurons (5). All this showed that sustained anoxia does not cause a major disruption of ionic homeostasis in the VRC contrary to its rapid deregulation in response to metabolic arrest. This indicates that stimulation of anaerobic metabolism during anoxia ("Pasteur effect") is able to maintain basic cellular functions in newborn rat brainstems (5, 80, 84).

Our above studies also revealed that the >2-mm-thick *en bloc* preparation has an anoxic core in carbogenated standard solution (37, 38, 83, 84). The same reports also indicated that cells in depths of 300–800 µm below the ventral surface including spontaneously active neurons within the most densely aggregated area of the VRC in the transversal area 300–600 µm (Figs. 1 and 2) are normoxic and that cells in depths <300 µm are even hyperoxic. The tissue PO_2 gradient in the ventrolateral aspect of isolated brainstems is reflected by gradients for PCO_2 and pH which is ~0.5 pH units more acidic in the anoxic core compared to the surface. This pronounced extracellular acidosis in control solution is likely the consequence of enhanced anaerobic metabolism in the anoxic core leading to lactate formation and associated H^+ production (37, 38, 83, 84). Along the VRC column in the transversal plane, there is also a gradient for extracellular K^+, which increases from ~4 mM in 300 µm depth to ~5.5 mM in 600 µm depth (37). Contrary, extracellular Ca^{2+} is stable throughout the *en bloc* preparation at 1.5 mM corresponding to the superfusate Ca^{2+} content used as standard at that time (84).

Upon tetanic electrical stimulation (Sects. 2.5 and 3.2.3) in control solution, PO_2 in the VRC decreases by up to 50 mmHg with a concomitant increase of both extracellular K^+ and pH by maximally 5 mM and 0.07 pH units, respectively (37, 38). We did not measure extracellular Ca^{2+} during tetanic stimulation but found that it remains unaltered during spontaneous inspiratory activity, which does also not affect extracellular pH (37, 38, 84). Contrary, extracellular K^+ in the VRC increases during each inspiratory burst by up to 100 µM, while PO_2 falls by maximally 0.4 mmHg (37).

In the *en bloc* model, use of O_2-, CO_2-, and H^+-sensitive microelectrodes enabled us to study central chemosensitivity which means adaptation of breathing to altered PCO_2 levels by brainstem sites that are intrinsically sensitive to the resulting change of medullary pH (26, 27, 85) (see also Chap. 13-Day and Wilson (91)). We found that the pH gradient in the VRC is reflected by a PCO_2 gradient with a value of 77 mmHg in 300 µm depth versus 95 mmHg at 600 µm. Despite the fact that both pH (see above) and PCO_2 in the VRC differ notably from in vivo values (see also Chap. 13-Day and Wilson (91)), the *en bloc* model is capable of responding to experimentally evoked changes of either parameter.

We also showed that acidosis counters the depression of inspiratory rhythm by opioids (5). Our findings from such experiments indicate that extracellular H^+ is the primary stimulatory factor in central chemosensitivity which may often mask a less evident direct effect of CO_2 (85). In addition, the latter work and our further studies using these electrodes (38, 48) provided evidence that respiratory chemosensitive structures are either located several hundred micrometers within the tissue, and not close to the ventral surface as has been proposed, and/or that chemosensitive structures close to the surface do respond with a delay of several minutes (for references, see (5, 26, 46, 48, 85)).

From these findings, we hypothesized that (1) VRC neurons in the newborn rat *en bloc* model are under aerobic conditions which is reflected by baselines of extracellular K^+ and Ca^{2+} that are close to physiological levels (36, 39), (2) anoxic slowing of inspiratory-related rhythm in newborn mammals represents an adaptive mechanism for energy conservation and seems to involve hyperpolarization of VRC neurons via ATP-sensitive K^+ channels, (3) tolerance to anoxia of respiratory networks in neonatal mammals may be due to their capability to enhance their utilization of anaerobic glycolysis, and (4) preBötC slices of <1,000 μm thickness should not have an anoxic core, at least under our superfusion conditions (Sects. 2.4 and 3.1).

4.1.2. Properties of Newborn Rat VRC Neurons

In various studies using whole-cell recording in both the *en bloc* and preBötC slice models, we established that resting V_m and R_i (Sect. 3.2.2) range between −35 to −60 mV and 150–750 MΩ, respectively, depending on the specific class of VRC neurons (Figs. 4, 6, and 7). In the en bloc model, these cell classes comprise several types each of pre-/postinspiratory active pFRG, inspiratory, and "tonic" expiratory neurons (5, 6, 24).

Using primarily the *en bloc* [+VII] model (Sect. 3.1.3), we elucidated the following intrinsic biophysical membrane properties of newborn rat VRC neurons: (1) Following initial identification of the type of VRC neurons and subsequent blockade of their rhythmic activity by the voltage-activated Na^+ channel blocker tetrodotoxin, use of specific (snail peptide) blockers revealed that these cells are equipped with distinct sets of L-, T-, N-, R-, and P/Q-type voltage-activated Ca^{2+} channels (51). Our follow-up study on analyzing the functional relevance of voltage-activated Ca^{2+} channels (52) unraveled that blockade of a single type of such Ca^{2+} channels (or Ca^{2+}-activated K^+ channels) does not block inspiratory rhythm despite specific cellular effects on individual VRC neurons. (2) As stated above (Sect. 4.1.1), ATP-sensitive K^+ channels seem to be involved in persistent postsynaptic hyperpolarization of VRC neurons during anoxia (5, 46, 70, 72). B-type γ-aminobutyric acid ($GABA_B$) receptors are coupled in a subpopulation of these neurons to postsynaptic K^+ channels whose activation by the $GABA_B$ receptor

agonist baclofen leads to sustained hyperpolarization, whereas there is no evidence for endogenous activation of these channels during in vitro inspiratory rhythm (59). (3) The latter study provided evidence that $GABA_A$ and glycine receptor-coupled anion channels hyperpolarize VRC neurons rhythmically during different phases of the in vitro respiratory cycle (Fig. 4), contrary to depolarizing actions of these major inhibitory neurotransmitters on neonatal hippocampal and cortical neurons (46, 48, 75) (see also Chap. 11-Kantor et al. (57)). (4) Hyperexcitability of spinal inspiratory motoneurons and some VRC interneurons in response to the $GABA_A$ receptor antagonist bicuculline (60) is depressed by adenosine acting on A_1 receptors, although neither adenosine nor A_1 receptor agonists have a major postsynaptic effect on these cells in control solution. However, adenosine acts through A_1 receptors to depress nonrespiratory activity and stabilize irregular inspiratory rhythms, while there is no evidence for functional A_2 receptors in newborn rat VRC neurons (60). (5) Agents raising cellular cyclic adenosine monophosphate (cAMP) such as forskolin or isobutylmethylxanthine reverse depression of both cellular bursting in VRC neurons and inspiratory cervical motor output by either prostaglandins or agonists of μ-type opioid receptors. Depending on the inspiratory VRC neuron type, the latter agents can cause either a postsynaptic hyperpolarization or presynaptic inhibition (71) (Sect. 4.2.3). (6) Using preBötC slices (in 8–9-mM K^+), we found that tonic excitation of XII motoneurons is mediated by postsynaptic 5-HT_2-type serotonin receptors (53). The same study also revealed that the latter receptors are also activated in preBötC neurons during excitatory serotonin effects on inspiratory rhythm, whereas other serotonin effects are mediated by 5-HT_{1A} receptors (53).

4.2. Findings on Calibrated En Bloc Preparations and preBötC Slices

Here, we summarize our recent findings on calibrated in vitro models from newborn rats and mice (Sect. 3.1). Specifically, we refer to (1) the structure–function analysis of the dual respiratory center via anatomical and pharmacological dissection, (2) influence of superfusate composition on isolated preBötC, (3) cellular mechanisms of preBötC depression by opioids and anoxia, and (4) "pharmoptic" approaches for preBötC neuron–glia discrimination.

4.2.1. Structure–Function Analysis of the Dual Respiratory Center

Studies using the *en bloc* [+VII] model (Sect. 3.1.3) established that the preBötC and pFRG constitute a dual inspiratory-expiratory center, at least in newborns (2, 5, 6, 8, 26) (Sect. 1). Both components of this dual center can be isolated by transecting this model. Onimaru's group found 5 years ago that a rostral brainstem "slab," generated by transection of the *en bloc* model 0.1–0.2 mm caudal to VII_c, shows rhythmic VII nerve activity presumably representing cranial pFRG motor output (6, 92). The caudal boundary of this rhythmic pFRG block neighbors the rostral boundary of ~350-μm-thick preBötC slices that we developed in our milestone

study on the discovery of the inspiratory center about two decades ago (7). In the latter study, we estimated based on consecutive sectioning that the newborn rat preBötC extends ~200 µm in rostrocaudal direction. Specifically, the brainstem aspect of the *en bloc* model was sectioned in either rostral-to-caudal or caudal-to-rostral direction until cervical or cranial inspiratory motor output, respectively, was irreversibly blocked. Since then, numerous studies make use of preBötC slices, however, with notable differences between laboratories in regard to their thickness (200–1,100 µm) and anatomical margins that were not determined histologically (for references, see (18, 33)).

We dealt with the latter issues by developing online histology for generating calibrated preBötC slices with anatomically defined and reproducible boundaries (33) (Sect. 3.1.2). In a follow-up study (40), we used "m-preBötC" slices with centered preBötC (Sect. 3.1.2) to determine the minimal thickness that is sufficient for inspiratory-related rhythm in "physiological" 3K/1Ca solution (Sect. 3.1) (Figs. 1 and 2). Specifically, we found that the center of the newborn rat preBötC is located exactly 0.5 mm caudal to VII_c and that the minimal slice thickness for synchronous bursting in the ipsilateral and contralateral preBötC area is 200 µm. In that study, we also developed 700-µm-thick "r+preBötC" and "c+preBötC slices" that contain the exposed (and partially sectioned) preBötC plus either rostrally or caudally adjacent brainstem tissue, respectively (Sect. 3.1.2) (Fig. 2). Using the latter slice types, we firstly found that <100 µm preBötC tissue is necessary for rhythm generation in 3K/1Ca if rostrally or caudally neighboring brainstem areas are present to provide (tonic) excitatory drive to rhythmogenic neurons. Secondly, we demonstrated that the preBötC has a "spatio-chemical organization." Specifically, in 3K/1Ca, c+preBötC slices generate regular fast inspiratory-related "fictive eupnea" bursts. Contrary, r+preBötC slices show a sequence of fictive eupnea bursts that are interrupted by occurrence of a single, larger amplitude "fictive sigh" which is often followed by transient post-sigh depression of one or several subsequent fictive eupnea bursts.

We also showed that upon onset of in vitro apnea after several hours of recording in 3K/1Ca (33, 40), bath application of various neuromodulators can restore rhythm with a fictive eupnea burst pattern (Fig. 2). These agents are thyrotropin-releasing hormone (0.1–100 nM), the cAMP-dependent phosphodiesterase-4 blocker rolipram (1–5 µM), the methylxanthine theophylline (0.25–10 mM), the group I metabotropic glutamate receptor agonist 3,5-dihydroxyphenylglycine (at 1–10 µM), and also 9 mM K^+ (15, 18, 33, 40). Contrary, substance-P (or the agonist GR73632 for neurokinin-1 receptors that are normally activated by substance-P), 3,5-dihydroxyphenylglycine (at 10–50 µM), and also 6–8-mM K^+ induce mostly a mixed fictive eupnea-sigh burst pattern. These different patterns

of suction electrode-recorded inspiratory population activity were reflected by corresponding patterns of small (eupnea-like) and large (sigh-like) cytosolic Ca^{2+} rises in preBötC neurons (Sect. 4.2.4) (Fig. 7). The latter observations indicate that structures rostral to the preBötC are capable of inducing sighs in preBötC networks which can reconfigure between different burst patterns under the influence of particular neuromodulators.

Our latter published findings substantiate hypothesis that the preBötC comprises a very thin kernel of likely only several hundred rhythmogenic inspiratory neurons (2, 7). However, our most recent data indicate that the preBötC, nevertheless, represents a small distributed neural network as proposed previously based on both in vivo and in vitro findings (for references, see (18)). Specifically, we isolated two neighboring inspiratory active 700-µm-thick slices from a single newborn rat brainstem (18). This is achieved by slicing firstly at 1.2 mm caudal to VII_c, then at 0.5 mm caudal to VII_c, and finally 0.2 mm rostral to VII_c (Sect. 3.1.1). The caudal one of these "sandwich" preBötC slices shows rhythmic activity with ~1-s single burst duration in both ventrolateral aspects of the rostral margin. In the rostral slice, recording from the ventrolateral area of the caudal margin reveals similar bursting but at lower rate (i.e., <3 vs. >5 bursts/min). Moreover, the bursts in the rostral slice with a single-burst duration of ~1 s are often partly obscured by an even slower rhythm with a single-burst duration of several seconds. The short-burst rhythms in both aspects of the sandwich slices seem, indeed, to represent inspiratory-related bursting because they are blocked by the µ-opioid receptor agonist [D-Ala^2,N-Me-Phe^4,Gly^5-ol]-enkephalin (DAMGO) [compare Fig. 7]. Contrary, slow bursting in the rostral slice is either not affected, or even stimulated, by DAMGO and may thus be generated by pFRG networks. In fact, findings from various in vivo and in vitro studies revealed that the preBötC is inhibited by opioids, whereas the pFRG is resistant, thus substantiating the >20-year-old hypothesis by the group of Onimaru and Homma on a dual respiratory center (for references, see (2, 5, 6)).

Recently, we showed using the *en bloc* [+VII] model that cyanide-evoked chemical anoxia is a further pharmacological tool, in addition to opioids, for elucidating the structure–function relationship between the preBötC and the pFRG (24). Specifically, we found, using combined suction electrode and whole-cell recording, that opioids increase the delay between the onsets of preinspiratory pFRG and inspiratory preBötC bursting. Contrary, we showed in that study (24) that synchronization of both rhythm generators by anoxia seems to result in generation of repetitive cervical bursts and enhanced postinspiratory activity (Figs. 8 and 9). These electrophysiological changes were reflected by optical (neuronal) population signals obtained by voltage imaging from three different brainstem regions containing the preBötC, the area of the BötC in adults, and the caudal aspect of the pFRG (Fig. 8). All this

indicates that similarly severe frequency depression of preBötC network bursting by opioids and anoxia (Fig. 7) is due to fundamentally different cellular mechanisms that are referred to below in more detail (Fig. 9) (Sect. 4.2.3). In a related study (28), we found that the change of respiratory burst patterns in the brainstem aspect of the *en bloc* [+VII] model upon anoxia revealed by voltage imaging is reflected by a similar transformation of pre-/postinspiratory into inspiratory/postinspiratory bursting in pFRG-driven lumbar nerves. That study (28) reported further that such pre-/postinspiratory lumbar bursting in control solution, and also repetitive cervical nerve bursts during evoked anoxia, is blocked following transection of the *en bloc* [+VII] preparation ~0.2 mm caudal to VII_c. In a related report (34), we identified landmarks on the ventral brainstem surface that enable generation of the *en bloc* model with an anatomically defined rostral section level (Sect. 3.1.3). We used this approach to demonstrate that the critical level, at which brainstem transection abolishes pFRG-mediated lumbar nerve bursting, is located close to the rostral end of VII nucleus as also indicated by findings of Giraudin and colleagues (29). In our latter study (34), we also reported that inspiratory XII nerve bursting disappears spontaneously in the *en bloc* [+VII] model within ~30 min after start of recording in control solution, whereas such activity is stable for several hours in *en bloc* [–VII] preparations.

In summary, we showed on the one hand that both preBötC-driven inspiratory and pFRG-driven expiratory activities in calibrated newborn rat brainstem models depend greatly on both their physical dimensions and the relative location of the preBötC and pFRG within the preparation depending on transection levels. On the other hand, we added experimentally evoked anoxia as a further tool besides opioids for pharmacological dissection of these networks.

4.2.2. Influence of Superfusate Composition on Isolated preBötC

In this section, we outline that superfusate K^+, Ca^{2+}, and glucose greatly influence preBötC (slice) rhythms. We point out that (close to) physiological superfusate concentrations of these constituents do not provide long-term in vitro inspiratory rhythm while, depending on the slice type, it is beneficial to use, at least, values that are as close as possible to physiological levels.

Superfusate K^+: In our paper on the preBötC discovery (7), we noted that "slices >500 µm thick generate rhythmic motor output with a cycle frequency that was 40 to 70% of that in the *en bloc* brainstem-spinal cord before the slice was cut. This frequency could be increased by changing the K^+ concentration in the slice bathing solution from 3 to 9 mM *[…]*. Thinner slices did not generate motor output at 3 mM K^+ but generated rhythmic output at K^+ concentrations of 9–11 mM." These statements indicated, on the one hand, a modulatory effect on preBötC networks of superfusate K^+, which does not fully equilibrate with extracellular K^+ in *en bloc* preparations (Sect. 4.1.1), but most likely in slices of <1 mm

thickness. This established the view that preBötC slices are principally only active in superfusate with a higher than physiological K^+ level, which is 3 mM (33, 34, 36, 39, 48). Specifically, it was argued that the ("tonic") excitatory drive from neighboring neurons for (intrinsic) bursting of rhythmogenic neurons is too low in preBötC slices and that elevated K^+ depolarizes these neurons and thus compensates for that attenuated drive (2). As a result, most groups use 8 or 9 mM K^+ even when studying thick preBötC slices despite the fact that such K^+ levels are an established in vitro epilepsy model using cortical brain slices (for references, see (18, 33, 34) and Chap. 11-Kantor et al. (57)).

Our initial study (33) showed that calibrated preBötC slices of ≥500 μm thickness (Sect. 3.1) are capable of inspiratory rhythm in 3K/1Ca for several hours (Fig. 2). Our recent unpublished observations indicate that raising K^+ from 3 to 9 mM does not principally change rhythmic Ca^{2+} rises in preBötC neurons except that a few more cells may become active in the same ventrolateral slice region while the rate of their inspiratory Ca^{2+} oscillations increases modestly (Fig. 10). This indicates that preBötC bursting in slices in elevated K^+ differs from seizure-like K^+-evoked hyperexcitability in cortical brain slices (see above). Our group also demonstrated that bursting in the preBötC area of slices is also not perturbed by blockers of $GABA_A$ and glycine receptors, such as bicuculline and strychnine, respectively, which are further common epilepsy models for cortical brain slices (for references, see (18, 33, 34) and Chap. 11-Kantor et al. (57)). Contrary, the latter agents cause large-amplitude seizure-like rhythmic bursting in XII motoneurons of slices and in spinal motoneurons of the *en bloc* model (18, 59, 60).

Despite the fact that preBötC slices are principally functional in physiological K^+, elevated superfusate K^+ is needed if long-term (>2 h) recording is intended in <500-μm-thick preBötC slices that are used to minimize modulation of rhythmogenic inspiratory networks by rostrocaudally neighboring brainstem tissue (40, 42) (Sect. 4.2.1). Above (Sect. 2.2), we stated that a convenient strategy may be to perform such experiments initially in 5K/1Ca solution and gradually increase K^+ in steps of 1 mM once rhythm starts to slow down. Ultimately, in 7K/1Ca solution, preBötC-driven rhythms in the ventrolateral slice area and concomitant activities XII nerve and/or nucleus are stable for >6 h at a rate of 5–15 bursts/min (42). Although this is slightly slower compared to bursting in 9 mM K^+ in 1 mM Ca^{2+}, it is still fast enough for pharmacological and patch-clamp analyses (42, 44). For Ca^{2+} imaging, such burst rates in 7K/1Ca are even advantageous because recovery of inspiratory-related Ca^{2+} rises takes sometimes >5 s, at least in our hands using either Fluo-4 or Fluo-8L (Fig. 10). Thus, preBötC rhythm at >15 bursts/min would probably interfere with Ca^{2+} recovery (Sect. 4.2.4) (15, 24, 33, 40, 43).

While elevated K^+ is needed for long-term rhythm in slices, this manipulation affects the sensitivity of the preBötC to some neuromodulators. For example, we showed that DAMGO abolishes preBötC slice rhythm in 3K/1Ca at 10–25 nM (33). Our recent findings indicate that this blockade is reversed by increasing K^+ to 9 mM in the presence of such low DAMGO doses (Fig. 7) and that DAMGO needs to be elevated to almost micromolar concentrations to depress rhythm again in 9K/1Ca (see Fig. 11 in (18)). Similarly, pronounced slowing of preBötC slice rhythm by chemical anoxia is antagonized by raising K^+ from 3 to 9 mM in 1 mM Ca^{2+} (Fig. 7) (see also Fig. 11 in (18)). Moreover, we found that V_m oscillations in inspiratory preBötC neurons are much affected by superfusate K^+. In 3K/1Ca, a large population of inspiratory neurons show a ramp-like depolarization before the onset of the inspiratory (synaptic) drive potential and concomitant action potential discharge (Fig. 7). This "inspiratory burst" is often followed by a pronounced hyperpolarization that turns into a progressive preinspiratory depolarization (Fig. 7). Raising K^+ only modestly depolarizes resting V_m which becomes rather "flat" between inspiratory bursts (Fig. 7) (see also Fig. 12 in (18)).

Superfusate Ca^{2+}: Measurements with Ca^{2+}-sensitive microelectrodes in various brain regions in vivo indicated a most common physiological extracellular value of 1.1–1.2 mM for this cation (for references, see (18, 33, 34, 36, 39)). Despite this, most in vitro respiratory studies use superfusate Ca^{2+} levels that vary, mostly between 1.5 and 2.4 mM, and sometimes as low as 0.8 mM (for references, see (4, 10, 18, 25, 33, 34)). Recently, we investigated whether extracellular Ca^{2+} influences preBötC networks (34). Specifically, we found that robust rhythm of calibrated newborn rat preBötC slices in 3K/1Ca is strongly depressed by raising Ca^{2+} to 1.5 mM and that this depression is countered by increasing also K^+ to at least 7 mM (Fig. 6). This substantiates the hypothesis that inspiratory network activity is determined by a "Ca^{2+}/K^+ antagonism." This term has been introduced several decades ago by Leusen based on in vivo findings by his group using injection of both these ions into respiratory brainstem areas (for references, see (18, 33, 34)). We showed further in this study (34) that Ca^{2+} elevation from 1 to 1.5 mM also strongly depresses preBötC bursting in the newborn rat *en bloc* [–VII] model with rostrally exposed preBötC. Contrary, we found in the same study (34) that >1.5 mM Ca^{2+} is necessary to depress inspiratory rhythm in 3 K in *en bloc* preparations with more brainstem tissue rostral to the preBötC (Fig. 6) likely because K^+ is ~2 mM higher in the VRC area (Sect. 4.1.1). Our unpublished findings indicate that slice rhythms are slightly more robust and faster in 3 mM K^+ and 0.75 mM Ca^{2+}. In some preparations, however, seizure-like activity develops in inspiratory motor networks at 0.75 mM Ca^{2+}, and such hyperexcitability becomes more pronounced when Ca^{2+} is lowered further. In a recent study (42), we presented evidence that blockade

of bursting in the isolated preBötC by raised Ca^{2+} is due to presynaptic inhibition. This view is based on an apparent lack of a postsynaptic effect of high Ca^{2+} on V_m or R_i in inspiratory preBötC neurons and neighboring tonically active neurons that may provide excitatory drive to the rhythmogenic inspiratory cells (Fig. 6). In summary, our latter findings indicate that superfusate Ca^{2+} levels above physiological values inhibit the preBötC and thus necessitate the use of 8–9 mM K^+ to counter this inhibition. At close-to-physiological Ca^{2+} levels of 1–1.2 mM, rhythm in (thick) slices occurs in 3 K for time periods of up to several hours and can be maintained for many hours after raising K^+ to maximally 7 mM.

Glucose: Extracellular brain glucose levels appear to range between 0.1 and 1 mM, depending somehow on the type of analytical tool and/or the brain region tested (for references see Chap. 1-Trapp and Ballanyi (45)). Contrary, 30 mM glucose was used in control solution in all our published studies on the *en bloc* model and non-calibrated preBötC slices and also in the vast majority, if not all, of studies by other groups using these models, for example, (4, 10–12, 22, 25, 29, 30, 32). In our published work on calibrated preBötC slices, 20 mM glucose was sufficient for robust rhythm over time periods of at least 8 h (in raised K^+). As indicated by our yet unpublished findings, in vitro inspiratory activity depends notably on superfusate glucose content. Specifically, we showed that (1) preBötC slices generated at 18–20°C in superfusate with 30 mM glucose show a slower rhythm (<5 bursts/min) that stops earlier in 3K/1Ca compared to slices generated under the same conditions and using the same solution except that glucose was 5 mM; (2) in 7K/1Ca, preBötC slices of up to 700 µm thickness generate stable rhythm in the ventrolateral aspect for >5 h in 1 mM glucose, but inspiratory XII activity seems to be more robust in 5–10 mM; and (3) for sustained viability of the *en bloc* model, superfusate glucose needs to be at least 20 mM while 30 mM are typically used. This is based on both our recent unpublished data and our previous findings on the *en bloc* model (84). Specifically, the latter study showed that 10 mM glucose is not sufficient for long-term inspiratory rhythm and that the typically highly anoxia-tolerant preparations (Sect. 4.1.1) respond with irreversible blockade of rhythm and major perturbation of ion homeostasis to anoxia in 10 mM glucose, particularly when preparations were obtained from P2-3 compared to P0-1 rats.

4.2.3. Cellular Mechanisms of preBötC Depression by Opioids and Anoxia

The above findings (Sect. 4.2.1) indicate that opioids and anoxia are powerful pharmacological tools for dissecting the individual components of the dual respiratory center. Currently, we study cellular mechanisms by which opioids depress preBötC networks and the clinically used methylxanthines caffeine and theophylline counter this depression. Our preliminary data indicate that opioids primarily inhibit preBötC neurons via presynaptic mechanisms,

similar to inhibitory effects of high Ca^{2+} (Sect. 4.2.2) (Fig. 6), and that also methylxanthines exert their respirogenic action mainly at presynaptic sites (18, 42, 93). Our recent studies show that methylxanthines need to be applied at low millimolar doses for reversing in vitro inspiratory depression by opioids (44, 93). Based on the necessity for using such high doses of caffeine and theophylline, we hypothesized that the stimulatory action of caffeine and theophylline on inspiratory rhythms is due to blockade of cAMP-degrading phosphodiesterase-4 in rhythmogenic preBötC neurons (44) to which cAMP is presumably a major stimulus (5, 18, 31, 33, 44, 46, 71). Our related preliminary results indicate that low millimolar methylxanthine doses, applied in control solution, cause seizure-like hyperexcitability in spinal inspiratory motor networks (93) (Fig. 5). This is in line with the established clinical epileptogenic side effect of these agents (for references, see (44)).

Our recent study using the *en bloc* [+VII] model indicated that, similar to opioids, also anoxia does not hyperpolarize a major number of identified preBötC neurons (24). This contrasts with our previous work on the uncalibrated *en bloc* model and our recent unpublished data on calibrated preBötC slices, indicating that ~50% of inspiratory (preBötC) neurons are persistently hyperpolarized by anoxia with a notable concomitant fall of R_i as indication of a metabolically induced increase in K^+ conductance (5, 46, 70, 72). The above discrepancy in anoxia response may partly stem from the use of different models, that is, uncalibrated versus calibrated *en bloc* or *en bloc* versus slice. Contrary, comparison between anoxia and opioid responses points to a different cellular mechanism of a seemingly very similar frequency depression of inspiratory motor output by anoxia and opioids. This hypothesis is supported by our published findings based on voltage imaging in the *en bloc* model (Sect. 4.2.1) (Figs. 8 and 9) ((24) and unpublished Ca^{2+} imaging data obtained in the preBötC of calibrated slices). The latter findings show that DAMGO-evoked depression of preBötC inspiratory-related neuronal activity is accompanied by a fall of cytosolic Ca^{2+} in these neurons while Ca^{2+} in adjacent presumptive astrocytes does not change. Contrary, depression of preBötC neuronal bursting by anoxia is accompanied by a notable Ca^{2+} rise in inspiratory neurons and a concomitant, often more pronounced, Ca^{2+} increase in neighboring glia (see Fig. 4 in (15)).

4.2.4. Pharmoptic Approaches for preBötC Neuron–Glia Discrimination

In a recent "Perspective" article, we noted that glial cells may contribute to control of inspiratory preBötC neuron networks, similar to their recently established important roles in other behaviors (27). However, our published imaging data do not provide straightforward criteria for discrimination of glial from neuronal responses. For example, our voltage imaging study revealed different reconfiguring preBötC/pFRG activities in the *en bloc* [+VII] model in response to opioids and anoxia (24) (Figs. 8 and 9).

Importantly, current CCD camera-based voltage imaging in the in vitro respiratory models has principally a temporal resolution in the millisecond range, whereas spatial resolution is rather limited (15, 23, 24, 43). Consequently, voltage imaging data, as shown in Fig. 8, represent, on the one hand, the merged activity of inspiratory, pre-/postinspiratory, and tonic expiratory neurons (5). On the other hand, these presumably neuronal signals may be "contaminated" by responses from glial cells (15).

Compared to voltage imaging, the kinetics of (recovery from) respiratory-related Ca^{2+} rises are in the range of 1–5 s. This is, at least partly, due to buffering and binding properties of the currently available fluorescent dyes (15, 23, 62). This disadvantage is outweighed by spatial resolution at the (sub)cellular level (see below). Focal injection of Fluo-4-AM, as our preferred method of loading cells in the preBötC of calibrated slices with fluorescent Ca^{2+} dye (15, 23, 33, 40, 43, 94) (Sects. 2.8 and 3.3.2), loads both neurons and glia. Contrary, bath application of Fluo-4-AM or Fluo-8L-AM seems to primarily load glia in our hands. Consequently, our injection approach does not discriminate between preBötC neurons and glial cells unless additional techniques are applied, such as patch-clamp recording from at least one cell during population imaging, or imaging combined with genetic fluorescent protein marking of identified neuron or glial populations (15–17, 43). In the following, we present our preliminary data on combined pharmacologic and optic ("pharmoptic") approaches to discriminate neurons from glia. Also, in this section, we summarize some of our recent Ca^{2+} imaging data in preBötC slices, in extension to those regarding effects of anoxia and opioids outlined at the end of the previous section.

Our group was the first to adapt multiphoton/confocal microscopy techniques (62, 65) to respiratory network analysis in mammals. In a series of papers, (15, 18, 23, 33, 40, 43, 94), we unraveled both the activity and morphology of inspiratory active, histologically identified preBötC neurons in calibrated newborn rat brainstem slices (Sect. 3.3.2). Within <20 min upon focal injection of Fluo-4-AM into the preBötC or XII nucleus, typically 5–15 cells in a given focal imaging plane show inspiratory-related Ca^{2+} rises in a circular area of 150–300 μm diameter (15, 94) (Fig. 10). Presumptive inspiratory preBötC neurons in transversal newborn rat slices can be visualized into tissue depths of up to 80–100 μm (15, 33, 40). Thus, 50–100 active Fluo-4-labeled preBötC cells can theoretically be studied in a total of 4–5 imaging planes in each preBötC aspect or XII nucleus using our custom-made multiphoton system (Sect. 2.8). However, for optimal spatial resolution, corresponding imaging with our confocal or custom-made multiphoton systems (Fig. 3) is restricted to imaging planes of maximally 50–60 μm below the slice surface (Sect. 2.8). Either imaging system provides greatly increased spatial resolution compared to

previous CCD camera-based imaging (11). This is particularly evident when 3D animations are made based on z-stack imaging series in slices exposed to glutamate (Sect. 3.3.2) (see figures in (15, 18, 23, 33, 40, 43, 94)). Our multiphoton imaging data indicate that presumptive inspiratory preBötC neurons have a soma diameter of ~12–25 μm and 2 to >5 primary dendrites, whereas astrocytic glial cells appear mostly round and seem to have soma diameters of <10 μm with no indication of successful labeling of their normally widespread but very fine processes (Figs. 10 and 11). Our published Ca^{2+} imaging studies were done in r+preBötC slices from cells located within the caudal 50 μm of the caudal preBötC margin. Our preliminary data (94) indicate that inspiratory active neurons in the most rostral preBötC aspect of c+preBötC slices are less abundant and more sparsely distributed in the transversal plane (Fig. 10). It is unlikely that fewer cells take up Fluo-4-AM in the rostral preBötC aspect because bath application of glutamate (0.1–1 mM) reveals a prominent Ca^{2+} rise in many cells with neuron-like morphology in both the rostral and caudal preBötC aspect (Fig. 10) (see also Fig. 4 in (15, 94)).

As a finding of major importance for understanding preBötC properties, we demonstrated that individual presumptive inspiratory neurons visualized with multiphoton/confocal Ca^{2+} imaging are capable in 3K/1Ca of reconfiguring their activity pattern between a fictive eupnea and a mixed eupnea-sigh burst pattern (see Fig. 7 in (40)) (Sect. 4.2.1). Specifically, after onset of in vitro apnea in 3K/1Ca, we used mostly thyrotropin-releasing hormone (0.1–100 nM), the phosphodiesterase-4 blocker rolipram (1–5 μM), or 7–9 mM K^+ (Fig. 7) to evoke regular eupnea-like Ca^{2+} rises in preBötC neurons, whereas we applied the neurokinin-1 receptor agonist GR73632 to evoke a eupnea-sigh burst pattern (15, 18, 33, 40) (Sect. 4.2.1). More recently, we have found that phenylephrine (5–50 μM) promotes a prominent Ca^{2+} increase in neurons corresponding to fictive sigh signals in control solution (see Fig. 4 in (15)). However, stimulation of the amplitude of inspiratory bursts by phenylephrine is not accompanied by a major rise of Ca^{2+} baseline in active preBötC neurons, whereas presumptive glial cells respond often with a major Ca^{2+} increase. A modest rise of Ca^{2+} baseline is also typical for neurons in response to GR73632 while this agent has a minor, if at all, effect on presumptive glia. Moreover, thyrotropin-releasing hormone does not evoke a major Ca^{2+} rise in any preBötC cell type (see Fig. 4 in (15)).

Another of our recent studies (61) used our Ca^{2+} imaging approach to complement a wide range of other data from the group of Dr. G. D. Funk (Edmonton) for elucidating a potential contribution of preBötC glia to stimulation of inspiratory slice rhythm by adenosine triphosphate (ATP). Specifically, we found in that collaboration (61) that ATP evokes a Ca^{2+} rise in the preBötC area primarily in cells with a soma diameter of <10 μm, whereas Ca^{2+}

was not notably changed in larger rhythmically active neighboring cells, likely representing neurons. Prior to this study, we observed that further pharmacological agents besides chemical anoxia and phenylephrine evoke a less prominent Ca^{2+} rise in presumptive inspiratory active neurons versus astrocytes that are noninspiratory active, at least regarding cytosolic Ca^{2+} signaling. Specifically, the endoplasmic reticulum Ca^{2+} ATPase inhibitor cyclopiazonic acid and the metabotropic glutamate receptor agonist 1-aminocyclopentane-1,3-dicarboxylic acid (t-ACPD) apparently evoke a notably more prominent Ca^{2+} rise in glia (Fig. 11), which occurs often in an oscillatory pattern in the case of t-ACPD.

We have currently developed a further assay for highlighting glial cells in newborn rat brainstem slices. Specifically, bath application of Fluo-4-AM or Fluo-8L-AM can be combined with (or followed by) bath application of Cd^{2+} (Fig. 11). Cd^{2+} seems to enter brainstem glial cells more easily than neurons, in particular during the first 10 min of exposure, and subsequently interacts with Fluo to increase fluorescence intensity. Prelabeling with Fluo-4 or Fluo-8L can be used, for example, to target glial cells for patch-clamp recording in preBötC slices (11). We currently use the novel glial "Fluo-Cd^{2+} staining" approach after pharmacological analysis in preBötC slices to highlight the 3D organization of astrocyte networks. In addition, by using the fluorescent cell marker sulforhodamine-101, we can label XII motoneurons (in red) while using the combined Fluo-Cd^{2+} approach for labeling neighboring presumptive astrocytes (in green) (Fig. 11). Our most recent findings indicate that we can label newborn rat astrocytes in hippocampal and cortical slices after electrophysiological experiments with a green fluorescent antibody against glial fibrillary acidic protein (Chap. 11-Kantor et al. (57)). We have just started to use this approach to identify, after the electrophysiological imaging experiments, astrocytes in the preBötC and XII nucleus of calibrated slices.

Recently, we have started to use tetanic electrical stimulation (Sect. 3.2.3) in the calibrated slices for identifying properties of preBötC neurons and glia. Preliminary findings indicate that stimulation in the preBötC (or XII) area in slices loaded with Fluo-4 or Fluo-8L via bath application evokes a wave of Ca^{2+} rises in small cells. This Ca^{2+} wave spreads in all directions to a distance of sometimes >200 μm from the starting point of the signal at the electrode tip (Fig. 12). Similar tetanic stimulation of the preBötC following loading of both glia and neurons via injection of dye reveals that also (inspiratory active) neurons respond with a notable Ca^{2+} rise.

By combining electrical stimulation with suction electrode recording, we demonstrated that evoked activity in one preBötC aspect can depress activity in the ipsilateral preBötC aspect (Fig. 12). Moreover, we found that stimulation in the midline of the slice

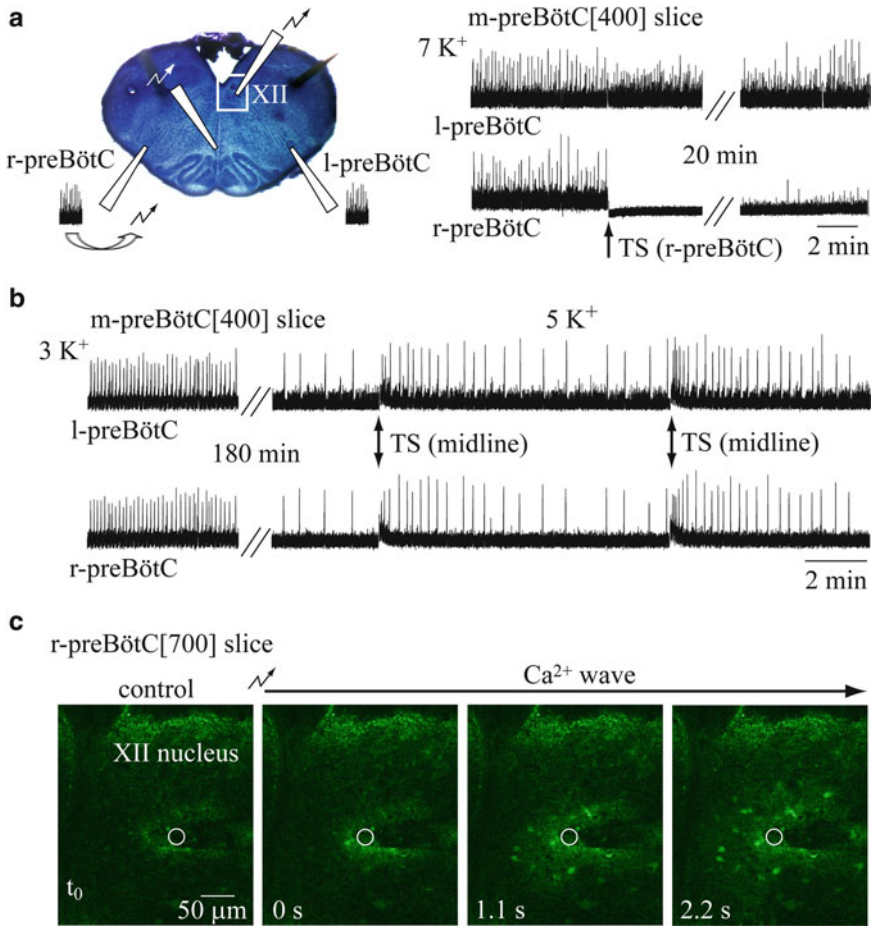


Fig. 12. Effects of electrical stimulation on inspiratory rhythm and glial Ca^{2+} in calibrated newborn rat preBötC slices. (**a**) In an m-preBötC[400/–0.75]W-P2 slice kept in 7 mM K^+ application of repetitive electrical pulses (50 V, 100 Hz, 100 pulses with 100-µs single-pulse duration) via the suction electrode in the *right* (“r”), preBötC aspect (see schema) caused long-term blockade of inspiratory rhythm in this region, whereas bursting in contralateral (*left*, “l”) preBötC was notably less perturbed. (**b**) In an m-preBötC[400/–0.80]W-P1 slice, initially robust inspiratory rhythm in 3 K^+ stopped after 90 min. Raising K^+ to 5 mM reactivated inspiratory bursting in both preBötC aspect. Tetanic electrical stimulation (60 V, 100 Hz, 100 pulses with 250-µs single-pulse duration) in the slice midline (see schema in **a**) accelerated rhythm in both preBötC aspects. (**c**) In the XII nucleus (see schema in **a**) of a 700-µm-thick caudal “sandwich preBötC slice” (see Sect. 4.2.1) loaded via incubation with Fluo-4 local tetanic stimulation (70 V, 100 Hz, 100 pulses with 250-µs single-pulse duration) evoked a wave of cytosolic Ca_i rises in presumptive astrocytes that progressed at a speed of ~25 µm/s.

between both preBötC aspects can activate bouts of inspiratory rhythm in 5K/1Ca solution which, by itself, is not sufficient to restore rhythm after onset of in vitro apnea in 3K/1Ca (Fig. 12). These preliminary findings indicate that electrical stimulation is a new powerful tool for identifying neuron–glia interactions within the preBötC as we have demonstrated successfully for neural circuits in cerebellar slices (82).

5. Limitations

Our studies summarized above and numerous reports from other laboratories have established that both newborn rodent brainstem–spinal cord preparations and preBötC slices are highly potent in vitro models for studying respiratory control. Examples for outstanding results are the discovery of the preBötC and the pFRG and the fact that both these rhythmogenic neural networks remain active in a transversal slice and after transection of the *en bloc* model slightly caudal to VII_c, respectively (Sect. 4.2.1). The functional relevance of the preBötC and the pFRG and also the hypothesis that they comprise a dual respiratory center (Sect. 4.2.1) have been substantiated by in vivo findings that used a wide spectrum of preparations ranging from fetal rodents to adult mammals of various species (2, 5, 16, 19, 26, 47). For that research, opioids turned out as one important tool for pharmacological dissection of preBötC- and pFRG-driven activities, both in the *en bloc* model and in vivo (Sect. 4.2.1). In fact, a large number of neuromodulators and experimental approaches, such as evoked anoxia, have very similar effects on dual respiratory center activities in that model as in vivo (5, 46, 72). Despite these advantages, both types of respiratory networks in the dish have limitations as pointed out in the following.

5.1. Limitations of the En Bloc Model

Despite the above-described ultimately important findings, it has been argued that in vitro respiratory activity in the *en bloc* model does not correspond to eupnea-like breathing but rather represents (anoxia-related) gasping (95). However, in recent review articles, we summarized findings from our group and others showing that respiratory-related rhythms in the newborn rat *en bloc* model are very similar to in vivo activity in deafferented newborn rats in vivo at reduced temperature (5, 46, 72). Although our studies revealed an anoxic core in this preparation, this core does not seem to influence the respiratory networks that are located in more superficial layers where (respiratory) neurons operate in this model under aerobic (and even hyperoxic) conditions for cells close to the ventral surface (Sect. 4.1.1) (5, 37, 46, 72, 83). We note in the latter articles that the fact that respiratory networks in the *en bloc* model respond to experimentally evoked anoxia like intact newborn mammals indicates that these structures are not hypoxic or anoxic in control solution. This view is supported by the findings from our group and others summarized in our above review articles (5, 46, 72) that inspiratory rhythms in the *en bloc* model are not affected by removal via sectioning of the dorsal brainstem aspect which very likely eliminates the anoxic core. As long as superfusate glucose content is at least 20 mM (Sect. 2.2), anaerobic

metabolism appears to be sufficient for maintaining cellular/axonal functions even in the anoxic core for several hours.

Inspiratory-related (cervical) spinal motor output persists in all types of calibrated *en bloc* models for >8 h (Sect. 3.2.1), whereas cranial inspiratory activity seems to deteriorate over time. Specifically, XII bursting disappears in *en bloc* [+VII] preparations within <1 h of recording according to our published study (34). Similarly, respiratory VII or trigeminal nerve bursting seems to stop during that time period based on our unpublished observations. Arrest of inspiratory XII bursting is likely not related to the anoxic core because evoked chemical anoxia of the entire preparation can restore such bursting. In addition, XII bursting is not abolished in *en bloc* [–VII] preparations during evoked anoxia as indicated by our preliminary findings. In our hands, also pre-/postinspiratory activity in lumbar and VII nerve roots disappears after 15–60 min in >50% of complete brainstem–spinal cord preparations, whereas such activity is typically stable for several hours in other laboratories, for example, that of Dr. Onimaru. At least in newborn mice, a further limitation of using the *en bloc* model with a major portion of tissue attached is related to the fact that the pons in this species exerts a tonic depressing action on the preBötC (96).

5.2. Limitations of Calibrated preBötC Slices

Our finding that preBötC slices are capable of rhythm in 3K/1Ca led to various important discoveries: (1) spatio-chemical organization of rhythmogenic inspiratory networks (Sect. 4.2.1) (40), (2) Ca^{2+}/K^{+} antagonism of bursting of (isolated) preBötC networks (34), (3) high sensitivity to some neuromodulators that is in various cases greatly attenuated by commonly used high K^{+} solutions, for example, during inspiratory depression by opioids and anoxia (18, 33). While we found that supraphysiological superfusate Ca^{2+} levels depress bursting of the isolated preBötC, use of 1 mM superfusate Ca^{2+} is not sufficient for countering occurrence of in vitro apnea in 3 mM K^{+} that occurs within <2 h in 400-µm-thin slices and within ~4 h in 700-µm-thick slices (33, 34, 40). While we found that use of close-to-physiological superfusate glucose concentrations (1–5 mM) during generation of preBötC slices results in more robust slice rhythm in 3K/1Ca, this does not delay onset of in vitro apnea. Consequently, particularly <700-µm-thick slices need to be studied in elevated K^{+} (7 mM) with glucose levels between 1 and 20 mM, and we recommend to start recording in 5K/1Ca (Sects. 2.2 and 4.2.2).

5.3. Limitations Common to En Bloc and Slice Models

One major limitation of both *en bloc* or slice models is the restriction of the time window of their use to the perinatal period, specifically to ~1 week old in rats for both models and to ~2 weeks for slices in mice, at least in some strains (Sect. 2.1). One major reason for this restriction may be related to the fact that the minimal neural substrate capable of respiratory rhythm likely expands

rostrocaudally during the early postnatal time period. Consequently, thicker transversal preBötC slices would have to be generated, if older animals are intended to be used. These thicker slices from older animals would have a larger anoxic core that may result in inactivation and/or damage of preBötC (and pFRG) neurons. Similar to other neural structures, respiratory groups seem to lose, during the first postnatal week, their extreme tolerance to depletion of oxygen (O_2) that is evident at birth (5, 46, 72, 83). As discussed above (Sect. 4.1.1) an anoxic core is already present in the newborn rodent *en bloc* model (37, 83). However, this core does not seem to include essential cellular elements of the dual respiratory center except for apparently anoxia-tolerant axons that connect both bilaterally organized VRC aspects (Sects. 4.1.1 and 5.1). The anoxic core would extend notably after the first postnatal week in parallel with an increase in brainstem size. To avoid this limitation while preserving some of the advantages of an in vitro approach, respiratory networks can be studied in older animals in an internally perfused brainstem model that is also applicable to newborn rodents (for references, see (46, 48) and Chap. 13-Day and Wilson (91)).

As a further restriction, *en bloc* preparations in general and preBötC slices in 3K/1Ca need to be studied at a temperature that is ~10°C lower than in vivo (Sect. 3.1.4). This results in slowing of respiratory-related bursting and may also distort some (synaptic) interactions within the respiratory networks and possibly affect their responses to some neuromodulators as well. Our unpublished observations indicate that the robustness of inspiratory-related rhythm in 3K/1Ca is more pronounced in preBötC slices from Wistar versus Sprague-Dawley rats and that onset of in vitro *apnea* also varies between litters from the same rat strain. This indicates that properties of the isolated preBötC differ between rodent species and also depend on factors such as nutrition or stress which may even differ between litters in a given species and strain. Another limitation of either model is related to the fact that slices with partially exposed preBötC in close-to-physiological 3K/1Ca solution differ in their inspiratory-related burst patterns, depending on whether the preBötC is neighbored by rostral or caudal tissue (Sect. 4.2.1) (40). Modulation by adjacent brainstem tissue may also affect the pFRG upon isolation in a slice, but this has not been studied yet. The latter considerations indicate that it may be advantageous to keep the rostrocaudal microenvironment of the preBötC (or pFRG) kernel intact, as is the case in the *en bloc* [+VII] model. While analysis of neuronal properties in both networks is possible using blind whole-cell recording techniques (Sect. 4.1.2), imaging at cellular resolution has yet been reported only for respiratory neurons located <100 μm below the (slice) surface based on previously used (custom-made) multiphoton microscopes (Sect. 4.2.4) (15, 33, 40). The latest generation of such microscopes is presumably

capable of dynamic (Ca^{2+}) imaging deeper within living brainstem tissues, both in slices and in the *en bloc* model, but this still needs to be demonstrated. Alternatively, "GRIN" lenses or micro-optrodes may be used which combine microelectrode penetration of tissue with the capability for cellular imaging (for references, see (15, 23, 43, 62)).

A further obstacle for "respiratory imaging" (15) is the reduced capability for long-term analysis of in vitro respiratory networks which is mostly related to the toxicity of this approach. For voltage imaging, most of the currently used dyes seem to depress respiratory network activity, and extended time periods of imaging are required because of the necessity for averaging (62), normally for ~50 cycles with the system we used (Sects. 2.8, 3.3.1, and 4.2.4) (15, 23, 24). Regarding our currently used multiphoton system, continuous Ca^{2+} imaging at a sampling rate of ~1 frame/s is limited to 1–2 h. Beyond that time period at that sampling rate or after correspondingly shorter time for higher scanning rates, both neurons and glial cells show a progressive increase in resting fluorescence intensity along with decreased resolution of morphological details. The cells stop showing spontaneous Ca^{2+} rises (in the case of neurons) or responses to experimental manipulations. On average, the total time for Ca^{2+} imaging in healthy cells using the confocal system seems to be slightly shorter than for the multiphoton imaging system. It needs to be considered that multiphoton imaging may reduce some phototoxicity because only cells in the focal plane are excited by the potentially harmful excitation laser light. However, the necessity for using an IR laser for this imaging approach comes at the expense of a potential caloric cell damage, particularly in more superficial tissue layers (15, 23, 24, 43, 62). Possibly, these problems will be solved, or at least improved, by the new generation of voltage and multiphoton imaging systems and/or other (genetically-engineered) dyes.

6. Perspective

Despite these limitations, the isolated calibrated respiratory networks from perinatal rodents will certainly provide further results of ultimate importance for understanding the neural control of breathing. We conclude with resounding a hypothetical scenario from our review article on "respiratory imaging" (15) that would likely answer, with advanced imaging techniques, most relevant questions in neural control of breathing: "Subpopulations of respiratory interneurons and output cells will be identified via specific patterns of expressed fluorescent proteins and acutely fluorescence-tagged ion channels, receptors and/or transporters. Populations of these identified cells will then be loaded with cell-permeant fluorescent

dyes for, e.g., simultaneous imaging of dynamic changes of signaling factors such as Ca^{2+} or pH in the cytosol and/or subcellular compartments. Subsequently, one or a few of these cells will be whole-cell recorded with additional functional or morphological dyes in the patch electrode solution for a correlation analysis of dynamic changes of subcellular activities with respiratory-related membrane potential oscillations or underlying membrane currents. Further improvement of computerized data processing and the spatiotemporal resolution of fluorescence microscopy will enable simultaneous 4-dimensional imaging of all these events for a thorough structure-function relationship of respiratory centers and motor circuits."

Acknowledgments

Work contributing to this study was supported by the Alberta Heritage Foundation for Medical Research (AHFMR), Alberta Innovates Health Solutions-Hotchkiss Brain Institute (AIHS-HBI), the Canada Foundation for Innovation (CFI-ASRIP), and operating plus training grants from the Canadian Institutes of Health Research (CIHR).

References

1. Bianchi AL, Denavit-Saubié M, Champagnat J (1995) Central control of breathing in mammals: neuronal circuitry, membrane properties, and neurotransmitters. Physiol Rev 75:1–45
2. Feldman JL, Del Negro CA (2006) Looking for inspiration: new perspectives on respiratory rhythm. Nat Rev Neurosci 7:232–242
3. Smith JC, Abdala AP, Rybak IA, Paton JF (2009) Structural and functional architecture of respiratory networks in the mammalian brainstem. Philos Trans R Soc Lond B Biol Sci 364:2577–2587
4. Suzue T (1984) Respiratory rhythm generation in the *in vitro* brain stem-spinal cord preparation of the neonatal rat. J Physiol 354:173–183
5. Ballanyi K, Onimaru H, Homma I (1999) Respiratory network function in the isolated brainstem-spinal cord of newborn rats. Prog Neurobiol 59:583–634
6. Ballanyi K, Onimaru H (2009) Respiratory network analysis, isolated respiratory center functions. In: Binder M, Hirokawa N, Windhorst U (eds) Encyclopedia of neuroscience. Springer, Heidelberg/New York/Tokyo, pp 3453–3458
7. Smith JC, Ellenberger HH, Ballanyi K, Richter DW, Feldman JL (1991) Pre-Bötzinger complex: a brainstem region that may generate respiratory rhythm in mammals. Science 254:726–729
8. Molkov YI, Abdala AP, Bacak BJ, Smith JC, Paton JF, Rybak IA (2010) Late-expiratory activity: emergence and interactions with the respiratory CpG. J Neurophysiol 104: 2713–2729
9. Smith JC, Ballanyi K, Richter DW (1992) Whole-cell patch-clamp recordings from respiratory neurons in neonatal rat brainstem *in vitro*. Neurosci Lett 134:153–156
10. Rekling JC, Champagnat J, Denavit-Saubi M (1996) Electroresponsive properties and membrane potential trajectories of three types of inspiratory neurons in the newborn mouse brain stem in vitro. J Neurophysiol 75:795–810
11. Koshiya N, Smith JC (1999) Neuronal pacemaker for breathing visualized *in vitro*. Nature 400:360–363
12. Del Negro CA, Morgado-Valle C, Feldman JL (2002) Respiratory rhythm: an emergent network property? Neuron 34:821–830

13. Ramirez JM, Viemari JC (2005) Determinants of inspiratory activity. Respir Physiol Neurobiol 147:145–157
14. Doi A, Ramirez JM (2008) Neuromodulation and the orchestration of the respiratory rhythm. Respir Physiol Neurobiol 164:96–104
15. Ruangkittisakul A, Okada Y, Oku Y, Koshiya N, Ballanyi K (2009) Fluorescence imaging of active respiratory networks. Respir Physiol Neurobiol 168:26–38
16. Gaultier C, Gallego J (2008) Neural control of breathing: insights from genetic mouse models. J Appl Physiol 104:1522–1530
17. Gray PA (2008) Transcription factors and the genetic organization of brain stem respiratory neurons. J Appl Physiol 104:1513–1521
18. Ballanyi K, Ruangkittisakul A (2009) Structure-function analysis of rhythmogenic inspiratory pre-Botzinger complex networks in "calibrated" newborn rat brainstem slices. Respir Physiol Neurobiol 168:158–178
19. Champagnat J, Morin-Surun MP, Bouvier J, Thoby-Brisson M, Fortin G (2011) Prenatal development of central rhythm generation. Respir Physiol Neurobiol 178:146–155
20. Iizuka M (2001) Respiratory activity in glossopharyngeal, vagus and accessory nerves and pharyngeal constrictors in newborn rat in vitro. J Physiol 532:535–548
21. Iizuka M (2004) Rostrocaudal distribution of spinal respiratory motor activity in an in vitro neonatal rat preparation. Neurosci Res 50:263–269
22. Iizuka M (2011) Respiration-related control of abdominal motoneurons. Respir Physiol Neurobiol 179(1):80–88
23. Ballanyi K, Onimaru H, Keller B (2009) Respiratory network analysis, functional imaging. In: Binder M, Hirokawa N, Windhorst U (eds) Encyclopedia of neuroscience. Springer, Heidelberg/New York/Tokyo, pp 3447–3453
24. Ballanyi K, Ruangkittisakul A, Onimaru H (2009) Opioids prolong and anoxia shortens delay between onset of pre-inspiratory (pFRG) and inspiratory (preBötC) network bursting in newborn rat brainstems. Eur J Physiol (Pflügers Archiv) 458:571–587
25. Onimaru H, Homma I (2003) A novel functional neuron group for respiratory rhythm generation in the ventral medulla. J Neurosci 23:1478–1486
26. Guyenet PG, Mulkey DK (2010) Retrotrapezoid nucleus and parafacial respiratory group. Respir Physiol Neurobiol 173:244–255
27. Ballanyi K, Panaitescu B, Ruangkittisakul A (2010) Control of breathing by nerve glue. Sci Signal 3:pe41
28. Taccola G, Secchia L, Ballanyi K (2007) Anoxic augmentation of lumbar respiratory bursts and block of lumbar locomotion in newborn rat brainstem-spinal cord. J Physiol 585:507–524
29. Giraudin A, Cabirol-Pol MJ, Simmers J, Morin D (2008) Intercostal and abdominal respiratory motoneurons in the neonatal rat spinal cord: spatiotemporal organization and responses to limb afferent stimulation. J Neurophysiol 99:2626–2640
30. Smith JC, Greer JJ, Liu GS, Feldman JL (1990) Neural mechanisms generating respiratory pattern in mammalian brain stem-spinal cord in vitro. I. Spatiotemporal patterns of motor and medullary neuron activity. J Neurophysiol 64:1149–1169
31. Mironov SL, Langohr K, Richter DW (1999) A_1 adenosine receptors modulate respiratory activity of the neonatal mouse via the cAMP-mediated signaling pathway. J Neurophysiol 81:247–255
32. Tryba AK, Ramirez JM (2004) Hyperthermia modulates respiratory pacemaker bursting properties. J Neurophysiol 92:2844–2852
33. Ruangkittisakul A, Schwarzacher SW, Secchia L, Poon BY, Ma Y, Funk GD, Ballanyi K (2006) High sensitivity to neuromodulator-activated signaling pathways at physiological $[K^+]$ of confocally imaged respiratory center neurons in on-line-calibrated newborn rat brainstem slices. J Neurosci 26:11870–11880
34. Ruangkittisakul A, Secchia L, Bornes TD, Palathinkal DM, Ballanyi K (2007) Dependence on extracellular Ca^{2+}/K^+ antagonism of inspiratory centre rhythms in slices and *en bloc* preparations of newborn rat brainstem. J Physiol 584:489–508
35. Ballanyi K, Ruangkittisakul A (2009) Brain slices. In: Binder M, Hirokawa N, Windhorst U (eds) Encyclopedia of neuroscience. Springer, Heidelberg/New York/Tokyo, pp 483–490
36. Hansen AJ (1985) Effect of anoxia on ion distribution in the brain. Physiol Rev 65:101–148
37. Brockhaus J, Ballanyi K, Smith JC, Richter DW (1993) Microenvironment of respiratory neurons in the in vitro brainstem-spinal cord of neonatal rats. J Physiol 462:421–445
38. Völker A, Ballanyi K, Richter DW (1995) Anoxic disturbance of the isolated respiratory network of neonatal rats. Exp Brain Res 103:9–19
39. Somjen GG (2002) Ion regulation in the brain: implications for pathophysiology. Neuroscientist 8:254–267
40. Ruangkittisakul A, Schwarzacher SW, Secchia L, Ma Y, Bobocea N, Poon BY, Funk GD, Ballanyi K (2008) Generation of eupnea and sighs by a spatiochemically organized inspiratory network. J Neurosci 28:2447–2458

41. Ruangkittisakul A, Panaitescu B, Ballanyi K (2011) K^+ and Ca^{2+} dependence of inspiratory-related rhythm in novel "calibrated" mouse brainstem slices. Respir Physiol Neurobiol 175:37–48
42. Panaitescu B, Ruangkittisakul A, Ballanyi K (2009) Silencing by raised extracellular Ca^{2+} of pre-Bötzinger complex neurons in newborn rat brainstem slices without change of membrane potential or input resistance. Neurosci Lett 456:25–29
43. Ruangkittisakul A, Ballanyi K (2009) Neuron-glia-imaging. In: Binder M, Hirokawa N, Windhorst U (eds) Encyclopedia of neuroscience. Springer, Heidelberg/New York/Tokyo, pp 2756–2764
44. Ruangkittisakul A, Ballanyi K (2010) Methylxanthine reversal of opioid-evoked inspiratory depression via phosphodiesterase-4 blockade. Respir Physiol Neurobiol 172:94–105
45. Trapp S, Ballanyi K (2012) Autonomic nervous system in vitro: studying tonically active neurons controlling vagal outflow in rodent brainstem slices. In Isolated Central Nervous System Circuits (Ed K Ballanyi), Neuromethods Series Vol. 73 (Ed W Walz). Springer Science+Business Media, LLC, New York, NY, pp 1–59
46. Ballanyi K (2004) Neuromodulation of the perinatal respiratory network. Curr Neuropharmacol 2:221–243
47. Greer JJ, Funk GD, Ballanyi K (2006) Preparing for the first breath: prenatal maturation of respiratory neural control. J Physiol 570:437–444
48. Ballanyi K (1999) Isolated tissues: in vitro preparations. In: Windhorst U, Johansson H (eds) Modern techniques in neuroscience research. Springer, Heidelberg, pp 307–326
49. Neher E, Sakmann B (2009) Single-channel recording, 2nd edn. Springer, New York/Dordrecht/Heidelberg/London
50. Walz W (2007) Patch-clamp analysis: advanced techniques, 2nd edn. Humana, Totowa
51. Onimaru H, Ballanyi K, Richter DW (1996) Calcium-dependent responses in neurons of the isolated respiratory network of newborn rats. J Physiol 491:677–695
52. Onimaru H, Ballanyi K, Homma I (2003) Contribution of Ca^{2+}-dependent conductances to membrane potential fluctuations of medullary respiratory neurons of newborn rats *in vitro*. J Physiol 552:727–741
53. Schwarzacher S, Pestean A, Günther S, Ballanyi K (2002) Serotonergic modulation of respiratory motoneurons and interneurons in brainstem slices of perinatal rats. Neuroscience 115:1247–1259
54. Moore AR, Zhou WL, Jakovcevski I, Zecevic N, Antic SD (2012) Physiological properties of human fetal cortex in vitro. In Isolated Central Nervous System Circuits (Ed K Ballanyi), Neuromethods Series Vol. 73 (Ed W Walz). Springer Science+Business Media, LLC, New York, NY, pp 125–158
55. Sanchez-Vives MV (2012) Spontaneous rhythmic activity in the adult cerebral cortex in vitro. In Isolated Central Nervous System Circuits (Ed K Ballanyi), Neuromethods Series Vol. 73 (Ed W Walz). Springer Science+Business Media, LLC, New York, NY, pp 263–284
56. Broicher T, Speckmann EJ (2012) Living human brain slices: network analysis using voltage sensitive dyes. In Isolated Central Nervous System Circuits (Ed K Ballanyi), Neuromethods Series Vol. 73 (Ed W Walz). Springer Science+Business Media, LLC, New York, NY, pp 285–300
57. Kantor C, Panaitescu B, Kuribayashi J, Ruangkittisakul A, Jovanovic I, Leung V, Lee TF, MacTavish D, Jhamandas JH, Cheung PY, Ballanyi K (2012) Spontaneous neural network oscillations in hippocampus, cortex and *locus coeruleus* of newborn rat and piglet brain slices. In Isolated Central Nervous System Circuits (Ed K Ballanyi), Neuromethods Series Vol. 73 (Ed W Walz). Springer Science+Business Media, LLC, New York, NY, pp 315–356
58. Biggs JE, Lu VB, Kim H, Lai A, Todd KG, Ballanyi K, Colmers WF, Smith PA (2012) Defined medium organotypic cultures of spinal cord put 'pain in a dish'. In Isolated Central Nervous System Circuits (Ed K Ballanyi), Neuromethods Series Vol. 73 (Ed W Walz). Springer Science+Business Media, LLC, New York, NY, pp 405–435
59. Brockhaus J, Ballanyi K (1998) Synaptic inhibition in the isolated respiratory network of neonatal rats. Eur J Neurosci 10:3823–3839
60. Brockhaus J, Ballanyi K (2000) Anticonvulsant adenosine A_1 receptor-mediated adenosine action on neuronal networks in the brainstem-spinal cord of newborn rats. Neuroscience 96:359–371
61. Huxtable AG, Zwicker JD, Alvares TS, Ruangkittisakul A, Fang X, Hahn LB, Posse de Chaves E, Baker GB, Ballanyi K, Funk GD (2010) Glia contribute to the purinergic modulation of inspiratory rhythm generating networks. J Neurosci 30:3947–3958
62. Yuste R, Konnerth A, Masters B (2006) Imaging in neuroscience and development, a laboratory manual. J Biomed Opt 11:19902
63. Fish KN, Gonzales-Burgos G, Zaitsev AV, Lewis DA (2012) Histological characterization of physiologically determined fast spiking interneurons in slices of the primate dorsolateral prefrontal cortex. In Isolated Central Nervous System Circuits (Ed K Ballanyi), Neuromethods

Series Vol. 73 (Ed W Walz). Springer Science+Business Media, LLC, New York, NY, pp 159–181

64. Nakamura TJ, Michel S, Block GD, Colwell CS (2012) Neural circuits underlying circadian oscillations in mammals: clocks in a dish. In Isolated Central Nervous System Circuits (Ed K Ballanyi), Neuromethods Series Vol. 73 (Ed W Walz). Springer Science+Business Media, LLC, New York, NY, pp 183–210
65. Stosiek C, Garaschuk O, Holthoff K, Konnerth A (2003) *In vivo* two-photon calcium imaging of neuronal networks. Proc Natl Acad Sci USA 100:7319–7324
66. Paxinos G, Halliday G, Watson C, Koutcherov Y, Wang H (2007) Atlas of the developing mouse brain. Elsevier, Amsterdam/Boston/Heidelberg
67. Greene EC (1935) The anatomy of the rat. Braintree Scientific, Philadelphia
68. Cho YR, Pawela CP, Li R, Kao D, Schulte ML, Runquist ML, Yan JG, Matloub HS, Jaradeh SS, Hudetz AG, Hyde JS (2007) Refining the sensory and motor ratunculus of the rat upper extremity using fMRI and direct nerve stimulation. Magn Reson Med 58:901–909
69. Mandadi S, Nakanishi ST, Han P, Humphreys J, Whela PJ (2012) The use of rodent isolated spinal cord preparations to examine motor output. In Isolated Central Nervous System Circuits (Ed K Ballanyi), Neuromethods Series Vol. 73 (Ed W Walz). Springer Science+Business Media, LLC, New York, NY, pp 437–464
70. Ballanyi K, Völker A, Richter DW (1994) Anoxia induced functional inactivation of neonatal respiratory neurons *in vitro*. Neuroreport 6:165–168
71. Ballanyi K, Lalley PM, Hoch B, Richter DW (1997) cAMP dependent reversal of opioid and prostaglandin mediated depression of the isolated respiratory network in newborn rats. J Physiol 504:127–134
72. Ballanyi K (2004) Protective role of neuronal K_{ATP} channels in brain hypoxia. J Exp Biol 207:3201–3212
73. Stachniak TS, Sudbury JR, Trudel E, Choe KY, Ciura S, Bourque CW (2012) Osmoregulatory circuits in slices and *en bloc* preparations of rodent hypothalamus. In Isolated Central Nervous System Circuits (Ed K Ballanyi), Neuromethods Series Vol. 73 (Ed W Walz). Springer Science+Business Media, LLC, New York, NY, pp 211–231
74. Trapp S, Lückermann M, Brooks PS, Ballanyi K (1996) Acidosis of dorsal vagal neurons in situ during spontaneous and evoked activity. J Physiol 496:695–710
75. Ben-Ari Y, Gaiarsa JL, Tyzio R, Khazipov R (2007) GABA: a pioneer transmitter that excites immature neurons and generates primitive oscillations. Physiol Rev 87:1215–1284
76. McKay BE, Tadayonnejad R, Anderson DM, Engbers JDT, Fernandez FR, Iftinca M, Turner RW (2012) Establishing in vivo like activity in rat cerebellar cells maintained in vitro. In Isolated Central Nervous System Circuits (Ed K Ballanyi), Neuromethods Series Vol. 73 (Ed W Walz). Springer Science+Business Media, LLC, New York, NY, pp 233–262
77. Ballanyi K, Grafe P, ten Bruggencate G (1987) Ion activities and potassium uptake mechanisms of glial cells in guinea-pig olfactory cortex slices. J Physiol 382:159–174
78. Konnerth A, Keller BU, Ballanyi K, Yaari Y (1990) Voltage sensitivity of NMDA-receptor mediated postsynaptic currents. Exp Brain Res 81:209–212
79. Ballanyi K, Branchereau P, Champagnat J, Fortin G, Velluti J (1993) Extracellular potassium, glial and neuronal potentials in the solitary complex of rat brainstem slices. Brain Res 607:99–107
80. Ballanyi K, Doutheil J, Brockhaus J (1996) Membrane potentials and microenvironment of rat dorsal vagal cells *in vitro* during energy depletion. J Physiol 495:769–784
81. Ballanyi K, Kaila K (1998) Activity-evoked changes in intracellular pH. In: Kaila K, Ransom BR (eds) pH and brain function. Wiley, New York, pp 283–300
82. Kulik A, Haentzsch A, Lückermann M, Reichelt W, Ballanyi K (1999) Neuron-glia signaling via α_1 adrenoceptor-mediated Ca^{2+} release in Bergmann glia *in situ*. J Neurosci 19:8401–8408
83. Ballanyi K, Kuwana S, Völker A, Morawietz G, Richter DW (1992) Developmental changes in the hypoxia tolerance of the in vitro respiratory network of rats. Neurosci Lett 148:141–144
84. Ballanyi K, Völker A, Richter DW (1996) Functional relevance of anaerobic metabolism in the isolated respiratory network of newborn rats. Eur J Physiol (Pflügers Archiv) 432:741–748
85. Voipio J, Ballanyi K (1997) Interstitial P_{CO2} and pH, and their role as chemostimulants in the isolated respiratory network of neonatal rats. J Physiol 499:527–542
86. Ammann D (1986) Ion-selective microelectrodes. Springer, Berlin/Heidelberg/New York/Tokyo
87. Baumgärtl H (1987) Systematic investigations of needle electrode properties in polarographic measurements of local tissue $P0_2$. In: Ehrly AM, Hauss J, Kolde G (eds) Clinical oxygen pressure

measurement. Springer, Berlin/Heidelberg/New York/London/Paris/Tokyo, pp 17–42

88. Ballanyi K, Grafe P (1985) An intracellular analysis of γ-aminobutyric-acid-associated ion movements in rat sympathetic neurones. J Physiol 365:41–58
89. Ballanyi K, Mückenhoff K, Bellingham MC, Okada Y, Scheid P, Richter DW (1994) Activity-related pH changes in respiratory neurones and glial cells of cats. Neuroreport 6:33–36
90. De Curtis M, Lilbrizzi L, Uva L, Gnatkovsky V (2012) Neuronal networks in the in vitro isolated Guinea Pig Brain. In Isolated Central Nervous System Circuits (Ed K Ballanyi), Neuromethods Series Vol. 73 (Ed W Walz). Springer Science+Business Media, LLC, New York, NY, pp 357–383
91. Day TA, Wilson RJA (2012) The study of respiratory chemoreflexes using a novel dual-perfused rodent preparation. In Isolated Central Nervous System Circuits (Ed K Ballanyi), Neuromethods Series Vol. 73 (Ed W Walz). Springer Science+Business Media, LLC, New York, NY, pp 385–403
92. Onimaru H, Kumagawa Y, Homma I (2006) Respiration-related rhythmic activity in the rostral medulla of newborn rats. J Neurophysiol 9:55–61
93. Ruangkittisakul A, Panaitescu B, Kuribayashi J, Ballanyi K (2010) Caffeine reversal of opioid-evoked and endogenous inspiratory depression in perinatal rat en bloc medullas and slices. Adv Exp Med Biol 669:123–127
94. Bobocea N, Ruangkittisakul A, Ballanyi K (2010) Multiphoton/confocal Ca^{2+}–imaging of inspiratory pre-Bötzinger complex neurons at the rostral or caudal surface of newborn rat brainstem slices. Adv Exp Med Biol 669: 81–85
95. St. John WM (2009) *Noeud vital* for breathing in the brainstem: gasping-yes, eupnoea-doubtful. Philos Trans R Soc Lond B Biol Sci 364:2625–2633
96. Zanella S, Roux JC, Viemari JC, Hilaire G (2006) Possible modulation of the mouse respiratory rhythm generator by A1/C1 neurones. Respir Physiol Neurobiol 153:126–138



http://www.springer.com/978-1-62703-019-9

Isolated Central Nervous System Circuits
Ballanyi, K. (Ed.)
2012, XV, 468 p. 125 illus., 52 illus. in color. With online files/update., Hardcover
ISBN: 978-1-62703-019-9
A product of Humana Press